Astronomy Letters, Vol. 26, No. 6, 2000, pp. 339–343. Translated from Pis'ma v Astronomicheskiĭ Zhurnal, Vol. 26, No. 6, 2000, pp. 403–407.

Optical Spectra of Four Objects Identified with Variable Radio Sources

V. Chavushyan[1], R. Mujica[1], A. G. Gorshkov[2], V. K. Konnikova[2]*, and M. G. Mingaliev[3]

[1] *National Institute of Astrophysics, Optics, and Electronics, Puebla, Mexico*
[2] *Sternberg Astronomical Institute, Universitetskiĭ pr. 13, Moscow, 119899 Russia*
[3] *Special Astrophysical Observatory, Russian Academy of Sciences, Nizhniĭ Arkhyz, Stavropol'skiĭ kraĭ, 357147 Russia*

Received July 5, 1999; in final form, November 17, 1999

Abstract—We obtained optical spectra of four objects identified with variable radio sources. Three objects (0029+0554, 0400+0550, 2245+0500) were found to be quasars with redshifts of 1.314, 0.761, and 1.091. One object (2349+0534) has a continuum spectrum characteristic of BL Lac objects. We analyze spectra of the radio sources in the range 0.97–21.7 GHz for the epoch 1997 and in the range 3.9–11.1 GHz for the epoch 1990, as well as the pattern of variability of their flux densities on time scales of 1.5 and 7 years. *© 2000 MAIK "Nauka/Interperiodica".*

Key words: *optical spectra, radio sources*

INTRODUCTION

We obtained optical spectra of four objects (0029+0554, 0400+0550, 2245+0500, 2349+0534) from a complete flux-limited sample of Zelenchuk-survey radio sources [1]. The sample contains all sources with fluxes $S > 200$ mJy at a frequency of 3.9 GHz and covers 24 h in right ascension at declinations 4°–6° and $|b| > 10°$ [2]. Since the limiting flux of the sample is low enough, the entire luminosity function of quasars is observed up to redshifts $z \approx 1$, which allows an attempt to be made to detect cosmological evolution of the quasar luminosity function after determining the redshifts for all sample objects.

OPTICAL OBSERVATIONS

We carried out optical observations in October 1998 with the 2.1-m telescope at the Guillermo Haro Observatory in Cananea of the National Institute of Astrophysics, Optics, and Electronics, Mexico (INAOE). We used the LFOSC spectrophotometer equipped with a 600 × 400-pixel CCD array [3]. The detector readout noise was 8 e^-, and the wavelength range covered was 4200–9000 Å with a 8.2-Å dispersion. The effective instrumental resolution was ~16 Å.

We performed the standard reduction procedure—the removal of cosmic-ray hits, bias and flat-field corrections, wavelength linearization, and flux calibration—by using the IRAF package.

The source 0440+0550 was observed with a 60-min exposure; the exposure time for the remaining objects was 40 min. Magnitudes were taken from the Automated Plate Scanner Catalog of the Palomar Sky Survey [4].

RADIO OBSERVATIONS

We observed all four radio sources yearly from 1984 until 1992 at frequencies of 3.9 and 7.5 (or 7.7) GHz with the RATAN-600 Southern Sector. In 1990, spectra of the sources at frequencies of 3.9, 4.8, 7.7, and 11.1 GHz [5] were obtained with the Southern and Northern Sectors. Since 1996, the sources have been observed two or three times a year simultaneously at six frequencies (0.97, 2.3, 3.9, 7.7, 11.1, and 21.7 GHz) with the Northern and Western RATAN-600 Sectors. Detector parameters and beam characteristics for the Northern and Western RATAN-600 Sectors are presented in [6, 7]. The same characteristics for the Southern Sector are given in [5]. In every series, the sources were observed 10 to 15 times each. The source flux was obtained by averaging all data in each series. Flux errors were determined from the scatter of fluxes detected daily in a given series; they include all types of error: noise, calibration error, calibration-signal referencing error, antenna pointing error, etc. The reduction procedure is described in [8]. The flux-density scales in different years were reduced to the scale adopted in [7], which presents the observations of all sample sources with power-law spectra.

RESULTS

Table 1 gives objects' names, their radio positions, and differences between the optical and radio positions. The first column contains the source names consisting

* E-mail address for contacts: algor@sai.msu.su

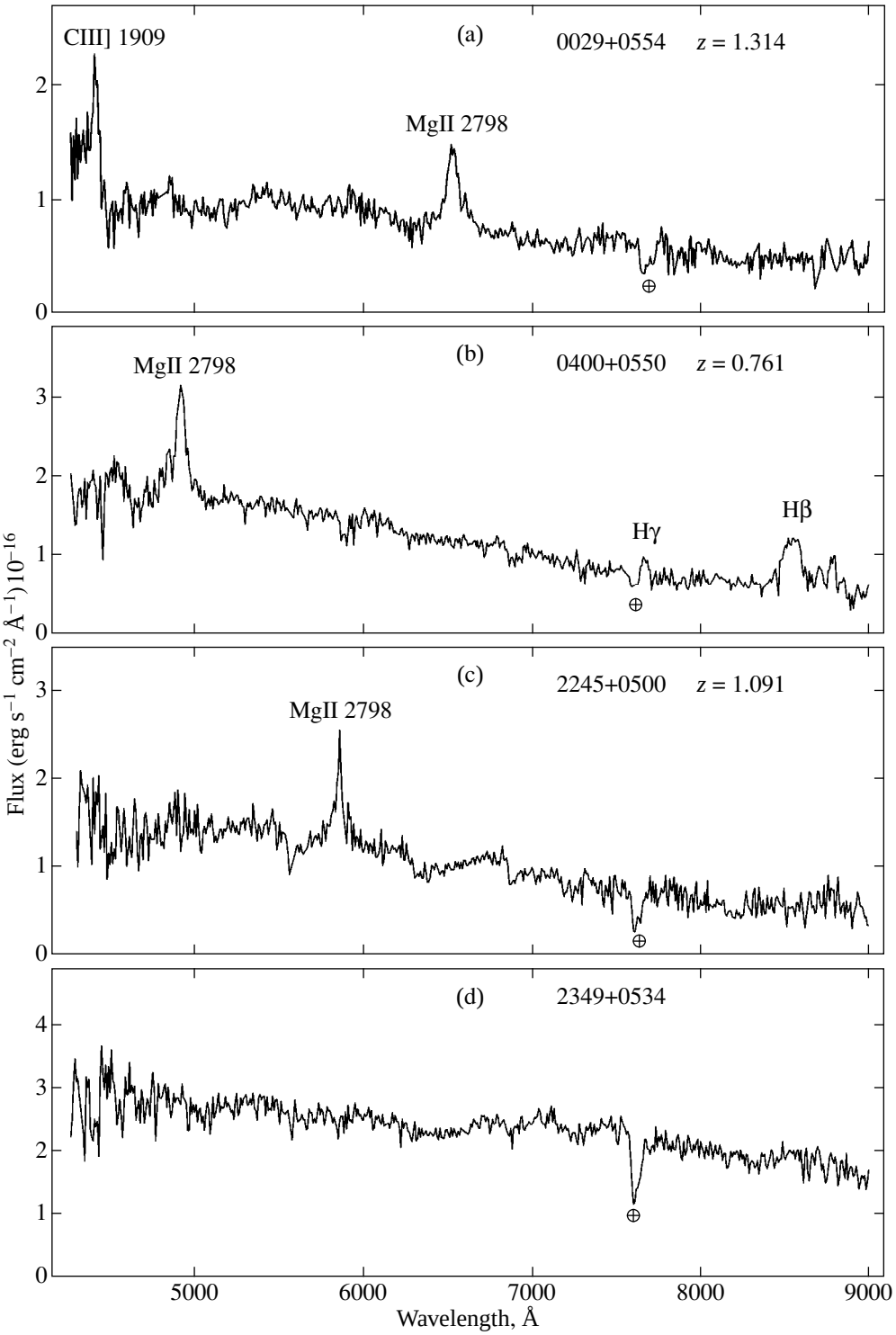

Fig. 1. Optical spectra of the objects identified with the radio sources 0029+0554, 0400+0550, 2245+0500, and 2349+0534.

of hours and minutes of right ascension and degrees and minutes of declination for the epoch 2000. The source names for the epoch 1950 appearing in previous papers are given in parentheses.

The radio positions were taken from the JVAS2 catalog of 2118 northern-sky compact radio sources [9]; the rms error of the positions in this catalogue is 0.014 arcsec. The error in the positions of the optical objects is 0.5 arcsec [4].

The difference between the radio and optical positions for all sources is smaller than 3σ of the total error of the radio and optical positions.

The source 0029+0554 was identified with a star-like object [10]. Figure 1a shows the object's optical

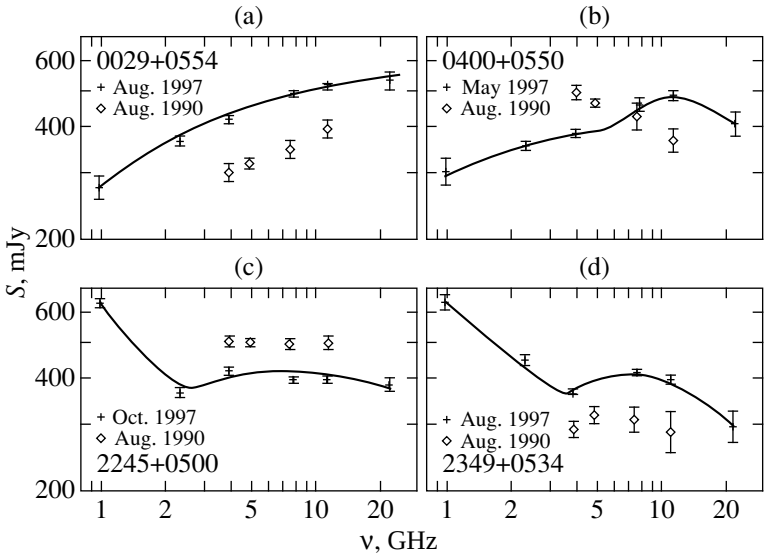

Fig. 2. Radio spectra of the sources 0029+0554, 0400+0550, 2245+0500, and 2349+0534 in 1990 and 1997.

spectrum. The spectrum exhibits two intense lines, which can be interpreted as the semi-forbidden C III] 1909 Å line and the Mg II 2798 Å line at redshift $z = 1.314$. The spectrum is typical of quasars. The RATAN-600 observations of the source show that its flux density slowly increases: between 1990 and 1997, the flux density increased from 300 to 480 mJy at 3.9 GHz and from 360 to 498 mJy at 7.5 GHz. Figure 2a presents the spectra of 0029+0554 obtained in August 1990 in the frequency range 3.9–11.1 GHz and in August 1997 in the range 0.97–21.7 GHz. Both spectra are rising, with the two-frequency spectral index between 3.9 and 7.5 GHz in both spectra being $\alpha \approx 0.23$ ($S \propto \nu^{\alpha}$). In the August 1997 spectrum, the flux density reaches a maximum at 22.7 GHz. During 1.5 years, the source was observed at six frequencies in four series and exhibited no statistically significant variability of its flux density. The relative variability amplitude V was calculated by the method described in [11]. On a time scale of ~8 years (1984–1992), the relative amplitude of long-term variability is 0.11 and 0.14 at 3.9 and 7.5 GHz, respectively [2]. All radio observations show that the flux density of the radio source 0029+0554 varies rather slowly, and the development of a single outburst at the stage of electron acceleration and/or magnetic-field strengthening is observed. The absolute spectral radio luminosity of the source 0027+056 at the frequency of maximum in a homogeneous isotropic cosmological model with a zero cosmological constant, deceleration parameter $q_0 = 0.5$, and $H = 50$ km s^{-1} Mpc^{-1} is $L_\nu = 2.5 \times 10^{34}$ erg s^{-1} Hz^{-1}.

The source 0400+0550 was identified with a star-like object [12]. The source's optical spectrum (Fig. 1b) exhibits three lines, which are interpreted as Mg II 2798 Å, Hγ 4340 Å, and Hβ 4861 Å at redshift $z = 0.761$. The spectrum is typical of quasars. Figure 2b presents the spectra of the source 0400+0550 obtained in August 1990 in the range 3.9–11.1 GHz and in May 1997 in the range 0.97–21.7 GHz.

The August 1990 spectrum is falling with the mean power-law index $\alpha = -0.23$, typical of the outburst spectrum in an optically thin spectral region. The May 1997 spectrum is composite; it can be separated into two components: an extended one with a power-law spectrum and a compact one with a peak in the spectrum attributable to synchroton self-absorption at 13.63 GHz, i.e., the initial stage of development of a new outburst is observed. During the source's observations from April 1996 until May 1997, no statistically significant variability of the flux density was found.

Table 1. Source names, radio positions, and differences between radio and optical positions

Source name	Radio positions, J2000.0		Radio–optical	
	R.A.	Decl.	R.A., arcsec	Decl., arcsec
0029+0554 (0027+056)	$00^h29^m45^s.90$	+05°54′40″.69	–0.30	0.09
0400+0550 (0357+057)	04 00 11.74	+05 50 43.14	0.0	–0.46
2245+0500 (2243+047)	22 45 53 65	+05 00 56.96	–1.35	–1.04
2349+0534 (2346+052)	23 49 21.06	+05 34 39.85	0.15	–0.55

Table 2. A summary of the results of optical and radio observations

Object	Lines	Å	Type	z	B	R	$\frac{S, \text{mJy}}{\frac{3.9, 11.1}{1997}}$	$\frac{V}{\frac{3.9, 7.5}{1984–1991}}$
0029+0554	$\frac{\text{C III]}}{\text{Mg II}}$	$\frac{1909}{2798}$	QSO	1.314	18.7	18.3	$\frac{422\ (9)}{524\ (6)}$	$\frac{0.11}{0.14}$
0400+0550	$\frac{\text{Mg II}}{\frac{\text{H}\gamma}{\text{H}\beta}}$	$\frac{2798}{\frac{4340}{4861}}$	QSO	0.761	18.1	17.5	$\frac{387\ (9)}{497\ (13)}$	$\frac{0.12}{0.13}$
2245+0500	Mg II	2798	QSO	1.091	18.6	18.4	$\frac{405\ (8)}{399\ (8)}$	$\frac{0.34}{0.41}$
2349+0534	none		BL Lac		19.0	18.0	$\frac{366\ (11)}{400\ (10)}$	$\frac{0}{0}$

The relative amplitude of long-term variability in seven years is $V = 0.13$ and 0.15 at 3.9 and 7.5 GHz, respectively [2]. By contrast to the previous source, 0400+0550 exhibits variations on a time scale of 2 or 3 years. The source's absolute spectral radio luminosity at the frequency of maximum of the May 1997 spectrum is $L_\nu = 8.6 \times 10^{33}$ erg s^{-1} Hz^{-1}.

The source 2245+0500 was identified with a starlike object [13]. It was observed in September 1989 with the 1-m telescope of an expedition of the Institute of Theoretical Physics and Astrophysics (Lithuanian Academy of Sciences) at Mount Maidanak (Uzbekistan) in *U*, *B*, and *V*. Its *U* magnitude was 19.3 ± 0.5, $U–B = 0$, and $B–V = 0.3$ [13].

Our optical spectrum exhibits a single line (Fig. 1c). Judging by its profile and intensity, this is the Mg II 2798 Å line at redshift $z = 1.091$, i.e., the object belongs to quasars. Its *B* and *R* magnitudes are 18.6 and 18.4, respectively. The source may also have a variable optical flux.

Figure 2c shows the source's snap-shot spectra obtained in August 1990 and in November 1997. Both spectra have the spectral index $\alpha = 0$ virtually in the entire centimeter range; however, subtracting the extended component from the 1997 composite spectrum reveals a compact component with a peak flux density at 15 GHz. The source was observed at six frequencies from July 1996 through February 1998; the relative variability amplitude *V* at 3.9, 7.7. and 11.1 GHz was, respectively, 0.11, 0.32, and 0.38. The relative amplitude of long-term variability in [2] was 0.34 and 0.41 at 3.9 and 7.5 GHz, respectively.

The daily RATAN-600 observations in January–February 1998 revealed no rapid variability of the source on time scales shorter than 30 days.

The absolute spectral luminosity of the source at the frequency of maximum in the compact component's spectrum is $L_\nu = 1.25 \times 10^{34}$ erg s^{-1} Hz^{-1}.

The source 2349+0534 was identified with a starlike object [13]. The object's optical spectrum (Fig. 1d) is a purely continuum one without noticeable lines. The spectrum is characteristic of BL Lac objects. The optical spectrum was apparently obtained during a radio outburst of the source. During the observations from 1984 until 1992, the source's flux density was essentially the same in all observations, the mean flux densities at 3.9 and 7.5 GHz were, respectively, 300 and 305 mJy, and the spectral index was virtually zero in all observations.

After a considerable break, the source was observed at six frequencies from April 1996 through August 1997. The flux density increased: we apparently observed the initial stage of an outburst in early 1996. Figure 2d shows the source's spectra for the epochs August 1990 and August 1997.

The August 1997 spectrum is composite and can be separated into two components: an intense extended one with a power-law spectrum ($\alpha = –0.9$) and a compact one with a peak in the spectrum at 10.7 Ghz.

CONCLUSION

The results of our optical observations and some characteristics of the objects in the radio band are presented in Table 2.

Of the four objects whose optical spectra we obtained, three are quasars and one is a BL Lac object. For all sources, the ratio of radio and optical flux densities lies in the range $(2–4) \times 10^3$.

ACKNOWLEDGMENTS

We wish to thank J. Miramon, G. Miramon, R. Gonzales, and S. Noriega for technical support and help in the observations with the 2.1-m telescope. This study was supported by the Russian Foundation for Basic Research (project no. 98-02-16428), the Program "Universities of Russia" (project no. 5561), the State Science and Technology Program "Astronomy" (project no. 1.2.5.1), and in part by a CONACYT grant (no. 28499-E).

REFERENCES

1. V. R. Amirkhanyan, A. G. Gorshkov, A. A. Kapustkin, *et al.*, Soobshch. Spets. Astrofiz. Obs. **47**, 5 (1985).
2. A. G. Gorshkov and V. K. Konnikova, Astron. Zh. **72**, 291 (1995).
3. F. J. Zickgraf, I. Thiering, J. Krautter, *et al.*, Astron. Astrophys., Suppl. Ser. **123**, 103 (1997).
4. R. L. Pennigton, R. M. Humphreys, S. C. Odewahn, *et al.*, Publ. Astron. Soc. Pac. **105**, 521 (1993).
5. V. R. Amirkhanyan, A. G. Gorshkov, and V. K. Konnikova, Astron. Zh. **69**, 225 (1992).
6. A. B. Berlin, A. A. Maksyasheva, N. A. Nizhel'skiĭ *et al.*, Abstracts of Papers, in *The XXVII Radio Astron. Conf.* (St. Petersburg, 1997) **3**, p. 115.
7. A. M. Botashev, A. G. Gorshkov, V. K. Konnikova, and M. G. Mingaliev, Preprint No. 132 Spets. Astrofiz. Obs. (1998).
8. A. G. Gorshkov and O. I. Khromov, Izv. Spets. Astrofiz. Obs. **14**, 15 (1981).
9. I. W. A. Browne, A. R. Patnaik, P. N. Wilkinson, and J. M. Wrobel, Mon. Not. R. Astron. Soc. **293**, 251 (1998).
10. A. J. Shimmins, J. G. Bolton, and J. V. Wall, Aust. J. Phys., No. 32, 63 (1975).
11. G. A. Seielstad, T. J. Pearson, and A. C. S. Readhead, Publ. Astron. Soc. Pac. **95**, 842 (1983).
12. C. R. Lawrence, C. L. Bennett, J. N. Hewitt, *et al.*, Astrophys. J., Suppl. Ser. **61**, 105 (1986).
13. O. I. Bugaenko, A. G. Gorshkov, V. F. Esipov, *et al.*, Pis'ma Astron. Zh. **19**, 136 (1993) [Astron. Lett. **19**, 5 (1993)].

Translated by N. Samus'

Astronomy Letters, Vol. 26, No. 6, 2000, pp. 344–355. Translated from Pis'ma v Astronomicheskiĭ Zhurnal, Vol. 26, No. 6, 2000, pp. 408–420.

A Self-Similar Solution for Spherically Symmetric Gravitational Collapse

R. N. Antonova and Ya. M. Kazhdan

Keldysh Institute of Applied Mathematics, Russian Academy of Sciences, Miusskaya pl. 4, Moscow, 125047 Russia

Received October 25, 1999

Abstract—A model of gas-dynamical flow during gravitational collapse is analyzed mathematically by assuming its spherical symmetry and self-similarity. A shock wave diverging from the center emerges in this model. The physical requirements imposed on the post-shock flow at the center for the specified parameters at infinity unambiguously determine the shock front and the flow behind it. *© 2000 MAIK "Nauka/Interperiodica".*

Key words: *plasma astrophysics, hydrodynamics and shock waves; supernovae and supernova remnants*

INTRODUCTION

Gravitational collapse is an astrophysical problem of current interest. A self-similar, spherically symmetric flow is taken by many authors [1–5] as a model to study this phenomenon and, in particular, its gas-dynamical aspect. Self-similarity is ensured by assuming a power-law density distribution at infinity and by a polytropic equation of state for the gas; since self-gravitation is taken into account, the flow is determined by two dimensional constants: the coefficient in the formula for the density distribution and the gravitational constant. Here, we mathematically analyze the flow that arises under these conditions on significant time–space intervals. We use the method of investigation from [6], which is devoted to a self-similar flow during accretion in the gravitational field of a central point mass. There is qualitative agreement between the situations in the solutions obtained here and in the above study. The main points are formulated in the text, while the factors that are not crucial in the emerged flow are mathematically justified in the Appendices.

Let us consider the gas-dynamical flow that arises during gravitational collapse. We consider this flow in the adiabatic approximation. The flow is assumed to be spherically symmetric. As $r \longrightarrow \infty$, where r is the distance from the mass point relative to which the flow is assumed to be spherically symmetric, the velocity u relative to this point, temperature T, and pressure p tend to zero, while the density ρ falls off as a power law

$$\rho \approx \rho_0 r^{-\omega}, \tag{1}$$

where the exponent ω lies in the interval $2 < \omega < 2.5$. The limits of this interval are determined by the requirements that the temperature reduce to zero when $r \longrightarrow \infty$ and that the energy at the initial time in any finite volume be finite.

The equation of state for the gas is assumed to be polytropic,

$$p \approx \rho^\gamma S, \tag{2}$$

where S is the entropy function, and γ is the adiabatic index ($4/3 < \gamma < 5/3$). At the center (for $r = 0$), the velocity is $u = 0$, and the flux is $\dfrac{\partial m_r}{\partial t} = 0$, where m_r is the gas mass within a sphere of radius r.

Our main result is the emergence of a shock wave diverging from the center in the flow under consideration; its front and the post-shock flow are unambiguously determined by the specified state of the gas for $r \longrightarrow \infty$.

The gas-dynamical system of equations for a flow with self-gravitation appears as follows:

$$\begin{aligned}
&\frac{\partial \rho}{\partial t} + \frac{\partial (r^2 u \rho)}{r^2 \partial r} = 0,\\
&\frac{\partial u}{\partial t} + u\frac{\partial u}{\partial r} + \frac{1}{\rho}\frac{\partial p}{\partial r} + \frac{g m_r}{r^2} = 0,\\
&\frac{\partial (p/\rho^\gamma)}{\partial t} + u\frac{\partial (p/\rho^\gamma)}{\partial r} = 0,\\
&m_r(r, t) = \int_0^r 4\pi r^2 \rho\, dr,
\end{aligned} \tag{3}$$

where g is the gravitational constant. The gas-dynamical flux through a sphere of radius r is given by

$$\frac{\partial m_r}{\partial t} = -4\pi r^2 u \rho. \tag{4}$$

* E-mail address for contacts: popov@keldysh.ru

1063-7737/00/2606-0344$20.00 © 2000 MAIK "Nauka/Interperiodica"

We set the following boundary conditions:

$$\rho \approx \rho_0 r^{-\omega}, \quad u \longrightarrow 0, \quad p \longrightarrow 0 \quad \text{when} \quad r \longrightarrow \infty,$$
$$u = 0, \quad \frac{\partial m_r}{\partial t} = 0 \quad \text{at} \quad r = 0. \tag{5}$$

The time t is measured from some time characteristic of the emerged flow.

It seems convenient to reduce the physical quantities to dimensionless form:

$$r = r_0\bar{r}, \quad t = t_0\bar{t}, \quad u = \frac{r_0}{t_0}\bar{u}, \quad \rho = \rho_0 r_0^{-\omega}\bar{\rho},$$
$$p = \rho_0\frac{r_0^{2-\omega}}{t_0}\bar{p}, \quad m_r = 4\pi\rho_0 r_0^{3-\omega} m_r,$$

where r_0 and t_0 satisfy the relation $r_0^{\omega}/t_0^2 = 4\pi g\rho_0$. In this case, one free parameter arises, for example, t_0. In what follows, $t_0 = 1$.

After this transformation, the Euler equation, the quantity m_r, and the asymptotics of the density for $r \longrightarrow \infty$ can be represented as

$$\frac{\partial\bar{u}}{\partial\bar{t}} + \bar{u}\frac{\partial\bar{u}}{\partial\bar{r}} + \frac{1}{\bar{\rho}}\frac{\partial\bar{p}}{\partial\bar{r}} + \frac{\bar{m}_r}{\bar{r}^2} = 0,$$
$$\bar{m}_r = \int_0^{\bar{r}} \bar{\rho}\bar{r}^2 d\bar{r}, \quad \bar{\rho} = \bar{r}^{-\omega}.$$

Below, we omit the bar in the designations.

The form of the equations in the gas-dynamical system and the boundary conditions determine self-similarity of the sought-for solution. The self-similar variable and the self-similar representation of the gas-dynamical functions appear as follows:

$$\eta = \frac{r}{t^{2/\omega}}, \quad u = \frac{r}{t}U(\eta), \quad \rho = r^{-\omega}R(\eta),$$
$$p = \frac{r^{2-\omega}}{t^2}p(\eta), \quad m_r = r^{3-\omega}M_r(\eta). \tag{6}$$

It turns out that the function $M_r(\eta)$ can be explicitly expressed in terms of $U(\eta)$ and $R(\eta)$. Indeed, the gas mass in a sphere of radius r and the gas-dynamical flux through this sphere for the self-similar representation of the functions can be rewritten as

$$M_r = \eta^{\omega-3}\int_0^{\eta}\eta^{2-\omega}R(\eta)d\eta, \tag{7}$$

$$\frac{2}{\omega}M_r'\eta = UR. \tag{8}$$

Below, the prime denotes a derivative of the corresponding function with respect to η.

Thus,

$$M_r' = \frac{1}{\eta}R - \frac{(3-\omega)M_r}{\eta}, \tag{9}$$

and, using equation (8), we obtain

$$M_r = \frac{R(2-\omega U)}{2(3-\omega)}. \tag{10}$$

Since, by definition, R and M_r are nonnegative, the inequality $U(\eta) \le 2/\omega$ must be satisfied for $\omega < 3$ at any η $(0 \le \eta \le \infty)$.

In what follows, it seems convenient to introduce the function $f(\eta) = P(\eta)/R(\eta)$, a self-similar representative of the speed of sound squared, instead of $P(\eta)$. The self-similar system of equations then takes the form

$$\left(U - \frac{2}{\omega}\right)R'\eta + RU'\eta + (3-\omega)UR = 0, \tag{11a}$$

$$\left(U - \frac{2}{\omega}\right)U'\eta + (U^2 - U) + f'\eta + f\left(\frac{R'}{R}\right) + (2-\omega)f + M_r\eta^{-\omega} = 0, \tag{11b}$$

$$\left(U - \frac{2}{\omega}\right)(fR^{1-\gamma})'\eta + [(\gamma\omega + 2 - \omega)U - 2]fR^{1-\gamma} = 0. \tag{11c}$$

For $\eta \longrightarrow \infty$: $\eta^2 f \longrightarrow 0$, $\eta U \longrightarrow 0$, and $R \longrightarrow 1$; for $\eta \longrightarrow 0$: $U(\eta)R(\eta)\eta^{3-\omega} \longrightarrow 0$, and $\eta U(\eta) \longrightarrow 0$.

The derived self-similar system of equations has the first integral—the adiabaticity integral

$$fR^{(1+\omega-3\gamma)/(3-\omega)}\left|U - \frac{2}{\omega}\right|^{[2(\omega-1)-\gamma\omega]/(3-\omega)}\eta^{\omega} = c_0, \tag{12}$$

where the constant c_0 is determined by the asymptotics at infinity and, in the case of shock generation, by the values of the functions at the shock front.

Note that the first two terms, the next three terms, and the last term in the Euler equation (11b) correspond to the acceleration of a unit mass, the pressure force, and the gravitational force, respectively.

Using the first integral, we can represent the self-similar system as

$$U'\eta = \frac{\Phi_1}{\Phi_2}, \tag{13a}$$

$$f'\eta = [(1-3\gamma)U + 2 - (\gamma-1)U'\eta]f/\left(U - \frac{2}{\omega}\right). \tag{13b}$$

Here,

$$\Phi_1 = \left[4\left(1 - \frac{1}{\omega}\right) - 3\gamma U\right]f$$

$$-\left(U-\frac{2}{\omega}\right)(U-U^2-M_r\eta^{-\omega}),$$

$$\Phi_2 = \gamma f-\left(U-\frac{2}{\omega}\right)^2, \qquad (14)$$

$$M_r = -\frac{\omega}{2}\left(U-\frac{2}{\omega}\right)\frac{R}{(3-\omega)},$$

$$R = \left\{\left[c_0\frac{\eta}{f}^{-\omega}\right]^{3-\omega}\left|U-\frac{2}{\omega}\right|^{2+\omega(\gamma-2)}\right\}^{\frac{1}{1-3\gamma+\omega}}.$$

The particular solution of the self-similar system corresponding to the state of complete hydrostatic equilibrium can be written explicitly as

$$U = 0, \quad R = 1, \quad f = \frac{\eta^{-\omega}}{2(\omega-1)(3-\omega)}. \qquad (15)$$

Clearly, this solution satisfies the conditions for $\eta \longrightarrow \infty$ and $\eta \longrightarrow 0$.

ASYMPTOTICS OF THE FUNCTIONS FOR $\eta \longrightarrow \infty$

Based on the natural assumption that the velocity tends to zero and on the specified density distribution $\rho \approx r^{-\omega}$ when $r \longrightarrow \infty$, the asymptotics of $U(\eta)$, $f(\eta)$, and $R(\eta)$ for $\eta \longrightarrow \infty$ appears as follows:

$$U = U_{0\infty}\eta^{-\omega/2} + U_{1\infty}\eta^{-\omega},$$
$$R = 1 + R_1\eta^{-\omega/2}, \qquad (16)$$
$$f = f_0\eta^{-\omega},$$

where $-U_{0\infty}$ and f_0 are arbitrary positive constants, and $U_{1\infty}$ and R_1 are determined by $U_{0\infty}$ and f_0:

$$U_{1\infty} = \left(\frac{\omega}{2}-1\right)U_{0\infty}^2 + 2(\omega-1)f_0 - \frac{1}{3-\omega},$$
$$R_1 = \left(\frac{3\omega}{2}-3\right)U_{0\infty}. \qquad (17)$$

It is convenient to represent f_0 as

$$f_0 = \frac{\Delta_\infty}{2(\omega-1)(3-\omega)},$$

where Δ_∞ is the ratio of the pressure forces to the gravitational force when $r \longrightarrow \infty$ specified from physical conditions.

For a free fall,

$$f = 0, \quad U \approx U_{0\infty}\eta^{-\omega/2}, \quad R \approx 1-3\left(1-\frac{\omega}{2}\right)U_{0\infty}\eta^{-\omega/2},$$

$U_{0\infty}$ is arbitrary. According to this asymptotics, the velocity $u \sim r^{1-\omega/2}$ becomes supersonic as $t \longrightarrow 0$ ($\eta \longrightarrow \infty$); it is lower than the parabolic velocity

$$\left(\frac{r^{1-\omega/2}}{t}\right) \approx \left(1-\frac{\omega}{2}\right)r^{-\omega/2}\frac{dr}{dt}$$
$$= U_{0\infty}\frac{\left(1-\frac{\omega}{2}\right)r^{1-\omega/2}}{t}\eta^{-\omega/2} = U_{0\infty}\left(1-\frac{\omega}{2}\right)r^{1-\omega}$$

for $\omega > 2$ and tends to zero as $r \longrightarrow \infty$.

To within a constant factor, the gas temperature for the assumed equation of state is equal to the speed of sound squared, i.e., $T \sim \frac{r^2}{t^2}f$. Since, according to the derived asymptotics, $T \sim r^{2-\omega}$ when $r \longrightarrow \infty$, the inequality $\omega > 2$ must be satisfied for the temperature and velocity to be zero at infinity.

The total energy inside the sphere of radius r_0 at time $t = 0$ is finite only for $\omega < 5/2$ and is given by

$$E_{r0} = A\frac{r_0^{5-2\omega}}{5-2\omega}\left[\frac{1}{\gamma-1}\frac{\Delta}{2(\omega-1)(3-\omega)} + \frac{U_{0\infty}^2}{2} - \frac{1}{3-\omega}\right], \qquad (18)$$

where A is a positive constant (see Appendix I). Consequently, the requirement of a negative energy at $t = 0$ inside the sphere of radius r_0 relates Δ and u_∞ by the inequality

$$\left[\frac{\Delta}{2(\gamma-1)(\omega-1)(3-\omega)} + \frac{U_{0\infty}^2}{2} - \frac{1}{3-\omega}\right] < 0. \qquad (19)$$

Before a singularity emerges, the flow remains supersonic with respect to any η = const line.

ASYMPTOTICS OF THE FUNCTIONS FOR $\eta \longrightarrow 0$ ($r \longrightarrow 0$)

The inequality $U(\eta) \le 2/\omega$ holds irrespective of the flow pattern, because $M_r(\eta) > 0$. If $U(\eta) \longrightarrow U_0$ as $\eta \longrightarrow 0$, where $|U_0| < \infty$, then $\lim_{\eta\to 0} U'\eta = 0$ and $U(0) < 2/\omega$. This is because the ratio of the third term to the sum of the first two terms in equation (11a) would tend to infinity at $U(0) = 2/\omega$, and (11a) could not hold.

For the specified flow parameters at infinity satisfying the above constraints, the asymptotics for $\eta \longrightarrow 0$ identifies the only flow whose gas-dynamical functions satisfy the system of equations (11a)–(11c) with appropriate boundary conditions.

ASYMPTOTICS OF A SUPERSONIC FLOW FOR $r \longrightarrow 0$

For a supersonic flow near the center, the boundary condition cannot be satisfied when $\eta \longrightarrow 0$. If $f/U^2 < 1$ for $\eta \longrightarrow 0$ and $\gamma < 5/3$, $|U(\eta)| \longrightarrow \infty$ and $\lim f/U^2 \longrightarrow 0$. In this case, the asymptotics of $U(\eta)$ and $R(\eta)$ appears as follows:

$$U(\eta) \approx -\sqrt{2A}\eta^{-3/2}, \quad R(\eta) \approx \frac{3-\omega}{\omega}\sqrt{2A}\eta^{\omega-3/2}, \quad (20)$$

where

$$A = \frac{\omega}{2(3-\omega)}\left(\frac{c_0}{f_0}\right)^{(3-\omega)/(1-3\gamma+\omega)} > 0 \quad (21)$$

(see Appendices II and III). Consequently,

$$RU\eta^{3-\omega} \approx -\frac{2A(3-\omega)}{\omega_0} \neq 0.$$

Thus, the boundary conditions when $\eta \longrightarrow 0$ can be satisfied only for a subsonic flow near the center. The latter is possible when a shock wave diverging from the center or a weak discontinuity along the characteristic arises. Since the flow under consideration is self-similar, η = const lines correspond both to the shock front and to the characteristic: $\eta = \eta_f$ and $\eta = \eta_{ch}$. However, the singular point of system (11a)–(11c) corresponds to the $\eta = \eta_{ch}$ line, and the integral curve can pass through this point only at exceptional values of the parameters in the asymptotics for $\eta \longrightarrow \infty$; we therefore do not consider this situation below.

Thus, a shock wave diverging from the center necessarily arises for a spherically symmetric self-similar flow, which determines gravitational collapse.

CONDITIONS AT THE SHOCK FRONT

Below, the subscripts 1 and 2 denote the pre-shock and post-shock values of the functions, respectively. For the self-similar functions, the conditions at the front $\eta = \eta_f$ appear as follows:

$$M_1^2 = \frac{(2/\omega - f_1)}{\gamma f_1}, \quad (22)$$

$$\frac{R_2}{R_1} = \frac{(\gamma+1)M_1^2}{(\gamma-1)M_1^2+2}, \quad U_2 = \frac{2}{\omega} + \frac{R_1}{R_2}\left(U_1 - \frac{2}{\omega}\right), \quad (23)$$

$$f_2 = f_1 + \frac{(\gamma-1)}{2\gamma}\left(\frac{2}{\omega} - U_1\right)^2\left(1 - \frac{R_1^2}{R_2^2}\right), \quad (24)$$

where M_1^2 is the square of the pre-shock Mach number.

The value of c_0 in the first integral (12) for the post-shock flow can be determined from the derived U_2, f_2, R_2, and η_f.

ASYMPTOTICS OF A SUBSONIC FLOW FOR $r \longrightarrow 0$: $U^2/f \longrightarrow 0$

For a subsonic flow, $U^2/f < 1$; U cannot tend to a finite nonzero value as $\eta \longrightarrow 0$, and $U^2/f \longrightarrow 0$ (see Appendices II, IV).

The sough-for asymptotics can be realized for the specified parameters (c_0, ω, γ) only at a definite coordinate of the shock front, $\eta_f = \eta_{f0}$, at which $\eta \longrightarrow 0$ in the corresponding solution behind the front when $U(\eta) \longrightarrow 0$.

In this case, the asymptotics of the self-similar functions in the principal terms appears as follows:

$$U \approx U_0\eta^\beta \quad (\beta > 0), \quad f = f_0\eta^{-\omega}, \quad R \approx R_0 = R(0), \quad (25)$$

and the boundary conditions for $\eta \longrightarrow 0$ are clearly satisfied. Indeed, according to the first integral (12), $fR^\alpha\eta^\omega \longrightarrow M_0$, where $\alpha = (1 + \omega - 3\gamma)/(3 - \omega)$, and $M_0 = c_0(2/\omega)^{[\gamma\omega - 2(\omega-1)]/(3-\omega)}$. It follows from equation (11a) that $(R'/R)\eta \longrightarrow 0$, and equation (11b) in the principal terms appears as

$$f'\eta + (2-\omega)f + \frac{R\eta^{-\omega}}{3-\omega} = 0. \quad (26)$$

Substituting $f = M_0R^{-\alpha}\eta^{-\omega}$ in (26) yields the equation for $R(\eta)$ with the solution

$$R^{-(1+\alpha)} = T_0\eta^{\frac{2(\omega-1)(1+\alpha)}{\alpha}} + \frac{1}{2M_0(3-\omega)(\omega-1)},$$

where T_0 is an arbitrary constant. Since the exponent $2(\omega - 1)(\alpha + 1)/\alpha > 0$,

$$R(0) = [2M_0(3-\omega)(\omega-1)]^{1/(1+\alpha)} < \infty$$

and

$$f(\eta) \approx M_0R(0)^{-\alpha}\eta^{-\omega} \quad \text{when} \quad \eta \longrightarrow 0.$$

To determine the exponent β, it is necessary to invoke the second terms of the expansion in the asymptotics for f and R; i.e., the asymptotics of the functions for $\eta \longrightarrow 0$ can be represented as

$$U \approx U_0\eta^\beta, \quad f \approx f_0\eta^{-\omega}(1 + f_{10}\eta^\delta), \quad R \approx R_0(1 + R_{10}\eta^\alpha). \quad (27)$$

In this case, it follows from the continuity and Euler equations that $\alpha = \beta$ and $\delta = \beta$, respectively.

Substituting (27) in the first two equations of system (11a)–(11c) and in the first integral (12) and given that $\alpha = \delta = \beta$, we obtain a linear homogeneous system of

equations for U_0, R_{10}, and f_{10} with β-dependent coefficients:

$$\begin{aligned} -\frac{2}{\omega}\beta R_{10} + (3-\omega+\beta)U_0 &= 0,\\ [2(\omega-1)+\beta]R_{10} + [2(1-\omega)+\beta]f_{10} &\\ +\omega(1-\omega)U_0 &= 0,\\ \frac{1-3\gamma+\omega}{3-\omega}R_{10} + f_{10} - \frac{\omega}{2}\frac{2(\omega-1)-\gamma\omega}{3-\omega}U_0 &= 0. \end{aligned} \quad (28)$$

The exponent β can be determined from the condition that the determinant of system (27) is equal to zero; this is a necessary condition for the existence of a nontrivial solution:

$$\gamma\beta^2 + \gamma(5-2\omega)\beta + 2(\omega-1)(4-3\gamma) = 0. \quad (29)$$

Since the free term in (29) is definitely negative for $\gamma > \frac{4}{3}$ and $\omega > 1$, one of the roots β is positive. It will be represented in the sough-for asymptotics. One of the coefficients, for example, U_0, is arbitrary and can be obtained by integration, because the system is homogeneous.

It is important to note that, in this case, only this single free parameter exists; together with the one-parameter set of η_f values, it determines the unique solution $\eta_f = \eta_{f0}$ for which the derived asymptotics is realized.

Indeed, representing the function in the vicinity of $\eta = 0$ as

$$\begin{aligned} U &= U_0\eta^\beta(1+U_1(\eta)),\\ f &= f_0\eta^{-\omega}[1+f_{10}\eta^\beta(1+f_1(\eta))],\\ R &= R_0[1+R_{10}\eta^\beta(1+R_1(\eta))] \end{aligned} \quad (30)$$

the equations for $U_1(\eta)$ and $f_1(\eta)$ follow from system (13a), (13b), and (14) for the initial conditions $\eta = 0$, $U_1(0) = 0$, and $f_1(0) = 0$. The type of singularity of the derived system ($\eta \longrightarrow 0$, $U_1 = 0$, $f_1 = 0$) can be determined from the equations

$$\eta\frac{d\bar{U}_1}{d\eta} = \frac{\frac{2\beta}{\omega}f_{10}U_0[\omega+1-3\gamma-\beta(\gamma-1)]\bar{U}_1}{\left[\frac{2f_{10}}{\omega}\frac{d\bar{f}_1}{d\bar{U}_1} - (\gamma-1)U_0\right]}, \quad (31)$$

$$\bar{R}_1(\eta) = \frac{1}{R_{10}}\left[\frac{\omega-3}{1-3\gamma+\omega}f_{10}\bar{f}_1(\eta) - \frac{\omega}{2}\frac{2+\omega(\gamma-2)}{1-3\gamma+\omega}U_0\bar{U}_1(\eta)\right].$$

Since the right-hand part of the first equation is a constant,

$$\bar{f}_1 = \frac{d\bar{f}_1}{d\bar{U}_1}\bar{U}_1, \quad \frac{2f_{10}}{\omega}\frac{d\bar{f}_1}{d\bar{U}_1} - (\gamma-1)U_0 = \frac{\gamma\beta U_0}{\omega K},$$

where

$$\begin{aligned} \omega K &= 2(\omega-1)\\ &+ \frac{\omega-3}{1+\omega-3\gamma}\left(\frac{2}{\omega}\right)^{(\omega\gamma-2\omega+2)/(1-3\gamma+\omega)} f_0^{(4-3\gamma)/(1-3\gamma+\omega)}\\ &> 2(\omega-1), \end{aligned}$$

$$\eta\frac{d\bar{U}_1}{d\eta} = \left(\beta + \frac{(\omega+1-3\gamma)\omega K}{\gamma\beta}\right)\bar{U}_1.$$

For $\gamma > 4/3$ and $\omega < 3$, $\omega + 1 - 3\gamma < 0$; therefore, for $\omega < 2.5$,

$$\begin{aligned} \beta + \frac{(\omega+1-3\gamma)\omega K}{\gamma\beta} &< \beta + \frac{2(\omega+1-3\gamma)(\omega-1)}{\gamma\beta}\\ &= \frac{\gamma\beta^2 + 2(\omega-1)(4-3\gamma) + 2(\omega-3)(\omega-1)}{\gamma\beta}\\ &= \frac{-\gamma(5-2\omega)\beta + 2(\omega-1)(\omega-3)}{\gamma\beta} < 0. \end{aligned}$$

This implies that the unique solution of system (31), $\bar{U}_1 = 0$, $\bar{f}_1 = 0$, $\bar{R}_1 = 0$, exists at any U_0, which satisfies zero initial conditions; i.e., the singularity is a saddle point, and the system for $U_1(\eta)$ and $f_1(\eta)$ with zero initial conditions has the unique solution.

Thus, if there is an intersection of the one-parameter set of solutions with $U(0) = 0$ for given parameters at infinity with the set of solutions corresponding to the one-parameter set of shock-front coordinates η_f, then it is unique, i.e., corresponds to a certain value of $\eta_f = \eta_{f0}$ and certain coefficients in the asymptotics for $\eta \longrightarrow 0$.

The values of η_{f0} and U_0 can be determined by numerically integrating system (11a)–(11c) or (13a), (13b) with allowance for the asymptotics when $\eta \longrightarrow 0$ (26). To avoid the loss of accuracy resulting from the mutual cancellation of two indefinitely increasing

quantities, it seems convenient to change to new functions and argument:

$$\zeta = \eta^{\beta}, \quad U = U(\zeta), \quad f = f_0\zeta^{-\omega/\beta}(1 + f_1(\zeta)), \quad R = R_0(1 + R_1(\zeta)). \tag{32}$$

The equations for $U(\zeta)$, $f_1(\zeta)$, and $R_1(\zeta)$ and the corresponding asymptotics for $\zeta \longrightarrow 0$ take the form

$$\zeta\frac{df_1}{d\zeta} = \left\{ f_0\left[\omega(\omega-1)U - 2(\omega-1)\left(1-\frac{\omega}{2}U\right)R_1\right] - f_0(1+f_1)\frac{[\gamma\omega-2(\omega-1)]U}{(\gamma-1)(U-2/\omega)} + 2(\omega-1)f_0f_1 + \zeta^{\omega/\beta}\left[\left(U-\frac{2}{\omega}\right)\left(\frac{[\gamma\omega-2(\omega-1)]U}{\gamma-1} + (3-\omega)U\right) + U - U^2\right]\right\}\frac{(\gamma-1)(1+f_1)}{\beta[\gamma f_0(1+f_1) - (U-2/\omega)^2\zeta^{\omega/\beta}]}, \tag{33}$$

$$\zeta\frac{dR_1}{d\zeta} = \frac{1}{(\gamma-1)\beta}(1+R_1) \times\left\{\beta\zeta f_1^{-1}\frac{df_1}{d\zeta} + \frac{[\gamma\omega-2(\omega-1)]U}{U-2/\omega}\right\},$$

$$\zeta\frac{dU}{d\zeta} = \frac{1}{\beta}(\omega-3)U - \frac{(U-2/\omega)}{1+R_1}\zeta\frac{dR_1}{d\zeta},$$

where

$$R_0 = \left[2c_0(\omega-1)(3-\omega)\left(\frac{2}{\omega}\right)^{[\gamma\omega-2(\omega-1)]/(3-\omega)}\right]^{(3-\omega)/(4-3\gamma)}, \tag{34}$$

$$f_0 = \frac{R_0}{2(\omega-1)(3-\omega)}.$$

When $\eta \longrightarrow 0$, $U \approx U_0\zeta$, $f_1 \approx f_{10}\zeta$, $R \approx R_{10}\zeta$,

$$f_{10} = \omega[\omega\gamma - 2(\omega-1) - (\gamma-1)(\omega-3-\beta)]U_0, \quad R_{10} = -\frac{\omega(\omega-3-\beta)}{2\beta}U_0. \tag{35}$$

The value of U_0 is chosen from the condition that, at $\eta = \eta_f$, the values of U, f, and R obtained by integration be equal to their values obtained from the conditions at the shock front $\eta_f = \eta_{f0}$. For example, at $\gamma = 1.4$, $\omega = 2.4$, $U_{0\infty} = -0.5$, $\Delta_\infty = 0.5$, $\eta_{f0} = 0.55587$.

The asymptotics of the physical quantities at the center, i.e., when $r \longrightarrow 0$, and for the specified parameters at infinity appears as follows

$$\text{velocity } u \approx U_0(4\pi g\rho_0)^{-\beta/\omega}r^{(1+\beta)}t^{-(1+2\beta/\omega)} \longrightarrow 0,$$

$$\text{density } \rho \approx \rho_0R_0r^{-\omega} \longrightarrow \infty,$$

$$\text{speed of sound squared } c^2 \approx \gamma f_0(4\pi g\rho_0)r^{2-\omega} \longrightarrow \infty, \tag{36}$$

$$\text{pressure } p \approx \rho_0R_0f_0(4\pi g\rho_0)r^{2(1-\omega)} \longrightarrow \infty,$$

$$\text{central flux } \frac{\partial m_r}{\partial t} = 4\pi\rho_0(4\pi g\rho_0)^{-\beta/\omega} \times U_0R_0r^{3-\omega+\beta}t^{1+2\beta/\omega} \longrightarrow 0.$$

For a free fall $f = 0$, there is such a coefficient $U_{0\infty}$ for $\omega > \omega_0(\gamma)$ in the asymptotics when $\eta \longrightarrow \infty$ that the post-shock flow is hydrostatic at some shock-front coordinate $\eta_f = \eta_{f0}$. In this case, the pre-shock values of the functions are

$$U_1(\eta_{f0}) = \frac{2(1-\gamma)}{\omega}, \quad R_1 = R_1(\eta_{f0}), \quad \eta_{f0} = \left[\frac{(\gamma+1)^2\omega^2R_1(\eta_{f0})}{16(\omega-1)(3-\omega)(\gamma-1)}\right]^{1/\omega}. \tag{37}$$

For $\eta < \eta_{f0}$, the hydrostatic solution is

$$U = 0, \quad R = \frac{(\gamma+1)}{(\gamma-1)}R_1(\eta_{f0}), \quad f = \frac{R_1(\eta_{f0})}{2(\omega-1)(3-\omega)}\eta^{-\omega}.$$

Accordingly, the physical quantities take on the following values:

$$u = 0, \quad \rho = \frac{\gamma+1}{\gamma-1}\rho_0R_1(\eta_{f0})\left(\frac{r}{r_0}\right)^{-\omega} \longrightarrow \infty, \quad p = \frac{(\gamma+1)\rho_0R_1^2(\eta_{f0})}{2(\gamma-1)(3-\omega)}\left(\frac{r}{r_0}\right)^{2-\omega} \longrightarrow \infty, \quad \frac{\partial m_r}{\partial t} = 0. \tag{38}$$

At $\gamma = 1.4$, $\omega(\gamma) \approx 2.28$.

If $|U(\eta)| \longrightarrow \infty$ for $\eta \longrightarrow 0$ and $\gamma f/U^2 > 1$, then the corresponding asymptotics contains two free parameters. It is therefore realized for the specified parameters at infinity for the entire range of shock-front coordinates.

The function $U(\eta) \longrightarrow \infty$ for $0 < \eta_f < \eta_{f0}$ and $\eta \longrightarrow 0$, and the asymptotics of the self-similar functions in the principal terms appears as follows:

$$\eta \longrightarrow 0, \quad U(\eta) \approx U_0\eta^{(4-3\gamma)/(\gamma-1)}, \quad f \approx f_0\eta^{-3}, \quad R \approx R_0\eta^{\omega-\frac{1}{(\gamma-1)}}, \tag{39}$$

i.e., $RU\eta^{3-\omega} \longrightarrow R_0U_0 \neq 0$; the boundary condition for $\eta \longrightarrow 0$ is not satisfied (see Appendix V).

Thus, of all the possible self-similar solutions with the asymptotics of a subsonic flow at the center, only the flow satisfying the natural condition of a zero cen-

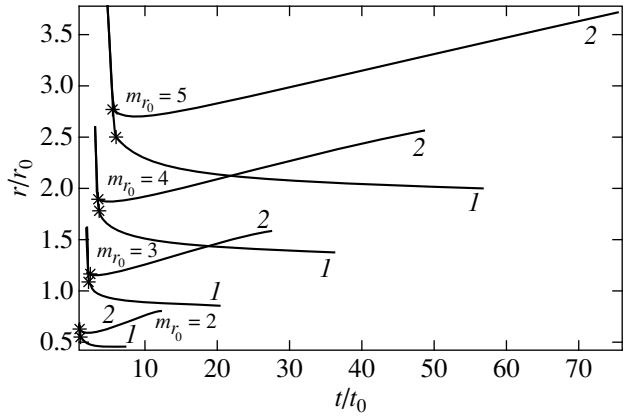

Fig. 1. Particle trajectories $r/r_0 = S(t/t_0)$ belonging to spheres bounding dimensionless masses: $m_{r_0} = 2$, $m_{r_0} = 3$, $m_{r_0} = 4$, and $m_{r_0} = 5$.

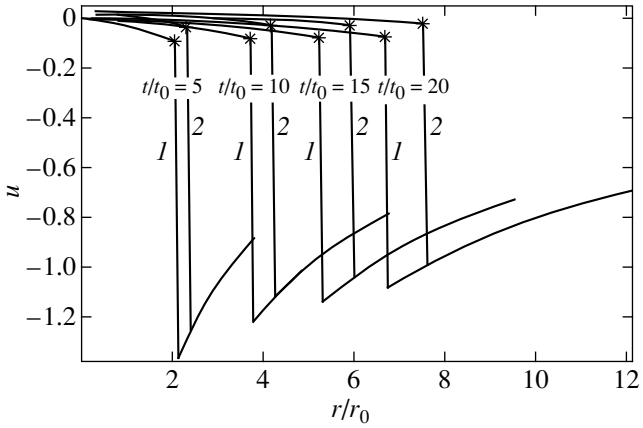

Fig. 2. Profiles of dimensionless hydrodynamic velocity $u(r/r_0)$ for a sequence of dimensionless times: $t/t_0 = 5$, $t/t_0 = 10$, $t/t_0 = 15$, and $t/t_0 = 20$; $*$ shock-front location.

tral gas flux can exist. A definite shock front in the (r, t) plane corresponds to this flow.

ASYMPTOTICS OF A SUBSONIC FLOW FOR $\eta_f > \eta_{f0}$

If the shock-front coordinate $\eta_f > \eta_{f0}$, then $U(\eta_h) = 2/\omega$ at some value of $\eta = \eta_h$. The possible asymptotics of the functions when $\eta \longrightarrow \eta_h$ follows from the emerging singularity in system (13a), (13b), and (14):

$$\begin{aligned}
&\text{(a) } U - \frac{2}{\omega} \approx U_0(\eta - \eta_h),\\
&f \approx f_0(\eta - \eta_h)^{\frac{4(\omega-1)-2\omega\gamma}{4(\omega-1)-6\gamma}} \longrightarrow 0,\\
&R \approx R_0(\eta - \eta_h)^{\frac{2[2+\omega(\gamma-2)]}{4(\omega-1)-6\gamma}} \longrightarrow \infty,\\
&M_r \approx M_{r0}(\eta - \eta_h)^{\frac{2\gamma(\omega-3)}{4(\omega-1)-6\gamma}} \longrightarrow 0,
\end{aligned} \tag{40}$$

where $U_0 = \dfrac{4(\omega-1)-6\gamma}{\gamma\omega\eta_h}$, f_0 is an arbitrary positive number, and

$$\begin{aligned}
R_0^{1+\omega-3\gamma} &= \left(\frac{c_0\eta_h^{-\omega}}{f_0}\right)^{3-\omega} U_0^{2+\omega(\gamma-2)},\\
M_{r0} &= -\frac{R_0U_0\omega}{3-\omega}\frac{\omega}{2};\\
\text{(b) } U - \frac{2}{\omega} &= U_0(\eta - \eta_h),\\
f &= f_0(\eta - \eta_h) \longrightarrow 0,\\
R &= R_0(\eta - \eta_h)^{\frac{\omega(\gamma-1)-1}{\omega+1-3\gamma}},\\
M_r &= M_{r0}(\eta - \eta_h)^{\frac{\gamma(\omega-3)}{\omega+1-3\gamma}} \longrightarrow 0,\\
U_0 &= \frac{2(1-3\gamma+\omega)}{\gamma\omega}, \quad f_0 = \frac{\omega-2}{\omega(\omega-3)}U_0.
\end{aligned} \tag{41}$$

After numerical integration over the entire range of parameters $(\gamma, \omega, U_\infty, f_0)$, the integral curves approached the first of the possible asymptotics for $\eta > \eta_{f0}$. In this case, there are two free parameters: η_h and the coefficient in the asymptotics f_0. Consequently, this situation arises for the specified parameters at infinity for the entire interval of shock-front coordinates, $\eta_{f0} < \eta_f < \infty$. Thus, if the shock-front coordinate $\eta_f > \eta_{f0}$, then a cavity diverging from the center and growing with time proportional to $t^{2/\omega}$ emerges.

It should be noted that the $\eta = \eta_h$ line (the cavity boundary) is a trajectory in the (r, t) plane. Indeed, a trajectory in the (r, t) plane is given by the equation

$$\frac{dr}{dt} = u$$

or, changing to the self-similar variables,

$$\frac{d\eta}{dt} = \frac{\eta}{t}(U - 2/\omega).$$

Consequently, $\dfrac{d\eta}{dt} = 0$ along the η_h line where $U(\eta_h) = 2/\omega$. According to the asymptotics (40), we have at the cavity boundary:

$$\begin{aligned}
&\text{velocity } u = \frac{2}{\omega}\eta_h t^{\frac{2}{\omega}-1},\\
&\text{density } \rho \sim \frac{\eta_h^{-\omega}}{t^2}R_0(\eta - \eta_h)^{-\frac{4(\omega-1)-2\gamma\omega}{4(\omega-1)-6\gamma}},\\
&\text{pressure } p \sim \gamma R_0 f_0 \eta_h^{2-\omega} t^{\frac{4}{\omega}(1-\omega)}.
\end{aligned} \tag{42}$$

Clearly, this solution cannot be considered satisfactory from a gas-dynamical point of view, because the pressure at the cavity boundary in it is finite. However,

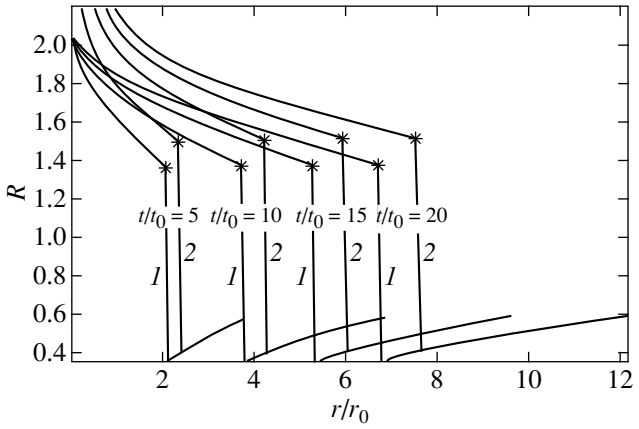

Fig. 3. Same as Fig. 2 for the function proportional to density $R = (r/r_0)^{\omega}\rho(r/r_0)$: (*1*) flow with zero central flux, self-similar front coordinate $\eta_f = 0.55587$; (*2*) flow with an emerging cavity, self-similar front coordinate $\eta_f = 0.625$, cavity boundary $\eta_h = 0.1$; $*$ shock-front location.

the derived solution can be interpreted as the flow behind a spherical piston diverging from the center, whose radius r_p, in view of the assumed self-similarity, increases with time as $r_p = \eta_h t^{2/\omega}$. The cavity boundary coincides with the piston surface; the piston velocity and the pressure on it decrease with time.

Of interest is the change in the radius of a fixed layer of gas with time, which follows from the explicit expression for $M_r(\eta)$ (10) and from the self-similar representation of the gas mass inside a sphere of radius r: $m_r(r, t) = r^{3-\omega}M_r(\eta)$.

The particle trajectory at times t longer than some fixed time t_0 is given by

$$r^{3-\omega}M_r(\eta) = r_0^{3-\omega}M_r(\eta_0). \qquad (43)$$

The right-hand part of this equation determines the gas mass inside the sphere of radius r_0 at fixed time t_0. In this case, $r_0 = \eta_0 t_0^{2/\omega}$. Figure 1 shows trajectories for various types of flow. At $U(0) = 0$, the trajectory radius approaches some positive value with time, i.e., the layer stops. At $U(\eta_h) = 2/\omega$, the trajectory radius increases starting from some time, i.e., expansion begins.

Plots of velocity and density versus radius at various times t for each of the two types of flow we considered are shown in Figs. 2 and 3.

CONCLUSION

We have singled out the unique, acceptable (from a gas-dynamical point of view) solution from all types of solutions to the self-similar equations that satisfy boundary conditions at the center and at infinity for the specified admissible flow parameters when $r \longrightarrow \infty$; i.e., we have identified the front of a shock wave diverging from the center that provides a zero velocity and a zero flux at the center. Thus, the central physical conditions producing this solution were determined. Naturally, the central state cannot be unique, identified in our case. An analysis of gas-dynamical quantities at the center differing from those we obtained will apparently require investigating a problem that is not self-similar.

In the gas-dynamical theory of gravitational collapse for massive stars or, to be more precise, for their iron cores (their total mass exceeds $10M_\odot$), virtually the same self-similar problem that we solved here arises. Nadyozhin [1] obtained a self-similar solution for an ideal gas with the adiabatic index $\gamma = 5/3$ by taking into account neutrino energy losses (with a distinctive power-law dependence on density and temperature). Subsequently, Jahil [3] constructed a physically close self-similar solution for several adiabatic indices $\gamma < 4/3$, but without allowance for neutrino losses [5]. Murzina and Nadyozhin [4] investigated self-similar gravitational collapse in the case of volume energy losses. All these solutions end with a singularity at time $t = 0$ (the domain of the solution: $0 \geq t > -\infty$) and do not include the shock front. Actually, as shown by numerical solutions to the gas-dynamical problem of collapse that take into account a complex equation of state for the gas (in particular, with a variable adiabatic index and a general law of neutrino energy losses, whose behavior change sharply when opacity or neutrino self-absorption arise), the development of the collapse is suspended without reaching a characteristic singularity in the self-similar solution [2]. In this case, a strong shock wave, which virtually stops the motion of gas toward the center, is invariably formed. Here, we obtained (for the above constraints on the parameters at infinity) this kind of self-similar solution for collapsing matter with the inclusion of the shock front, which is useful in interpreting numerical gas-dynamical calculations.

ACKNOWLEDGMENTS

We wish to thank V.S. Imshennik and participants of the workshop directed by him (Institute of Theoretical and Experimental Physics) for a helpful discussion. We are also grateful to G.S. Bisnovatyĭ-Kogan, who proposed to write this paper.

REFERENCES

1. D. K. Nadyozhin, Astron. Zh. **45**, 1166 (1968).
2. V. S. Imshennik and D. K. Nadyozhin, in *Itogi Nauki i Tekhniki. Ser. Astronomiya* (VINITI, Moscow, 1982), Vol. 21, p. 63.
3. A. Jahil, Astrophys. J. **265**, 1047 (1983).
4. M. V. Murzina and D. K. Nadyozhin, Astron. Zh. **68**, 574 (1991).
5. V. S. Imshennik, in *Astrophysics on the Threshold of the 21st Century*, Ed. by N. S. Kardashev (Gordon and Breach Science, Philadelphia, 1992), p. 167.
6. Ya. M. Kazhdan and M. V. Mursina, Astrophys. J. **400**, 192 (1992).

APPENDIX I

In the self-similar flow under study, the total energy inside any sphere of finite radius $0 \le r_0 < \infty$ at $t = 0$ is finite and nonpositive if and only if the flow parameters ω, U_∞, and Δ_∞ satisfy the conditions

$$2 < \omega < 2.5,$$
$$\frac{\Delta_\infty}{2(\gamma-1)(3-\omega)(\omega-1)} + \frac{U_{0\infty}^2}{2} - \frac{1}{3-\omega} < 0. \quad \text{(I.1)}$$

The total energy inside the sphere of radius r_0 is given by the integral

$$E_{r0} = 4\pi\int_0^{r_0}\rho r^2\left[\frac{1}{\gamma-1}\frac{p}{\rho} + \frac{u^2}{2} - \frac{Gm_r}{r}\right]dr. \quad \text{(I.2)}$$

After changing to the self-similar variables and using the explicit expression for $M_r(\eta)$, this integral can be represented as

$$E_{r0} = A\int_0^{r_0} r^{4-2\omega}\Phi(\eta)dr, \quad \text{(I.3)}$$

where

$$\Phi(\eta) = R(\eta)\left[\eta^\omega\left(\frac{f(\eta)}{\gamma-1} + \frac{U^2(\eta)}{2}\right) + \frac{\omega}{2(3-\omega)}R(\eta)\left(U(\eta) - \frac{2}{\omega}\right)\right],$$

and the constant $A > 0$.

At $t = 0$, η is infinite at finite $r > 0$; at $r = 0$, it varies in the range $\eta_0 \le \eta \le \infty$, where $\eta_0 = 0$, if the flow near the center is supersonic or subsonic, and $\eta_f \le \eta_{f0}$, while $\eta_0 = \eta_h$ if $\eta_f > \eta_{f0}$.

The integral that specifies E_{r0} at time $t = 0$ can be represented as the sum of integrals:

$$\int_0^{r_0} r^{4-2\omega}\Phi(\eta)dr = \lim_{r_1\to 0}\int_{r_1}^{r_0} r^{4-2\omega}\Phi(\eta)dr \quad (r_1 > 0) + \lim_{t\to 0} t^{5-2\omega}\int_{\eta_0}^{\infty}\eta^{4-2\omega}\Phi(\eta)d\eta. \quad \text{(I.4)}$$

In the first integral, $\eta = \infty$, and, according to the asymptotics (16) and (17), we have for $2 < \omega < 3$

$$\lim_{\eta\to\infty}\Phi(\eta) = \frac{\Delta_\infty}{2(\gamma-1)(\omega-1)(3-\omega)} + \frac{U_{0\infty}^2}{2} - \frac{1}{3-\omega},$$

therefore,

$$\lim_{r_1\to 0}\int_{r_1(r_1>0)}^{r_0} r^{4-2\omega}\Phi(\eta)dr = \frac{r_0^{5-2\omega}}{5-2\omega}\left(\frac{\Delta_\infty}{2(\gamma-1)(\omega-1)(3-\omega)} + \frac{U_{0\infty}^2}{2} - \frac{1}{3-\omega}\right). \quad \text{(I.5)}$$

To determine the second term on the right-hand side of (I.4), we represent the integral in it as the sum of four integrals:

$$\int_{\eta_0}^{\infty} = \int_{\eta_0}^{\eta_0+\varepsilon} + \int_{\eta_0+\varepsilon}^{\eta_1} + \int_{\eta_1}^{N} + \int_{N}^{\infty}. \quad \text{(I.6)}$$

Here, ε is small enough, while N is large enough; $\eta_1 = \eta_f$ is the shock coordinate in discontinuous flows, η_1 is any number, $\eta_0 + \varepsilon < \eta_1 < N$ in continuous solutions.

According to the asymptotics, for $\eta \longrightarrow 0$ and $\eta \longrightarrow \eta_h$ $(4/3 < \gamma < 5/3)$,

$$\int_{\eta_0}^{\eta_0+\varepsilon}\eta^{4-2\omega}\Phi(\eta)d\eta \sim \varepsilon^{\delta_1}, \text{ where } \delta_1 \ge 1/2, \text{ at } \eta_0 = 0, \quad \text{(I.7)}$$

$$\int_{\eta_0}^{\eta_0+\varepsilon}\eta^{4-2\omega}\Phi(\eta)d\eta \sim \varepsilon^{\delta_2}, \text{ where } \delta_2 = \frac{\gamma(\omega-3)}{2(\omega-1)-3\gamma} > 0, \text{ at } \eta_0 = \eta_h. \quad \text{(I.8)}$$

The integrals $\int_{\eta_0+\varepsilon}^{\eta_1}$ and $\int_{\eta_1}^{N}$ are finite, because the integrands are continuous and bounded in these intervals. The integral

$$\int_N^\infty \eta^{4-2\omega}\Phi(\eta)d\eta \sim \begin{cases}\left(\frac{\Delta_\infty}{2(\gamma-1)(\omega-1)(3-\omega)} + \frac{U_{0\infty}^2}{2} - \frac{1}{3-\omega}\right)\frac{\eta^{5-2\omega}}{5-2\omega} \\ \text{at } \omega \ne \frac{5}{2}, \\ \ln\eta \text{ at } \omega = \frac{5}{2}.\end{cases} \quad \text{(I.9)}$$

It is easy to see from the above estimates that

$$\lim_{t\to 0} t^{5-2\omega}\int_{\eta_0}^{\infty}\eta^{4-2\omega}\Phi(\eta)d\eta = \begin{cases}\infty \text{ at } \omega \ge \frac{5}{2}, \\ 0 \text{ at } \omega < \frac{5}{2}.\end{cases} \quad \text{(I.10)}$$

In view of the boundary condition at infinity (the temperature $T \longrightarrow 0$ as $r \longrightarrow \infty$), the parameter $\omega > 2$.

Thus, for the energy at $t = 0$ to be finite and nonpositive inside any sphere of radius r, $0 \le r < \infty$, it is necessary that $2 < \omega < 2.5$ and that the inequality

$$\frac{\Delta_\infty}{2(\gamma-1)(\omega-1)(3-\omega)} + \frac{U_{0\infty}^2}{2} - \frac{1}{3-\omega} < 0 \qquad \text{(I.11)}$$

be satisfied.

APPENDIX II

If $|U(\eta)| \longrightarrow \infty$ for $\eta \longrightarrow 0$ and $4/3 < \gamma < 5/3$, then the ratio f/U^2 cannot tend to a finite nonzero limit. Indeed, if $|U(\eta)| \longrightarrow \infty$ and $f/U^2 \longrightarrow K$, where $0 < K < \infty$, then, according to equation (13b), $|U| \sim \eta^\alpha$, where $\alpha = \frac{1-3\gamma}{\gamma+1}$, and it follows from the first integral (12) that

$$R \sim [|U(\eta)|^{\gamma\omega-4}\eta^{-\omega(3-\omega)}]^{1/(1+\omega-3\gamma)},$$

therefore,

$$R|U(\eta)|\eta^{\omega-3} \sim \eta^{[\alpha(1+\gamma)-(1-3\gamma)](\omega-3)/(1+\omega-3\gamma)}.$$

When $\eta \longrightarrow 0$ and $|U(\eta)| \longrightarrow \infty$, according to equation (11a), $R|U(\eta)|\eta^{3-\omega} \longrightarrow \text{const} = L$, where $0 \le L < \infty$. However, L cannot be equal to zero, because the exponent α in this case would be larger than $\frac{1-3\gamma}{1+\gamma}$, in conflict with equation (13b). Consequently, $L > 0$. In this case, however, $M_r \sim RU \sim \eta^{\omega-3}$, hence $M_r\eta^{-\omega} \sim \eta^{-3}$, and, since $U \sim \eta^{(1-3\gamma)/(\gamma+1)}$, $M_r\eta^{-\omega}/U^2 \sim \eta^{(3\gamma-5)/(\gamma+1)} \longrightarrow \infty$.

We then have $U'\eta \approx \frac{M_r\eta^{-\omega}}{KU} \sim \frac{\eta^{-3}}{U}$, i.e., $U^2 \sim \eta^{-3}$ but the emerging condition $\frac{1-3\gamma}{\gamma+1} = -3/2$ can be satisfied only at $\gamma = 5/3$.

APPENDIX III

The flow near the center ($\eta = 0$) can be only subsonic. If $(\gamma f/U^2 < 1)\lim U(\eta) = U_0$ for supersonic onflow at the center, where $|U_0| < \infty$, then $U_0 = 2/3$.

It follows from the assumption $|U_0| < \infty$ that $\lim_{\eta\to 0} U'\eta = 0$, $f(0) < \infty$, and $\Phi_2(\eta) < \infty$, while $\lim_{\eta\to 0}\Phi_1(\eta) = 0$. In this case, $f(0) = 0$, because, according to the first integral (12), $M_r \sim R \sim \eta^{(\omega-3)\omega/(1-3\gamma+\omega)}$ at $f(0) \ne 0$ (given that $U_0 < 2/\omega$), and, consequently, $M_r\eta^{-\omega} \sim \eta^{(3\gamma-4)/(1-3\gamma+\omega)} \longrightarrow \infty$ and $\Phi_1(\eta) \longrightarrow \infty$. In our case, $U_0 \ne 0$, because it would follow from the equality $U_0 = 0$ that $R(0) = 0$, and equation (11a) could not be satisfied. The ratio of the first term in this equation to the sum of the other two would tend to infinity. $U_0 \ne 1$, because $\omega > 2$, while $U_0 < 2/\omega$. It thus follows from the condition $\lim_{\eta\to 0}\Phi_1(\eta) = 0$ that $\lim_{\eta\to 0} M_r\eta^{-\omega} = U_0 - U_0^2$, i.e., $R \sim M_r \sim \eta^\omega$. On the other hand, according to equation (11a), $R \sim \eta^{(\omega-3)U_0/(U_0-2/\omega)}$. U_0 is therefore determined by the equality $\frac{(\omega-3)U_0}{U_0-2/\omega} = \omega$, i.e., $U_0 = 2/3$, and the asymptotics appears as follows:

$$U \approx 2/3 + U_{10}\eta^\alpha, \quad f \approx f_{10}\eta^\omega, \quad M_r \approx 2/9\eta^\omega.$$

In view of the equality

$$M_r = \frac{R(2-\omega U)}{2(3-\omega)},$$

we obtain

$$R \approx (2/3 + R_{10}\eta^\alpha)\eta^\omega,$$

where $\alpha = \frac{(3\gamma-4)\omega}{3-\omega}$. Thus, $RU\eta^{3-\omega} \longrightarrow 0$ as $\eta \longrightarrow 0$.

However, as follows from the numerical integration of system (13a), (13b), and (14), this asymptotics for any c_0 and $\eta \longrightarrow \infty$ yields $R(\eta) \longrightarrow \text{const} \ll 1$; i.e., the initial asymptotics (16) is not satisfied when $\eta \longrightarrow \infty$. So, the function $U(\eta)$ does not tend to a finite limit for supersonic onflow at the center when $\eta \longrightarrow 0$.

If, however, $U(\eta) \longrightarrow \infty$, then $RU\eta^{3-\omega} \longrightarrow \text{const} \ne 0$ and $U\eta \longrightarrow \infty$; i.e., the boundary conditions are not satisfied when $\eta \longrightarrow 0$. Indeed, $\gamma f/U^2 \longrightarrow 0$ in this case, because $\gamma f/U^2$ cannot tend to a finite, nonzero limit as $U(\eta) \longrightarrow \infty$, and $\gamma f/U^2 < 1$ (see Appendix II).

For $\gamma f/U^2 < 1$ and $U(\eta) \longrightarrow \infty$ ($\eta \longrightarrow 0$), in the principal terms of the function,

$$\Phi_1(\eta) \approx U(U^2 + M_r\eta^{-\omega}), \quad \Phi_2(\eta) \approx -U^2,$$

$$\eta\frac{df}{d\eta} = \left[(1-3\gamma) - \frac{(\gamma-1)U'\eta}{U}\right]f, \qquad \text{(III.1)}$$

$$\eta\frac{dM_r}{d\eta} \simeq (\omega-3)M_r,$$

i.e., $f \approx f_0\eta^{1-3\gamma}|U|^{1-\gamma}$ and $M_r \approx A\eta^{\omega-3}$, while $M_r\eta^{-\omega} \approx A\eta^{-3}$; the coefficient A is given by

$$A = \frac{\omega}{2(3-\omega)}\left(\frac{c_0}{f_0}\right)^{(3-\omega)/(1-3\gamma+\omega)}. \qquad \text{(III.2)}$$

Two cases are then possible:

(1) $\frac{M_r\eta^{-\omega}}{U^2}$ cannot tend to zero as $\eta \longrightarrow 0$, because $U \sim \eta^{-1}$, and, consequently, $f \sim \eta^{-2\gamma}$ and $f/U^2 \sim \eta^{-2(\gamma-1)} \longrightarrow \infty$.

(2) $\frac{M_r\eta^{-\omega}}{U^2}$ cannot tend to infinity, because $U \approx (2A/3)^{2/3}\eta^{-3/2}$, and, consequently, $f = f_0\eta^{(1-3\gamma)}$ and $f/U^2 \sim \eta^{4-3\gamma} \longrightarrow \infty$ for $\gamma > 4/3$.

Thus, $U^2 \sim M_r\eta^{-\omega}$ with

$$\eta\frac{dU}{d\eta} = -\frac{U^2 + M_r\eta^{-\omega}}{U} = -\frac{U^2 + A\eta^{-3}}{U}.$$

Consequently,

$$U \simeq -\sqrt{2A}\eta^{-3/2}, \quad f \approx f_0(2A)^{(1-\gamma)/2}\eta^{-(1+3\gamma)/2}, \quad R \approx \frac{(3-\omega)}{\omega}\sqrt{2A}\eta^{\omega-3/2}, \tag{III.3}$$

and, for $\eta \longrightarrow 0$,

$$RU\eta^{3-\omega} \approx \frac{2(3-\omega)}{\omega}A \neq 0, \quad U\eta \longrightarrow \eta^{-1/2} \longrightarrow \infty.$$

APPENDIX IV

For a subsonic flow, $\gamma f/U^2 > 1$ and $\gamma > 4/3$, the function $U(\eta)$ near the center when $\eta \longrightarrow 0$ cannot tend to constant U_0, where $0 < |U_0| < \infty$.

Indeed, if $U(\eta) \longrightarrow U_0$, where $0 < |U_0| < \infty$, then it is necessary that $U'\eta \longrightarrow 0$, $U_0 < 2/\omega$, and $f(\eta) \longrightarrow f_0 > 0$. According to equation (13b), $f(\eta) \sim \eta^\alpha$ when $\eta \longrightarrow 0$, where $\alpha = \frac{(1-3\gamma)U_0 + 2}{U_0 - 2/\omega}$. Since $f_0 > 0$, it is necessary that $\alpha \leq 0$. However, the exponent α must be negative, because $R \sim \eta^{-\omega(3-\omega)/(1+\omega-3\gamma)}$, while $M_r\eta^{-\omega} \sim \eta^{\omega(3\gamma-4)/(1+\omega-3\gamma)} \longrightarrow \infty$ at $\alpha = 0$; consequently, $\Phi_1(\eta) \longrightarrow \infty$, while $|\Phi_2(\eta)| < \infty$, i.e., $U'\eta \longrightarrow \infty$. Thus, it is necessary that $U_0 < \frac{2}{3\gamma - 1}$ and, hence, $f \longrightarrow \infty$. In this case,

$$\Phi_2(\eta) \sim f,$$

$$\Phi_1(\eta) \sim \left[4\left(1 - \frac{1}{\omega}\right) - 3\gamma U_0\right]f + \left(U_0 - \frac{2}{\omega}\right)M_r\eta^{-\omega}.$$

The condition $U'\eta \longrightarrow 0$ can therefore be satisfied only if $M_r\eta^{-\omega}/f \longrightarrow A$, where the constant $A \geq 0$, with $A = 0$ at $U_0 = U_0^* = \frac{4(\omega-1)}{3\gamma\omega} > 0$. However, for $|U_0| < \infty$, the quantity $R \sim \eta^{(3U_0-2)/(2/\omega-U_0)}$, while $M_r\eta^{-\omega} \sim \eta^{(3U_0-2)/(2/\omega-U_0)}$ and $M_r\eta^{-\omega}/f \sim \eta^\beta$, where

$$\beta = \frac{3U_0 - 2}{2/\omega - U_0} - \frac{(3\gamma-1)U_0 - 2}{2/\omega - U_0} = \frac{(4-3\gamma)U_0}{2/\omega - U_0}.$$

But $\beta < 0$ at $U_0 = U_0^*$ and $A = \text{const}$, i.e., $\beta = 0$ only at $\gamma = 4/3$.

APPENDIX V

For $\eta \longrightarrow 0$ and $|U(\eta)| \longrightarrow \infty$, the corresponding asymptotics in a subsonic flow near the center contains two arbitrary constants, as follows from the form of its first two terms. Consequently, this asymptotics at the specified parameters γ, ω, U_∞, and Δ_∞ is realized for the entire interval of shock-front coordinates η_f.

When $\eta \longrightarrow 0$ and $|U(\eta)| \longrightarrow \infty$ and for $U^2/\gamma f < 1$, $U^2/f \longrightarrow 0$ (see Appendix II). In this case, it follows from equation (11a) that $RU\eta^{3-\omega} \longrightarrow \text{const}$; therefore, $M_r \approx -\frac{\omega}{2}RU/(3-\omega) \approx M_{r0}\eta^{\omega-3}$.

Since $U^2/f \longrightarrow 0$, equation (11b) in the principal terms appears as follows:

$$f'\eta + f\frac{R'}{R}\eta + (2-\omega)f + M_{r0}\eta^{-3} = 0,$$

and its solution is $f = f_0\eta^{-3}$. Indeed, assuming that $R \sim \eta^\alpha$ or $R \sim \text{const}$ when $\eta \longrightarrow 0$, we find that the solution of this equation in the principal term can be (1) $f \sim f_0\eta^{\omega-2-\alpha}$ (at $R \sim \text{const}$, $\alpha = 0$), for $\omega - 2 - \alpha < -3$, or (2) $f \sim \eta^{-3}$.

Since $U \sim \eta^{\omega-3-\alpha}$, $U/f \sim \eta^{-1} \longrightarrow \infty$ in the first case; given that $U \longrightarrow \infty$, clearly, $U^2/f \longrightarrow \infty$, in conflict with the initial assumption. Thus, $f \approx f_0\eta^{-3}$ in the principal term in the solution of this equation for $\eta \longrightarrow 0$. In this case, it follows from the first integral that $U \sim U_0\eta^{(4-3\gamma)/(\gamma-1)}$, and, consequently, $R \approx R_0\eta^{\omega-1/(\gamma-1)}$. One of the coefficients of the derived asymptotics, for example, U_0, is arbitrary and can be obtained only by integrating system (13a), (13b); in this case, $R_0U_0 = L$ and $f_0 = -\frac{\omega}{2\gamma}\frac{(\gamma-1)}{3-\omega}L$, where

$$L = -\left[\frac{2(3-\omega)}{\omega}c_0\frac{3\gamma-4}{\gamma-1}|U_0|^{1-\gamma}\right]^{(3-\omega)/(4-3\gamma)}.$$

In accordance with the condition $U(\eta) \longrightarrow \infty$ as $\eta \longrightarrow 0$, the derived asymptotics is possible only for $\gamma > 4/3$.

Thus, if $U(\eta) \longrightarrow \infty$ when $\eta \longrightarrow 0$, then

$$U(\eta) \approx U_0\eta^{(4-3\gamma)/(\gamma-1)}, \quad f \approx f_0\eta^{-3}, \quad R \approx R_0\eta^{\omega-1/(\gamma-1)}.$$

To determine the second terms, we represent the asymptotics of the functions for $\eta \longrightarrow 0$ as

$$U = U_0\eta^{(4-3\gamma)/(\gamma-1)}(1 + U_1(\eta)), \quad R = R_0\eta^{\omega-1/(\gamma-1)}(1 + R_1(\eta)), \quad f = f_0\eta^{-3}(1 + f_1). \tag{V.1}$$

Cumbersome calculations (they are omitted here) yielded the following functions $U_1(\eta)$, $f_1(\eta)$, and $R_1(\eta)$.

For $4/3 < \gamma < 3/2$,

$$U_1 = U_{10}\eta^{(3\gamma-4)/(\gamma-1)} + U_{20}\eta^{(5\gamma-3)/(\gamma-1)} + U_1^*(\eta),$$

$$f_1 = f_{10}\eta^{(3\gamma-4)/(\gamma-1)} + f_{20}\eta^{(5\gamma-3)/(\gamma-1)} + f_1^*(\eta), \quad \text{(V.2)}$$

$$R_1 = R_{10}\eta^{(3\gamma-4)/(\gamma-1)} + R_{20}\eta^{(5\gamma-3)/(\gamma-1)} + R_1^*(\eta),$$

where U_{10}, f_{10}, and R_{10} are given by the system of linear equations

$$\frac{3\gamma-4}{\gamma-1}(R_{10}+U_{10}) = \frac{2}{\omega U_0}(\omega - f_{10}),$$

$$f_0\left[\frac{(3\gamma-4)}{\gamma-1} - \frac{\gamma}{\gamma-1}\right]f_{10} + \left(f_0\frac{3\gamma-4}{\gamma-1}+1\right)R_{10} + U_{10} - \frac{2}{\omega U_0} = 0, \quad \text{(V.3)}$$

$$f_{10} + \frac{1-3\gamma+\omega}{3-\omega}R_{10} + \frac{(3-\gamma)\omega-2}{3-\omega}U_{10} = \frac{2}{\omega}\left[\frac{(3-\gamma)\omega-2}{3-\omega}\right]U_0,$$

$$R_1^*(\eta) = U_1^*(\eta) = C\eta^{-\frac{\gamma}{\gamma-1}\frac{\alpha}{1-\alpha}}, \quad \text{(V.4)}$$

$$f_1^*(\eta) = -\alpha R_1^*, \ \alpha = [3(1-\gamma)+(\gamma-2)\omega]/(3-\omega).$$

For $3/2 < \gamma < 5/3$,

$$f_1 = \frac{1-\gamma}{2\gamma}\frac{U_0^2}{f_0}\eta^{(5-3\gamma)/(\gamma-1)} + C\eta,$$

$$R_1 = \frac{-1}{2\gamma}\frac{U_0^2}{f_0}\eta^{(5-3\gamma)/(\gamma-1)} + \frac{C}{\gamma-1}\eta, \quad \text{(V.5)}$$

$$U_1 = \frac{1}{2\gamma}\frac{U_0^2}{f_0}\eta^{(5-3\gamma)/(\gamma-1)} - \frac{C}{\gamma-1}\eta.$$

C in (V.4) and (V.5) and for $4/3 < \gamma < 5/3$ is an arbitrary constant.

Thus, if the function $U(\eta) \longrightarrow \infty$ in a subsonic flow for $4/3 < \gamma < 5/3$ and $\eta \longrightarrow 0$, then the corresponding asymptotics is determined by two arbitrary parameters; it can thus be realized for the specified flow parameters at infinity for the entire range of η_f, which determine the shock-front location in the (r, t) plane.

Translated by V. Astakhov

Astronomy Letters, Vol. 26, No. 6, 2000, pp. 356–361. Translated from Pis'ma v Astronomicheskiĭ Zhurnal, Vol. 26, No. 6, 2000, pp. 421–426.

A Self-Similar Solution for a Supernova Explosion with Allowance for Accelerated Relativistic Particles

I. N. Toptygin*

St. Petersburg State Technical University, ul. Politekhnicheskaya 29, St. Petersburg, 195251 Russia

Received August 18, 1999; in final form, November 16, 1999

Abstract—A self-similar solution to Sedov's problem of a strong explosion in a homogeneous medium is generalized to the case of relativistic-particle generation in a supernova remnant; the particles are accelerated by Fermi's mechanism at the shock front and in the perturbed post-shock region. Self-similarity takes place if the thickness of the prefront is small compared to its radius and if the pressure ratio of the relativistic and nonrelativistic components at the shock front is kept constant. In the presence of relativistic particles, the time dependence of the shock-front radius remains the same as that in their absence, but the plasma parameters in the inner perturbed region change appreciably. The shell of the matter raked up by the explosion is denser and thinner than that in the nonrelativistic case, the relativistic-particle pressure in the central region remains finite, and the nonrelativistic-gas pressure at the explosion center approaches zero. The influence of relativistic particles on the transition to the radiative phase of expansion of the supernova remnant and on its dynamics is studied. It is shown that relativistic particles can decrease several-fold the remnant radius at which the transition to the radiative phase occurs. © *2000 MAIK "Nauka/Interperiodica"*.

Key words: *supernovae and supernova remnants*

INTRODUCTION AND STATEMENT OF THE PROBLEM

In the case of spherical symmetry, the expansion of supernova remnants and strong stellar winds can be described at some evolutionary stages by self-similar solutions [1–4], which allow the laws of motion of shock fronts and plasma in perturbed regions to be found. Self-similar solutions are widely used to analyze specific astrophysical phenomena [5]. However, in such an analysis, the fact that shock fronts can accelerate charged particles up to relativistic energies [6] should be taken into account; an appreciable fraction of the energy of the primary perturbation, reaching tens of percents, can be transferred to the accelerated particles. Under these conditions, the relativistic component (accelerated particles) becomes an important dynamic factor and considerably affects the gas dynamics of plasma, i.e., the density and pressure distribution behind the front of a spherical shock wave.

Here, our goal is to generalize self-similar solutions to the case where relativistic accelerated particles are present and to deduce the observational implications of these solutions. The problem is solved in a two-fluid gas-dynamical approximation; the relativistic component is described by pressure $p_c(r, t)$, whose value at the shock front is specified as a boundary condition. In a microscopic treatment (which is not presented here), the accelerated-particle pressure at the front can be expressed in terms of the injection rate of nonrelativistic particles to the acceleration regime, much as we did in [7] for a steady-state case. In the above paper, we also showed that the density of accelerated particles is generally negligible compared to the total density of plasma particles. Based on numerical calculations, Berezhko *et al.* [8] have recently considered in detail the particle acceleration in supernova remnants. However, these authors focused their attention on the microscopic aspect of the problem, treated gas-dynamical phenomena in a simplified way, and did not discuss the relationship of their results to known self-similar solutions for various expansion stages of supernova remnants.

The set of gas-dynamical equations for deriving self-similar solutions is taken in the Euler approximation [9], i.e., without allowance for viscosity and heat conduction in the regions of smoothly varying gas-dynamical parameters. In our case, this set is

$$\frac{\partial \rho}{\partial t} + \frac{\partial(\rho u)}{\partial r} + \frac{2\rho u}{r} = 0, \tag{1}$$

$$\frac{\partial u}{\partial t} + u\frac{\partial u}{\partial r} + \frac{1}{\rho}\frac{\partial}{\partial r}(p_g + p_c) = 0, \tag{2}$$

$$\frac{\partial}{\partial t}\left(\frac{1}{2}\rho u^2 + w_g\right) + \frac{1}{r^2}\frac{\partial}{\partial r}(r^2 q_g) + u\frac{\partial p_c}{\partial r} = 0, \tag{3}$$

* E-mail address for contacts: INT@cosmos.hop.stu.neva.ru

1063-7737/00/2606-0356$20.00 © 2000 MAIK "Nauka/Interperiodica"

$$\frac{\partial w_c}{\partial t} + \frac{1}{r^2}\frac{\partial}{\partial r}(r^2 q_c) - u\frac{\partial p_c}{\partial r} = 0. \quad (4)$$

Here, equations (3) and (4) describe the energy balance for the nonrelativistic and relativistic components, which are assumed to be polytropic gases,

$$w_g = \frac{p_g}{\gamma_g - 1}, \quad w_c = \frac{p_c}{\gamma_c - 1} \quad (5)$$

are the densities of their internal energies, and $\gamma_g = 5/3$ and γ_c are the Poisson adiabatic indices. For a relativistic gas, we have $5/3 > \gamma_c \geq 4/3$, depending on the shape of the accelerated-particle spectrum [7]. The quantity

$$q_g = \left(\frac{1}{2}\rho u^2 + \frac{\gamma_g}{\gamma_g - 1}p_g\right)u \quad (6)$$

is the energy flux density of a nonrelativistic gas. The energy flux of the accelerated particles is given by

$$q_c = \frac{\gamma_c}{\gamma_c - 1}p_c u - \frac{\kappa}{\gamma_c - 1}\frac{\partial p_c}{\partial r}, \quad (7)$$

where κ is the diffusion coefficient determined by small-scale magnetic fields. The presence of diffusion coefficient in (7) introduces some characteristic scale (transport mean free path Λ of the accelerated particles) into the problem, and a self-similar solution can be constructed only by disregarding this scale. For this reason, we take the approximation $\kappa \longrightarrow 0$, which corresponds to neglect of the shock transition thickness determined by the accelerated particles in comparison with the front radius

$$R_s \gg \frac{v}{u}\Lambda, \quad (8)$$

where v is the particle velocity. This approximation does not result in any significant constraint, because a sufficiently large acceleration is possible only if the inequality (8) is satisfied. If this inequality is violated, the particles quickly leave the neighborhood of the front and cannot gain appreciable energy.

STRONG EXPLOSION WITH ALLOWANCE FOR THE GENERATION OF RELATIVISTIC PARTICLES

For an instantaneous point release of energy E (and neglecting the mass of the ejected shell) in a homogeneous medium of density ρ_0, we have the self-similar variable [9]

$$s = \frac{r}{R_s(t)}, \quad R_s(t) = \beta\left(\frac{Et^2}{\rho_0}\right)^{1/5}, \quad (9)$$

where $R_s(t)$ is the shock radius, β is a dimensionless constant, which is defined below. This approach is applicable only to expansion into a "cold" medium, i.e., when the pressure is neglected in comparison with the pressure in the perturbed region. It is valid irrespective of whether accelerated relativistic particles are generated during the explosion. The self-similar variable differs from the nonrelativistic case only by the constant β. However, the solution in the perturbed region $s < 1$ differs more significantly from Sedov's well-known solution [9].

We introduce dimensionless dependent variables $U(s)$, $G(s)$, $Y(s)$, $Z(s)$ given by the relations

$$u(r,t) = \frac{2r}{5t}U(s), \quad \rho(r,t) = \rho_0 G(s),$$

$$p_c(r,t) = \frac{4r^2\rho_0}{25t^2\gamma_c}G(s)Y(s), \quad (10)$$

$$p_g(r,t) = \frac{4r^2\rho_0}{25t^2\gamma_g}G(s)Z(s).$$

Substituting these relations in set (1)–(4) yields ordinary differential equations with one independent variable $\xi = \ln s$, which can be written in symmetric form as

$$\frac{d\ln G}{d\xi} = \frac{1}{1-U}\left(\frac{dU}{d\xi} + 3U\right), \quad (11)$$

$$\frac{dU}{d\xi} = \frac{3U(Y+Z) - 3(Y/\gamma_c + Z/\gamma_g) - U(1-U)(5/2-U)}{(1-U)^2 - Y - Z}, \quad (12)$$

$$\frac{d\ln Y}{d\xi} = \frac{\gamma_c - 1}{1-U}\frac{dU}{d\xi} + \frac{(3\gamma_c - 1)U - 5}{1-U}, \quad (13)$$

$$\frac{d\ln Z}{d\xi} = \frac{\gamma_g - 1}{1-U}\frac{dU}{d\xi} + \frac{(3\gamma_g - 1)U - 5}{1-U}. \quad (14)$$

To determine the four unknown functions, we must specify four boundary conditions at the shock front. In the presence of relativistic particles, the boundary conditions will differ from those specified for an ordinary gas-dynamical front. Let us formulate them with allowance for the condition (8), i.e., neglecting the thickness of the front broadened by relativistic particles in comparison with its radius. First of all, the relative plasma compression at the front

$$\sigma = \frac{\rho(R_s(t), t)}{\rho_0} = G(1) \quad (15)$$

can exceed $\sigma_g = (\gamma_g + 1)/(\gamma_g - 1)$ for a strong gas-dynamical nonradiative shock wave. The value $\sigma \geq 4$ depends on the rate of particle injection to the acceleration regime and on the spectrum shape, which can be determined by solving the kinetic equation [7]. When a purely gas-dynamical problem is considered, this quantity must be specified as an external parameter.

In the local frame of reference associated with some portion of the shock front, the pre- and post-shock

plasma velocities v_1 and v_2 satisfy the relation $v_1/v_2 = \sigma$. Since $v_1 = v_s = \dot{R}_s(t) = 2R_s(t)/5t$, and $u(R_s(t), t) = v_s - v_2 = v_s(1 - \sigma^{-1})$, this yields

$$U(1) = 1 - \sigma^{-1}. \quad (16)$$

Conservation of the momentum flux through the front, $\rho_1 v_1^2 + p_1 = \rho_2 v_2^2 + p_2$, allows the total pressure $p_{tot} = p_2$ on the inner side of the front to be found at $\rho_1 = \rho_0$, $v_1 = v_s$, $\rho_2 = \sigma\rho_0$, and $p_1 \approx 0$:

$$p_{tot} = p_{gs} + p_{cs} = \rho_0 v_s^2(1 - 1/\sigma). \quad (17)$$

A similar equation for the energy flux results in the relation

$$\frac{\gamma_g}{\gamma_g - 1}p_{gs} + \frac{\gamma_c}{\gamma_c - 1}p_{cs} = \frac{v_s}{2v_2}\rho_0(v_s^2 - v_2^2). \quad (18)$$

This equality suggests the absence of "runaway" particles, whose energy is so large that they freely leave the system. From the last two equalities, we find the fraction of the dynamic pressure at the front transferred to the accelerated particles:

$$\eta = \frac{p_{cs}}{\rho_0 v_s^2} = \frac{\gamma_c - 1}{\gamma_g - \gamma_c}\left[\frac{(\gamma_g - 1)\sigma}{2} - \gamma_g + \frac{\gamma_g + 1}{2\sigma}\right]. \quad (19)$$

The last formula is valid only in the presence of relativistic particles, i.e., for $\gamma_c < \gamma_g$. Using relations (10) and the preceding equalities, we can find the remaining boundary conditions:

$$Y(1) = \frac{\eta\gamma_c}{\sigma}, \quad Z(1) = \frac{\gamma_g}{\sigma}\left(1 - \frac{1}{\sigma} - \eta\right). \quad (20)$$

The boundary conditions (15), (16), and (20) form a complete set. They include the parameter σ, which is calculated by kinetic methods. The results obtained when solving a steady-state problem [7] can be applied in the case under consideration only to a quasi-static regime, when the front displaces by a small distance compared to its radius on an acceleration time scale $\tau_a \approx \kappa/v_s^2$. This regime requires sufficiently small particle transport mean free paths, i.e., strong plasma turbulization. A transition to the case of a nonrelativistic gas-dynamical shock wave occurs for $\sigma \longrightarrow (\gamma_g + 1)/(\gamma_g - 1)$. This implies $\eta \longrightarrow 0$ and $Y \longrightarrow 0$, and the conditions (15), (16), (20) transform to Sedov's conditions [9].

The set of ordinary nonlinear equations (11)–(14) with the above boundary conditions can be readily integrated numerically. This procedure is facilitated by constructing the energy integral for these equations, which can be done by using the methods of Sedov [9] or Landau and Lifshitz [10]. In this way, we obtain the relationship between the dimensionless functions U, Y, and Z:

$$\frac{1}{2}U^2(1 - U) = \frac{Y(\gamma_c U - 1)}{\gamma_c(\gamma_c - 1)} + \frac{Z(\gamma_g U - 1)}{\gamma_g(\gamma_g - 1)}, \quad (21)$$

which satisfies the boundary conditions (16) and (20). However, even the derivation of the asymptotics of the solution at $s \ll 1$ and its comparison with the asymptotics of Sedov [9] reveal the principal differences brought about by relativistic particles.

Let us represent the sough-for functions in the region $s \ll 1$ as

$$U(s) = U_0 + A_u s^{a_u}, \quad G(s) = A_g s^{a_g},$$

$$Y(s) = A_y s^{a_y}, \quad Z(s) = A_z s^{a_z},$$

where U_0, A, and a are constants; $U_0 > 0$ by the meaning of this quantity, and $a_u > 0$ and $a_g \geq 0$ because the velocity and density are bounded. From equations (11), (13), and (14), we find

$$a_g = \frac{3U_0}{1 - U_0}, \quad a_y = -\frac{3(2 - \gamma_c)}{1 - U_0} - 3\gamma_c + 1,$$

$$a_z = -\frac{3(2 - \gamma_g)}{1 - U_0} - 3\gamma_g + 1.$$

The condition $a_g > 0$ yields $U_0 < 1$; whence it follows that $a_y < 0$, $a_z < 0$, $a_y - a_z = a_g(\gamma_c - \gamma_g) < 0$. Thus, we have $Y(s) \gg Z(s)$ for $s \ll 1$. This condition implies that, in the central explosion region, the pressure of the relativistic particles prevails, $p_c \gg p_g$, for any their finite contribution η to the total pressure at the front.

From equation (12), we find

$$U_0 = \frac{1}{\gamma_c}, \quad a_u = \frac{3(\gamma_g - \gamma_c)}{\gamma_c - 1} \quad (22)$$

and finally obtain

$$a_g = \frac{3}{\gamma_c - 1}, \quad a_y = -\frac{2\gamma_c + 1}{\gamma_c - 1}, \quad a_z = a_y + a_u. \quad (23)$$

In contrast to Sedov's solution, the nonrelativistic-gas pressure vanishes at the explosion center, $p_g \longrightarrow 0$, while the accelerated-particle pressure remains finite: $p_c \longrightarrow$ const as $r \longrightarrow 0$. The gas density at the explosion center in the presence of relativistic particles approaches zero more rapidly than it does in their absence. In the limiting case of ultrarelativistic particles ($\gamma_c \longrightarrow 4/3$), we have $\rho \propto r^9$, whereas in the nonrelativistic gas-dynamical case $\rho \propto r^{4.5}$. Thus, in the presence of relativistic particles, the shell becomes thinner, denser, and colder than in the nonrelativistic case. These qualitative conclusions are confirmed by numerical calculations, whose results are shown in the figure. The calculations were carried out for $\gamma_c = 4/3$. The plasma velocity inside the perturbed region grows toward the periphery almost linearly; the pressure of

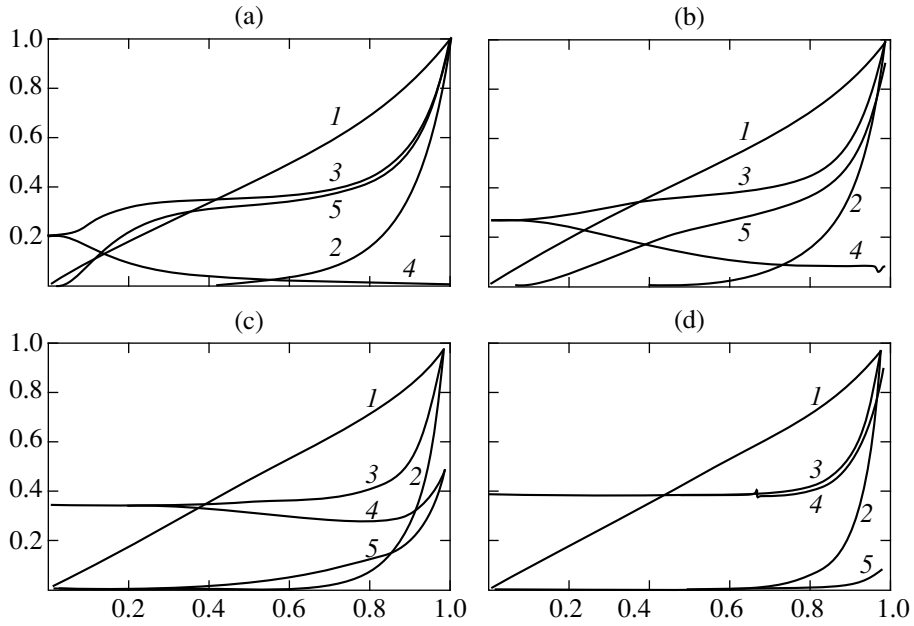

Plasma parameters *versus* distance from the explosion center in the perturbed region, normalized to their values on the inner side of the front: (a) $\sigma = 4.01$, (b) $\sigma = 4.25$; (c) $\sigma = 5.50$; (d) $\sigma = 6.75$. Curves *1* for plasma velocity, *2* for density, *3* for total pressure, *4* and *5* for the pressure of relativistic and nonrelativistic particles, respectively, relative to the total pressure at the front.

the accelerated particles is finite in the central region even for their very small contribution to the total pressure at the front (figure a); and the nonrelativistic-gas pressure decreases with increasing compression and vanishes at the explosion center. The shell thickness also decreases with increasing compression.

The constant β appearing in the self-similar variables (9) can be determined from equality of the explosion energy E and the total energy of the gas and the accelerated particles:

$$E = \int_0^{R_s(t)} \left(\frac{\rho u^2}{2} + \frac{p_g}{\gamma_g - 1} + \frac{p_c}{\gamma_c - 1}\right) 4\pi r^2 dr, \qquad (24)$$

which gives the relation

$$\beta^5 \frac{16\pi}{25} \int_0^1 \left[\frac{1}{2}U^2(s) + \frac{Y(s)}{\gamma_c(\gamma_c - 1)} + \frac{Z(s)}{\gamma_g(\gamma_g - 1)}\right] G(s) s^4 ds = 1. \qquad (25)$$

The table lists numerical values of β and fractions η_k, η_g, and η_c ($\eta_k + \eta_g + \eta_c = 1$) of the total explosion energy accounted for by the shell kinetic energy, the nonrelativistic-gas internal energy, and the accelerated-particle energy, respectively. This table also gives the parameter A characterizing the remnant radius (see the next section). As we see from the table, the fraction of the explosion energy η_c accounted for by the accelerated particles rapidly grows with increasing relative compression, with the injection rate remaining modest [7, 8] and quite attainable under real conditions. As the compression increases further, the runaway particles, which we disregarded here, begin to play a significant role, and they must be included in the calculations to obtain reliable results. Although the compression can, in principle, be arbitrarily large, stable states are possible only for moderate compressions, which apparently do not exceed $\sigma = 8$–10 [11].

RADIATIVE EVOLUTIONARY STAGE OF THE SUPERNOVA REMNANT

The redistribution of total explosion energy in favor of the accelerated particles with increasing relative compression σ results in a change of the parameters and dependences that characterize the radiative stage of expansion of the supernova remnant. Let us make the corresponding estimates following [12] and our results.

At the previous, adiabatic stage, the temperature immediately behind the shock front is

$$T_s = \frac{\mu v_s^2}{\sigma}\left(1 - \frac{1}{\sigma} - \eta\right), \qquad (26)$$

where $\mu = 0.60 m_H$ is the mean mass per particle for standard elemental abundances. This value can be obtained from relations (17) and (19) and the equation of state for a nonrelativistic gas $p_{gs} = (\rho_0\sigma/\mu)T_s$. The transition to the radiative stage occurs when the post-shock temperature reaches some value T_r at which strong radiation in the lines of heavy elements takes

The distribution of explosion energy between the components and the normalization constant as a function of relative compression

σ	4.00	4.01	4.10	4.25	4.50	4.75	5.00	5.50	5.90	6.30	6.75	6.90
β	1.148	1.132	1.088	1.097	1.097	1.075	1.067	1.032	1.019	1.004	0.995	0.991
η_c	0.000	0.062	0.255	0.267	0.331	0.440	0.504	0.640	0.699	0.750	0.789	0.801
η_g	0.721	0.675	0.521	0.494	0.420	0.323	0.260	0.148	0.094	0.052	0.016	0.006
η_k	0.279	0.262	0.223	0.239	0.249	0.237	0.236	0.212	0.207	0.198	0.195	0.193
A	10.8	10.5	9.7	9.6	9.2	8.5	7.9	6.6	5.8	4.8	3.3	2.4

place ($T_r = 6 \times 10^5$ K, according to [12]). From this condition, we find the transition radius of the remnant

$$R_c = \left[\frac{4\mu E}{25\rho_0 T_r}\frac{\beta^4}{\sigma}\left(1-\frac{1}{\sigma}-\eta\right)\right]^{1/3} = 15\left[\frac{(E/10^{50})\beta^5}{n_0\sigma}\left(1-\frac{1}{\sigma}-\eta\right)\right]^{1/3}\ \text{pc}. \quad (27)$$

Here, the second equality suggests that $\rho_0 = 1.26 m_H n_0$, where n_0 is the atomic number density (cm^{-3}), and E is the explosion energy (in ergs). The dependence on explosion energy and on ambient density in the presence of accelerated particles does not change, $R_c = A(E/10^{50})^{1/3} n_0^{-1/3}$, but the numerical coefficient A decreases from 10.8 at $\sigma = 4$ to 2.4 at $\sigma = 6.9$ (see table).

After the radius R_c is reached, a thin dense cold shell surrounding the region filled with heated gas and accelerated particles is rapidly formed. Almost the entire mass of the raked-up gas is contained in this shell. The pressure inside the shell is close to a uniform one, because the speed of sound is relatively high, but decreases with time due to the remnant expansion. The dependence of the pressure on remnant radius can be found in the snowplough model [12]. Denoting the internal energy of the remnant by

$$E_T = \frac{4}{3}\pi R^3\left(\frac{p_g}{\gamma_g - 1} + \frac{p_c}{\gamma_c - 1}\right), \quad (28)$$

we write the condition of its adiabatic expansion as

$$\dot{E}_T = -4\pi R^2 p\dot{R}, \quad (29)$$

where $p = p_g + p_c$ is the total pressure. In this case, we assume that the dense shell prevents the outward escape of the accelerated particles and that their pressure in the outer region is low. To estimate their maximum effect, we take the condition $p_c \gg p_g$. The applicability of this inequality is facilitated by the fact that, as the compression increases, an increasingly large fraction of the energy is accounted for by the accelerated particles (see table), and that a considerable part of the internal energy of nonrelativistic gas is lost during radiative cooling (more than half, according to [12]). In this approximation, we obtained from equalities (28) and (29)

$$E_T = E_{T0}\left(\frac{R_c}{R}\right)^{3(\gamma_c - 1)}, \quad (30)$$

where E_{T0} is the internal energy of the remnant after radiative cooling. This energy can be approximately estimated with the aid of the table; a more accurate result requires a numerical calculation of radiative cooling. For $\gamma_c = 4/3$, we have the dependence $p_c \propto R^{-4}$, whereas in the nonrelativistic case $p_g \propto R^{-5}$.

To calculate the time dependence of the remnant radius, we take into account the balance of mass and the balance of momentum of the cold shell (neglecting the small mass of the central part):

$$M = \frac{4}{3}\pi R^3\rho_0, \quad \frac{d}{dt}(M\dot{R}) = 4\pi R^2 p. \quad (31)$$

Using these and the preceding equations, we can easily find the asymptotics of the radiative stage of expansion of the supernova remnant:

$$R(t) = \left(\frac{27}{4\pi\rho_0}E_{T0}R_c t^2\right)^{1/6}. \quad (32)$$

The derived time dependence $R(t) \propto t^{1/3}$ is similar to the dependence $R(t) \propto t^{2/7}$ for the nonrelativistic case.

It should be emphasized that the latter result is valid only if the dense shell holds well the relativistic particles within the remnant. Since there are no observational and theoretical data on regular and turbulent magnetic fields in the shell, this assumption may prove to be wrong. In this case, the estimate (27) for the transition radius of the remnant is preserved, but its subsequent evolution will follow a more complex law.

CONCLUSION

We have obtained a self-similar solution to the nonsteady-state gas-dynamical problem of the adiabatic stage of a strong point explosion accompanied by the generation of relativistic particles. The mechanism of accelerated-particle generation is unimportant. The solution allows us to calculate the variations of plasma parameters in the perturbed region and the distribution of total explosion energy between the nonrelativistic gas and the relativistic particles.

ACKNOWLEDGMENTS

I am grateful to A.M. Bykov for a discussion of the statement of the problem and of the results obtained. This study was supported in part by the Russian Foundation for Basic Research (project no. 98-02-17711) and the Ministry of Education of the Russian Federation (project no. 990110).

REFERENCES

1. L. I. Sedov, Dokl. Akad. Nauk SSSR **52**, 17 (1946).
2. V. S. Avedisova, Astron. Zh. **48**, 894 (1971).
3. R. Weaver, R. McCray, J. Castor, *et al.*, Astrophys. J. **218**, 377 (1977).
4. R. A. Chevalier, Astrophys. J. **258**, 790 (1982).
5. I. S. Shklovskii, *Supernovae* (Nauka, Moscow, 1976).
6. E. G. Berezhko and G. F. Krymskii, Usp. Fiz. Nauk **154**, 49 (1988).
7. I. N. Toptygin, Zh. Éksp. Teor. Fiz. **112**, 1584 (1997).
8. E. G. Berezhko, V. K. Elshin, and L. T. Ksenofortov, Zh. Éksp. Teor. Fiz. **109**, 3 (1996).
9. L. I. Sedov, *Methods of Similarity and Dimension in Mechanics* (Nauka, Moscow, 1972).
10. L. D. Landau and E. M. Lifshitz, *Hydrodynamics* (Nauka, Moscow, 1986).
11. I. N. Toptygin, Pis'ma Astron. Zh. **25**, 40 (1999).
12. S. I. Blinnikov, V. S. Imshennik, and V. P. Utrobin, Pis'ma Astron. Zh. **8**, 671 (1982) [Sov. Astron. Lett. **8**, 361 (1982)].

Translated by G. Rudnitskiĭ

Astronomy Letters, Vol. 26, No. 6, 2000, pp. 362–371. Translated from Pis'ma v Astronomicheskiĭ Zhurnal, Vol. 26, No. 6, 2000, pp. 427–436.

Super-Alfvén Expansion of a Nova Shell in the Magnetic Field of Its Core

S. A. Nikitin[1]*, V. A. Vshivkov[2], and V. N. Snytnikov[3]

[1] *Budker Institute of Nuclear Physics, Siberian Division, Russian Academy of Sciences, pr. Akademika Lavrent'eva 11, Novosibirsk, 630090 Russia*
[2] *Institute of Computer Technologies, Siberian Division, Russian Academy of Sciences, Novosibirsk, Russia*
[3] *Boreskov Institute of Catalysis, Siberian Division, Russian Academy of Sciences, pr. Akademika Lavrent'eva 5, Novosibirsk, 630090 Russia*

Received April 13, 1999

Abstract—We study the effect of nova magnetodipole fields on the dynamics and structure of ejected shells by using a numerical model based on the kinetic–hydrodynamic description of plasma dynamics. Our calculations show that characteristic nonuniformities appear in the distribution of field and plasma perturbations during super-Alfvén shell expansion in the circumstellar medium. *© 2000 MAIK "Nauka/Interperiodica".*

Key words: *plasma astrophysics, hydrodynamics and shock waves*

INTRODUCTION

According to an analysis of observational data for many novae, in particular, for V603 Aql (1918) and DQ Her (1934), their expanding plasma shells break up into several fragments as they evolve, among which polar clumps and equatorial belts are distinguished [1, 2]. During initial plasma expansion, the emission region is similar in shape to an ellipse elongated along the star's polar axis, with an axial ratio of 1 : 1.5 for V603 Aql. The idea of gravitational formation of ejections as matter falls onto the star from an accretion disk [3], including a magnetized one [4], was invoked to account for the asymmetric expansion of plasma from stars. However, the role of stellar intrinsic magnetic field, $\sim 10^6$–10^8 G in strength [5], in the possible redistribution of shell energy to produce jets has not been investigated. There is an as yet unstudied hypothesis that a strong magnetic field of the star affects the dynamics of the matter ejected by an explosion from its surface [1, 2].

Typically, the energy of the nova magnetodipole field (10^{38}–10^{42} erg) is much lower than the kinetic energy of the shell (10^{44}–10^{46} erg) acquired through thermonuclear heating [6]. Therefore, the hydrodynamic models of a point explosion with shock propagation from the stellar center usually disregard the effect of magnetic field on the motion of matter [7]. In this case, the shell remains spherical in shape.

The approximation of a weak magnetic field breaks down if the subsurface region, where the initial perturbations form, is taken into account. In this region, the matter with a magnetic field beneath the detaching shell is compressed. The dipole magnetic field in a relatively narrow layer can act as a "working body" with distinct anisotropic properties. The stellar magnetic field also affects the interaction of the shell with stellar wind. These peculiarities must show up in observable inhomogeneity of the ejected plasma as it moves away from the star. Here, we study this hypothesis by using our kinetic–hydrodynamic model of plasma dynamics. The model allows for the redistribution of plasma flows and makes it possible to trace the shell expansion in the magnetized medium around the star shortly after the outburst energy release.

In Section 1, we consider the magnetogravitational and electrodynamic approaches, which enable us to estimate the scale sizes of the region where the initial perturbation is formed as a function of the released energy, respectively, with and without allowance for gravitation. In the magnetogravitational approach, we determine the deformation scale size for a gravitating nonrotating sphere of an incompressible magnetized fluid. By disregarding the gravitational field, we study a superconducting shell separated from a rigid magnetic core by a vacuum gap. In this case, an energy similarity is established between these two models in equality of the relative scale sizes of the sphere deformation, on the one hand, and of the magnetic-field compression region, on the other. We discuss the characteristics of real stars in an effort to justify the physical model we propose [8]. It consists of a uniformly magnetized, perfectly conducting sphere surrounded by a thin exploding shell and a rarefied ionized gas that fills the ambient space.

* E-mail address for contacts: S.A.Nikitin@inp.nsk.su

1063-7737/00/2606-0362$20.00 © 2000 MAIK "Nauka/Interperiodica"

In Section 2, we describe a mathematical model, which is based on the kinetic approximation for ions and on the hydrodynamic approximation for electrons [9]. This model is intended to investigate the above physical system.

In Section 3, we discuss our numerical results, showing that nonuniformities appear in the distributions of field and plasma perturbations at early times of the shell motion.

1. ON THE CHOICE OF A PHYSICAL MODEL

1.1. Estimating the Deformation of a Magnetic Gravitating Incompressible Sphere by an Explosion of Its Shell

Let us consider the possible scale size of the deformation of the star itself—a white dwarf in a close binary system—by a thermonuclear explosion of the spherical hydrogen layer accreted on its surface [6]. We assume that the star has the mass $M = (0.5–1)M_\odot$, radius $R \approx 8 \times 10^8$ cm, and magnetic field $B = 10^6–10^8$ G, which are typical of novae, and ignore its own rotation. Chandrasekhar and Fermi [10] showed that a nonrotating sphere with a uniform magnetic field inside and a dipole field outside is not an equilibrium configuration under steady-state conditions and tends to flatten out, shrinking in the field direction. If the stellar matter beneath the shell is assumed to be perfectly conducting and incompressible, then we conclude that the white dwarf is deformed by the compressing effect of pressure forces through the kinetic energy $\mathscr{E}_0 \sim 10^{44}–10^{46}$ erg released during the explosion with its volume preserved. A quasi-static estimate for the scale size of this deformation can be obtained by equating part of the energy $W \sim \frac{1}{2}\mathscr{E}_0$ (approximately half of the entire energy $\mathscr{E}_0$ is assumed to move toward the stellar center) to the change in total potential energy ΔU. Following Chandrasekhar and Fermi [10], we write the equation of a deformable surface as

$$r = R + \varepsilon P_l(\cos\vartheta), \tag{1}$$

where ϑ is the polar angle in a system with the symmetry axis along the vector of uniform stellar magnetization; $P_l(\cos\vartheta)$ is the Legendre polynomial of the lth order; and ε is the amplitude of the "P_l deformation". According to the virial theorem, the total increment ΔU is equal to the sum of changes in the gravitational ($\Delta\Omega$) and magnetic ($\Delta\mathcal{M}$) energies. In particular, for $l = 2$ ($\varepsilon \ll 1$), we have

$$\Delta U = \Delta\Omega + \Delta\mathcal{M} = \frac{3}{25}\frac{GM^2}{R^3}\varepsilon^2 + \frac{7}{20}B^2R^2\varepsilon, \tag{2}$$

where $G = 6.7 \times 10^{-11}$ m^3 kg^{-1} s^{-2} is the gravitational constant. Expression (2) is written for the P_2 deformation, which is the main deformation when deriving the condition of gravitational equilibrium for a uniformly magnetized sphere formed by an incompressible medium. Such a sphere is known to be unstable and tend to take the shape of an oblate spheroid ($\varepsilon < 0$). In this case, the change in magnetic energy $\Delta\mathcal{M}$ of the second order in ε is positive for all $l \neq 2$, which rules out the system's instability against this type of perturbation. The amplitude ε ($l = 2$) can be determined from the condition of ΔU minimum and can be written in relative units as

$$\frac{\varepsilon_*}{R} = -\frac{35}{24}\frac{B^2R^4}{GM^2}.$$

It is easy to see that, for a typical white dwarf in steady state without rotation, the flattening along the magnetic axis is negligible: $|\varepsilon_*/R| \sim 10^{-11}$, $|\varepsilon_*| \sim 100$ μm!

Let us now assume that the P_2 deformation also dominate during the forced compression by a thermonuclear explosion of the shell. This assumption is based on the fact that, since the sphere is incompressible, its shape can change primarily due to the motion of internal particles along frozen-in magnetic field lines. As a result, the front velocity of the lower part of the shell, which exerts a compressing effect, varies with ϑ as $V_0\cos\vartheta$. The amount of transformed energy (i.e., the energy of shell motion along the magnetic axis) is thus estimated to be

$$\Delta W \approx \frac{W}{2}\int_0^\pi \cos^2\vartheta\sin\vartheta d\vartheta = \frac{1}{3}W.$$

The deformation scale size can be determined from the equation of energy balance

$$\Delta W = \Delta U = \Delta\Omega + \Delta\mathcal{M} \approx \Delta\Omega$$

and is [8]

$$\frac{\varepsilon_N}{R} = -\frac{5}{3}\sqrt{\frac{WR}{GM^2}} = -(10^{-3}–10^{-2}) \tag{3}$$

or $|\varepsilon_N| \sim$ 10–100 km. We take the compression to be elastic, i.e., assume that the star regains its original shape associated with a minimum of the total energy after the matter of the lower part of the shell disperses.

Our quasi-static estimate for the maximum amplitude of the star's flattening by shell explosion is determined by the gravitational energy and does not depend on the magnetic-field strength. It can be shown that this is because the equilibrium degree of deformation (ε_*) is low under steady-state conditions, or, in other words, because the contributions of the gravitation and the magnetic field to the change in potential energy are incommensurable at relatively large amplitudes $|\varepsilon| \gg |\varepsilon_*|$. Nevertheless, as follows from the above reasoning, the role of strong stellar magnetization in the development of the compression itself shows up in the pattern of deformation of the boundary surface.

Gravitation affects the general scale size of the compression region, while the spatial nonuniformity of the latter is determined by the magnetic field. Below, we use a different, even more idealized model as an example to illustrate this.

1.2. A Superconducting Shell and the Similarity Condition for Models with and without Gravitation

Let us consider a system composed of a uniformly magnetized conducting sphere with radius a and moment μ surrounded by a closed shell of inner radius r_e separated from the sphere by a vacuum gap of thickness δ_e. In the magnetostatic approximation, we can easily estimate the field configuration in this system after the shell has exploded and transformed into a perfectly conducting plasma spherical layer. The perturbed scalar potential of the field $\mathbf{H} = -\nabla\Phi$ in the gap is given by the sum $\Phi = \Phi_0 + \Phi_1$, where $\Phi_0 = \mu\cos\vartheta/r^2$ is the potential of the original field, and the perturbation potential Φ_1 is written as a series of spherical harmonics, whose coefficients can be determined from the boundary conditions

$$\frac{\partial}{\partial r}(\Phi_0 + \Phi_1)\big|_{r = r_e} = \frac{\partial}{\partial r}\Phi_1\big|_{r = a} = 0.$$

As a result, we obtain

$$\Phi_1 = \frac{\mu}{r_e^3 - a^3}\left[2r + \left(\frac{a}{r}\right)^3\right]\cos\vartheta, \quad a \le r \le r_e.$$

In a similar approach, the identity $\Phi_0 + \Phi_1 = 0$, $r \ge r_e$, holds for the region outside a shell of thickness dr_e, because the radial component of $\nabla(\Phi_0 + \Phi_1)$ vanishes on the $r = r_e + dr_e$ sphere and because $\Phi_1 \longrightarrow 0$ as $r \longrightarrow \infty$. In other words, there is no external total quasi-static field, which is tantamount to the emergence of superconductor properties in the shell. Thus, a consequence of the idealized model with an instantaneously emerging closed highly conducting shell is the screening effect of the latter, which must produce an electromagnetic impulse that propagates in all directions away from the body and that "switches off" the original external field. The fact that the initial kinetic energy of the shell plasma is much higher than the magnetodipole energy $\mathcal{M} = \mu^2/a^3$ underlies this assumption [8]. In this case, the magnetic flux is intercepted and compressed in the gap between the plasma and the body by the diamagnetic current that arises near the inner boundary of the heated layer. The magnetic pressure, which exerts a deceleration effect on the lower boundary of the shell, depends strongly on polar angle, according to the expression for the square of the field at $r = r_e$

$$H_e^2 = \frac{9\mu}{(r_e^3 - a^3)^2}\sin^2\vartheta.$$

In the approximation of a spherical front (δ_e, $\delta_e' \ll a$), the work of ponderomotive forces as the field is compressed in the gap is

$$\mathcal{A} = -\frac{1}{4}\int_0^{\pi}\int_{r_e}^{r_e'} H_e^2 r^2 dr\sin\vartheta d\vartheta \simeq \frac{\mu^2}{3a^2}\frac{(\delta_e - \delta_e')}{\delta_e\delta_e'},$$

where r_e', and δ_e' are, respectively, the shell radius and the gap thickness in the final state. Equating $\mathcal{A}$ to the shell kinetic energy W and assuming the compression to be strong ($\delta_e' \ll \delta_e$), we obtain

$$\frac{\delta_e'}{r} \simeq \left(\frac{3Wa^3}{\mu^2}\right)^{-1} = \kappa_m^{-1}.$$

The energy parameter κ_m is the ratio of the plasma-shell energy to the energy of the magnetodipole field outside a sphere of radius a. Nikitin and Ponomarenko [11] introduced this parameter to analyze the efficiency of interaction of the local-explosion plasma with a point-like magnetic dipole (in this case, a is the distance from the dipole to the point of explosion). Thus, there is an anisotropy in the magnetic-pressure distribution ($\propto \sin^2\vartheta$) in the gap, which causes deformation of the compression front. Another characteristic of the compression region is its mean scale size, specified by κ_m. A similar parameter, as applied to the gravitational energy of the sphere, can be introduced:

$$\kappa_g = \frac{5}{3}\frac{WR}{GM^2}.$$

According to the estimate (3),

$$\frac{\varepsilon_N}{R} \sim \sqrt{\kappa_g}.$$

The origin of P_2 deformation in the model of a sphere of an incompressible fluid corresponds to the angular dependence of magnetic pressure in the model of a shell with a vacuum gap. Thus, one might expect the spatial pattern of field and medium perturbations as the shell of a magnetic gravitating star explodes to be similar to the corresponding pattern in the model configuration without gravitation. The following relation serves as the similarity criterion:

$$1/\kappa_m \sim \sqrt{\kappa_g}, \tag{4}$$

when this relation is satisfied, the relative scale sizes of the perturbation region are the same in both approaches:

$$\delta_e'/a \sim \varepsilon_N/R. \tag{5}$$

The perturbation scale of the magnetic field during its compression, specified by κ_m, for novae lies in the range $1/\kappa_m \sim 10^{-2}$–10^{-8}. Thus, our estimates show that the stellar core undergoes no significant initial defor-

mations produced by compression during the shell explosion. The core remains nearly spherical. It is therefore important to consider the following question: to what extent can the deviation from a spherical shape in the shell expansion be caused by the interaction of the expanding plasma with the magnetized circumstellar medium?

1.3. Basic Characteristics of the Circumstellar Medium

Let us estimate some characteristics of the stellar surface and its ambient space from the viewpoint of peculiarities of the perturbation propagation.

The velocity of Alfvén waves in the surface layer of a white dwarf with density $\rho \sim 10^4$ g cm^{-3} [6] is $V_A = \sqrt{B^2/(4\pi\rho)} \sim 3 \times (10^6$–$10^7)$ cm s^{-1}, and the velocity of matter in a shell of mass $M_e \sim (10^{-3}$–$10^{-4})M_\odot$ for a typical nova is $V \sim \sqrt{W/M_e} \sim (10^7$–$10^8)$ cm s^{-1}. Thus, the velocity of the inner shell boundary toward the stellar center is higher than the Alfvén one. In the theory of an ideal magnetized fluid, satisfying this condition implies the emergence of strong local hydromagnetic turbulence [12]. After the action of the external impulse ceases, two oppositely directed trains of Alfvén waves, which carry away the turbulent energy from the perturbation region, must propagate along magnetic field lines. If we restrict ourselves to the hydromagnetic approximation, then this effect will be the main manifestation of anisotropic properties of the spherical surface layer in which a shock emerges.

To take into account finite compressibility, let us estimate the speed of sound in the surface layer by using the formula $S = \sqrt{\gamma P/\rho}$, where, according to [13], the pressure at the above density for steady-state conditions at minimum of the total energy is $P \sim 9.7 \times 10^{18}$ dyne cm^{-2}, and the adiabatic index is assumed to be equal to that for a nonrelativistic ideal gas ($\gamma = 5/3$). We then have $S \sim 4 \times 10^7$ cm s^{-1}. In general, the velocity of magnetosonic perturbations is given by

$$V_\pm^2 = \frac{1}{2}\left\{S^2 + V_A^2 \pm \sqrt{(S^2 + V_A^2)^2 - 4S^2V_A^2\cos^2\vartheta}\right\},$$

where the "+" and "–" signs refer to the fast and slow waves, respectively; and θ is the angle between the wave vector and the field direction. Clearly, given the estimated V_A and S, a shock wave is generated at shell velocity $V \sim 10^8$ cm s^{-1}. The jump in density is attributable to the removal of electron-gas degeneracy because of the high temperature at the shock front determined by a mean temperature of $\sim 2 \times 10^8$ K [6] in the shell at the time of explosion; in order of magnitude, this value is the critical degeneracy temperature in helium and hydrogen at densities $\sim 10^4$ g cm^{-3}.

The nova shell in a binary system expands in the stellar wind from the neighboring star. The mass flux, which causes hydrogen accumulation on the surface of the future nova, is related to the outburst period and is variously estimated to be $\dot{M} \sim (10^{-5}$–$10^{-13})\, M_\odot$ yr^{-1} [5]. We use the approximation of spherically symmetric accretion to estimate the density ρ_* and velocity of the ionized gas around the white dwarf. From the condition of flux conservation $\dot{M} = 4\pi\rho_* V_* r^2 = \text{const}$ and from the dependence of radial infall velocity V_* on radius ($V_* \propto r^{-1/2}$), we obtain $\rho_* \propto r^{-3/2}$. In particular, near the star ($r \sim R$),

$$V_* \sim \sqrt{2GM/R} \sim 6 \times 10^8 \text{ cm s}^{-1},$$

and the particle number density is

$$n_* \sim 10^9\text{–}10^{17} \text{ cm}^{-3}.$$

The derived density distribution of the background medium enables us to estimate the radius of gas-dynamical deceleration $\tilde{R}$ at which the shell mass equals the mass of the entrained stellar-wind plasma,

$$4\pi\int_R^{\tilde{R}} \rho_* r^2 dr = M_e.$$

The estimated value of $\tilde{R} \sim 4 \times (10^{13}$–$10^{19})$ cm is much larger than the stellar radius and, accordingly, the formation scale of the shell structure of interest.

Another characteristic scale is the size of the white-dwarf magnetosphere [13]. The location of a stationary shock wave in stellar wind R_A can be determined from equality of the ionized-gas infall velocity $V_*(R_A)$ and the Alfvén velocity, which depends on the star's dipole magnetic field strength $B(R_A)$ and the wind density $n_*(R_A)$: $V_* \sim B/\sqrt{4\pi\rho_*}$. It follows from the above estimates of V_*, n_*, and B that $R_A \geq 10R$. Within this scale, the original field can be assumed to be a dipole one. The shell front cannot be decelerated by the magnetic field as it moves in the rarefied medium inside the magnetosphere, because the kinetic energy W is much higher than the star's magnetodipole energy $\mathcal{M}$.

It seems most likely that the expanding shell near the nova interacts with the magnetized atmosphere of the white dwarf, which is formed at the stage immediately preceding the outburst. Calculating atmospheric parameters at distances of the order of R from the star is a separate, complex problem even for the quasi-steady-state case where hydrogen is accumulated in a degenerate surface layer [14]. We therefore restrict ourselves to qualitative reasoning, which allows the range of background-particle densities to be specified. When the temperature in the layer rises to $\sim 10^8$ K, the gas can

successively pass several states—from complete degeneracy to the onset of explosive expansion. It may well be that a substantial mass of matter with a relatively low expansion velocity compared to the particle velocity at the time of explosion outflows from the surface in this case. Assuming hydrostatic equilibrium and using the barometric formula, we find an upper limit for the atmospheric density at a distance of one radius (R) to be $n_* \sim 4 \times 10^{23}$ cm^{-3} at a scale height of $\sim 10^3$ km for a temperature of $\sim 10^8$ K at the onset of outburst development and a surface density of 10^4 g cm^{-3}. Since the above estimate of the density in accretion flow gives a lower limit, $10^9 < n_* < 10^{23}$ cm^{-3}. For definiteness, we choose a density from this range at which the local Alfvén velocity does not exceed the shell velocity. In background matter with $n_* \sim 10^{18}$–10^{19} cm^{-3} at distance R from the stellar surface with a field strength of 10^6 G, the velocity V_A is $\sim 3 \times 10^7$–8×10^6cm s^{-1}. Under such conditions, the shell motion near the nova at velocity $V \sim 10^8$ cm s^{-1} can be super-Alfvén one with the Mach–Alfvén number $M_A = V/V_A \sim 3$–10.

At large M_A, the front of a collisionless shock wave has a width of the order of the ion gyroradius $\rho_i = mcV/eB$ [15]. In our case, it is rather small, $<10^{-1}$ cm, i.e., considerably smaller than the mean free path of particles in the background plasma. In particular, the mean free path of hydrogen ions in the shell for collisions with ions of a hydrogen background of mass m and relative velocity V_r is given by

$$\lambda_{ii} = \left(\frac{mV_r^2}{2}\right)^2 \frac{1}{2\pi n_* e^4 \Lambda}.$$

At $n_* \sim 10^{18}$ cm^{-3} and V_r of the order of the shell velocity, $\lambda_{ii} \sim 10^3$ cm (the Coulomb logarithm is $\Lambda \sim 1$). Under the above conditions, the effect of collisions on the shock structure can be assumed to be marginal, and, as a result, we may use a collisionless plasma model to describe the interaction of the shell with the magnetized plasma near the nova.

Thus, in energy terms, the specific mechanism of the shell interaction with the background medium proves to be of no importance in studying the morphology of shell expansion. We can therefore choose between the hydrodynamic and kinetic–hydrodynamic (hybrid) models in favor of the latter for the reasons associated with the possibility of calculating multiflow plasma motions.

1.4. A Model with Background Plasma

In agreement with our analysis, the physical model must have the following main properties:

—the presence of a strong dipole magnetic field in which the ion gyroradius is much smaller than the size of the region under study ($\rho_i \ll a$);

—the kinetic energy of the shell particles is much larger than the magnetodipole energy ($\mathscr{E}_0 \gg \mu^2/a^3$).

—the scaling factor characterizing the compression region is $\kappa_m^{-1} < 10^{-2}$ [see (3, 5)];

—the propagation velocity of perturbations in the compression region and in outer space is lower than the shell front velocity, i.e., the corresponding Mach–Alfvén number is large;

—the gas-dynamical deceleration radius, defined as the size of the region in which the background-particle mass in the initial state is equal to the expanding-plasma mass, is much larger than the system's characteristic size ($\tilde{R} \gg a$).

The computed region in our model consists of three subregions:

—the space between the perfectly conducting surface of a uniformly magnetized sphere filled with the dense medium of the shell in its part that is not subjected to initial heating; since the model is intended for a collisionless interaction, the dense medium is simulated by a cold plasma with large Mach–Alfvén numbers ($M_A > 1$) specified for it;

—the high-temperature layer of particles in the shell with a specified initial radial-velocity distribution;

—the outer rarefied medium with a uniform density in which $M_A > 1$ near the sphere.

2. A MATHEMATICAL MODEL

The basic set of equations includes Vlasov's equation for the ion plasma component, the equations of motion, and Maxwell's equations:

$$\frac{\partial f_i}{\partial t} + \mathbf{v}\frac{\partial f_i}{\partial \mathbf{r}} + \mathbf{F}\frac{\partial f_i}{\partial \mathbf{v}} = 0,$$

$$\mathbf{F} = \frac{e}{m}\left(\mathbf{E} + \frac{1}{c}[\mathbf{v} \times \mathbf{H}]\right),$$

$$\mathbf{E} = -\frac{1}{c}[\mathbf{V}_e \times \mathbf{H}],$$

$$\mathrm{curl}\mathbf{H} = \frac{4\pi en}{c}\{\langle \mathbf{V}_i \rangle - \mathbf{V}_e\},$$

$$\mathrm{curl}\mathbf{E} = -\frac{1}{c}\frac{\partial \mathbf{H}}{\partial t},$$

where

$$n = n_e = n_i = \int f_i(\mathbf{r}, \mathbf{v}, t)dv,$$

$$\langle V_i \rangle = \frac{1}{n}\int f_i \mathbf{v} d\mathbf{v}.$$

Here, $\mathbf{E}$, $\mathbf{H}$ are the electric- and magnetic-field strengths; V_e, $\langle V_i \rangle$ are the weighted mean electron and ion velocities; and n is the ion (electron) density.

The equations of ion motion are the equations for the characteristics of the kinetic equation

$$\frac{d\mathbf{r}_i}{dt} = \mathbf{v}_i, \quad \frac{d\mathbf{v}_i}{dt} = \mathbf{F}.$$

At initial time $t = 0$ in the cylindrical region $0 \le r \le r_{max}$ and $0 \le z \le z_{max}$, there is a stationary plasma with uniform density n_* (background plasma) and a dipole magnetic field with the dipole center at point (0, 0). The external plasma does not penetrate into the central region $R < R_s$ ($R = \sqrt{r^2 + z^2}$), where the magnetic field is uniform and constant, and the ions are reflected elastically from the core at boundary R_s. A spherical shell containing N ions with total kinetic energy $\mathscr{E}_0$ is located at distance ΔR from the central part. We chose ΔR in our calculations in the range from $0.1R$ to $0.2R$. For clarity, the main plots were constructed for $\Delta R = 0.2R$. The ion velocities in the shell are distributed in the interval $[-V_{max}, V_{max}]$ following a specified law (for example, a law that ensures self-similar expansion in free space) and are directed perpendicular to the shell. In our calculations, attention was focused on the dimensionless model parameters M_A and $\mathscr{E}_0/\mathscr{M}$.

3. NUMERICAL RESULTS

We performed our calculations with the parameters typical of novae. In one of the cases, the model corresponds to the following characteristics. A stellar core of radius $R = 8 \times 10^8$ cm is magnetized to the internal uniform field strength $B = 2.6 \times 10^7$ G. The initial hydrogen ion velocities in the shell correspond to a self-similar distribution function with $V_{max} = 3 \times 10^8$ cm s^{-1}. The shell kinetic energy is $\mathscr{E}_0 = 10^{43}$ erg, and its ratio to the stellar magnetic energy $\mathscr{E}_0/\mathscr{M} \sim 10^2$ is near the lower limit for observational data. The density of the ionized hydrogen background produced by the stellar wind is 7×10^{22} cm^{-3}. The Mach–Alfvén number is $M_A = 5$ for the region near the nova surface. The results of our calculations are presented in Figs. 1–3, which show the distributions of the total density of shell and background particles in the form of sections (Fig. 1) and isolines (Fig. 2) and of magnetic field lines (Fig. 3) for time $\tilde{t} = tV_{max}/\Delta R = 4$. The system's magnetic axis is directed along the section plane in Fig. 1 and is horizontal in Figs. 2, 3, and all the succeeding figures.

As follows from Figs. 1–3, the shell boundary (the outer isoline in Figs. 2 and 3) takes a nearly elliptical shape. This boundary is determined by the fastest shell particles, whose number depends on the initial ion velocity distribution. The ellipticity of the plasma-shell boundary results from the deceleration of ions as they move at an angle to the magnetic field. Along the magnetic field, the particles fly apart freely. However, maximum density perturbations are observed near the poles, which is attributable to a superposition of the motions of the particles reflected from the sphere and of the particles directed toward the stellar surface in a narrow cone along the polar axis. The travel velocity of these maxima is appreciably lower than the initial velocity V_{max} that the particles initially moving outward exactly along the polar axis retain. Note that the latter particles are few in number. They do not cause an appreciable increase in density along the magnetic axis far from the star (Fig. 1). The plasma decelerates most effectively as it moves across the magnetic field in the region adjacent to the equatorial plane, in close agreement with the theory of a magnetolaminar mechanism for the interaction of interpenetrating ionized flows

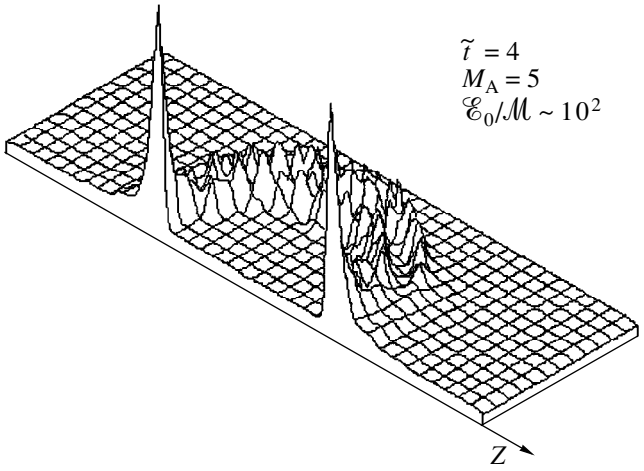

Fig. 1. Distribution of the total density of shell and background particles at time $\tilde{t} = 4$ ($M_A = 5$, $\mathscr{E}_0/\mathscr{M} \sim 10^2$).

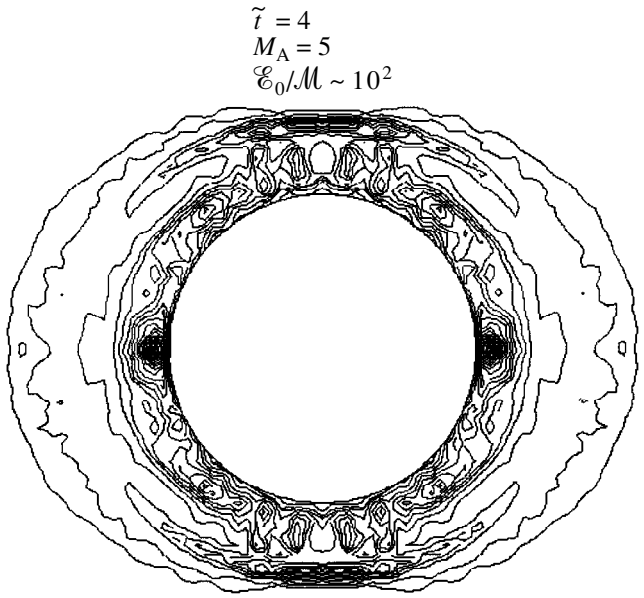

Fig. 2. Density isolines at time $\tilde{t} = 4$ ($M_A = 5$, $\mathscr{E}_0/\mathscr{M} \sim 10^2$).

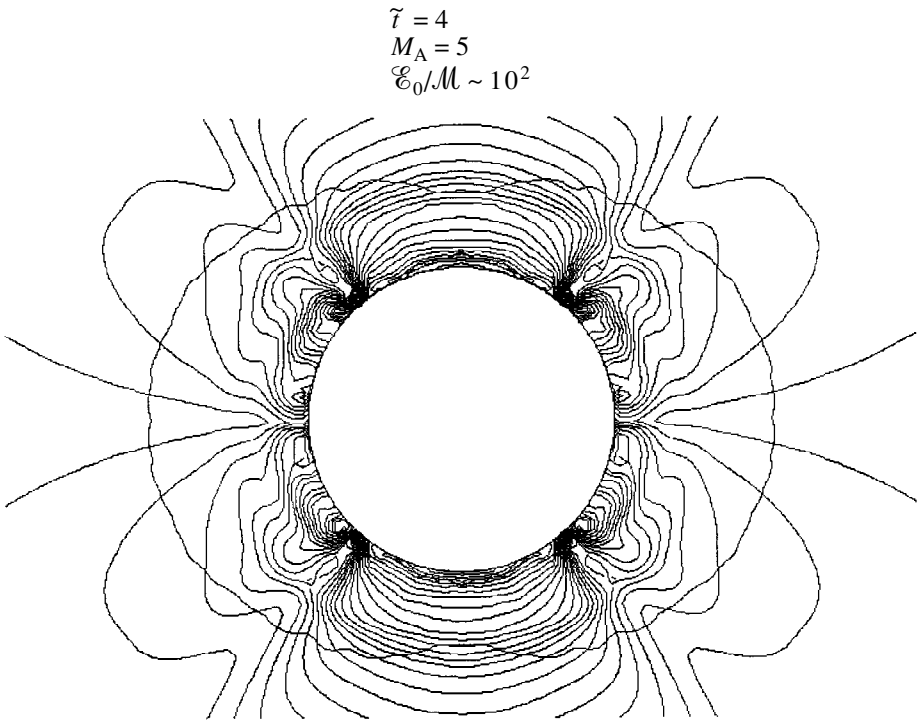

Fig. 3. Magnetic field lines at time $\tilde{t} = 4$ ($M_A = 5$, $\mathscr{E}_0/\mathscr{M} \sim 10^2$).

[16]. The deceleration gives rise to a plasma belt of enhanced density near the equator (Fig. 2). This zone of enhanced density is produced both by particles of the stellar shell and by the ions of the stellar wind entrained by the shell. The high-density equatorial zone breaks away from the stellar surface and propagates at late times as a wave through the stellar-wind plasma with a local enhancement of the interstellar magnetic field. From an observer's point of view, the motion of the equatorial part of the shell can be interpreted as the formation and propagation of a broad plasma jet. The shell plasma presses the nova magnetic field against the core surface, as can be seen from the crowding of field lines near the sphere (Fig. 3). In general, the magnetic field acquires a quadrupole symmetry in the meridional section, which is seen most clearly in the case of low shell energy. This effect vanishes as we pass to a large ratio of the shell energy to the stellar magnetic energy, $\mathscr{E}_0/\mathscr{M} \sim 10^5$.

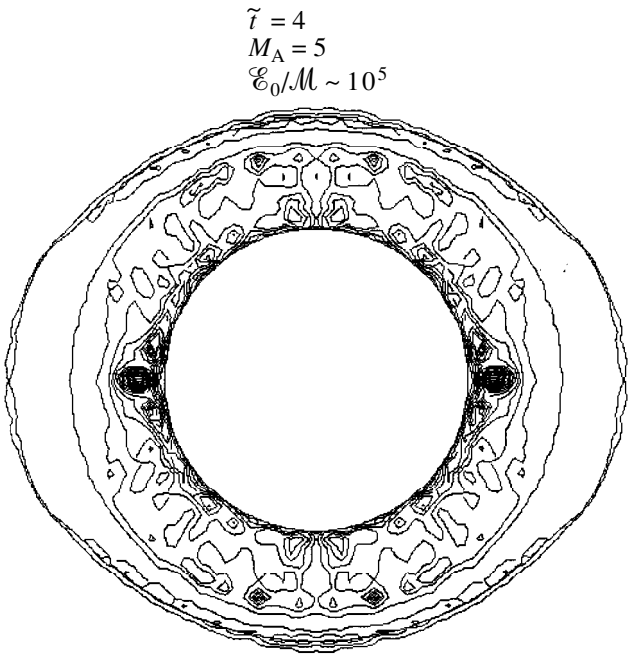

Fig. 4. Density isolines at time $\tilde{t} = 4$ ($M_A = 5$, $\mathscr{E}_0/\mathscr{M} \sim 10^5$).

We calculated the case with a large shell kinetic energy for the same Mach–Alfvén number $M_A = 5$ by increasing the number of particles in the shell by three orders of magnitude. The model corresponds to an explosion of energy $\mathscr{E}_0 = 1.5 \times 10^{43}$ erg, stellar field strength $B = 10^6$ G, a background density of 1.4×10^{21} cm^{-3}, and shell velocity $V = 3 \times 10^7$ cm s^{-1}. The results of our calculations are shown in Fig. 4 for isolines of plasma density and in Fig. 5 for magnetic field lines. It follows from Fig. 4 that the cloud boundary remains elliptical. However, the bulk of the plasma of enhanced density expands spherically, corresponding to the model of a point explosion. Individual fluctuations are attributable to the reflection of the finite number of particles used in our calculations from the sphere. The equatorial belt of enhanced density

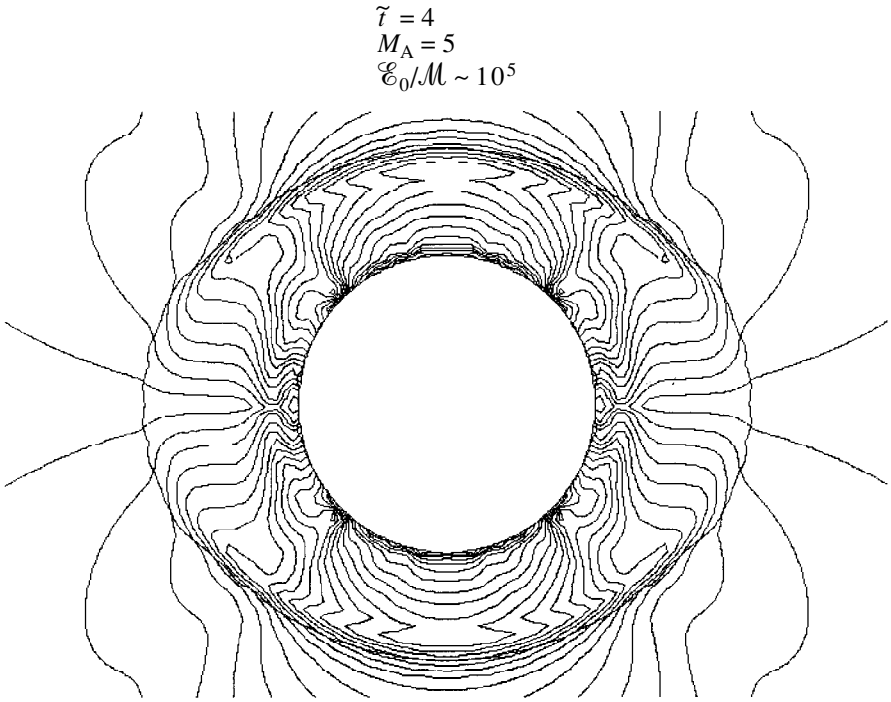

Fig. 5. Magnetic field lines at time $\tilde{t} = 4$ ($M_A = 5$, $\mathcal{E}_0/\mathcal{M} \sim 10^5$).

stretches along the boundary with the stellar wind and became less distinct against the background of the expanding shell. The magnetic field lines are compressed in this belt to form a narrow plasma sheet with the plasma motion across the magnetic field. The magnetic field inside the expanding shell tends to recover its dipole structure. Outside the boundary, the waves propagate because of the reconnection of magnetic field lines. The main region of wave generation lies at an angle of ~45° to the magnetic dipole axis and is most distinct for a low shell energy. Thus, the ratio of the shell energy to the magnetic energy is important for the formation of a nova explosion, which transforms into a spherically symmetric expansion at large values of this parameter.

Our numerical calculations revealed these features of the overall picture of exploded-shell expansion in the dipole magnetic field of the nova core for large Mach–Alfvén numbers. The results of our calculations of plasma dynamics with $M_A = 2.5$ are shown in Figs. 6 and 7. We reduced M_A by decreasing the particle velocity in the shell, which also caused the shell energy to decrease by a factor of 4. As follows from the plot of density isolines, the pattern of plasma dynamics became spherically symmetric. The distribution of magnetic field lines remains a magnetodipole one, though with distortions at the boundary between the shell and the stellar-wind plasma. The dipole magnetic field distribution exhibits an abrupt decrease in the efficiency of interaction between the expanding plasma flow and the ambient medium. Indeed, as the Mach–Alfvén number decreases to 2 or 3, the magnetolaminar mechanism of interaction between the plasma flows changes to the mechanism of interaction with the magnetic field [16–18]. In this case, the energy is lost through magnetosonic and Alfvén waves. However, the

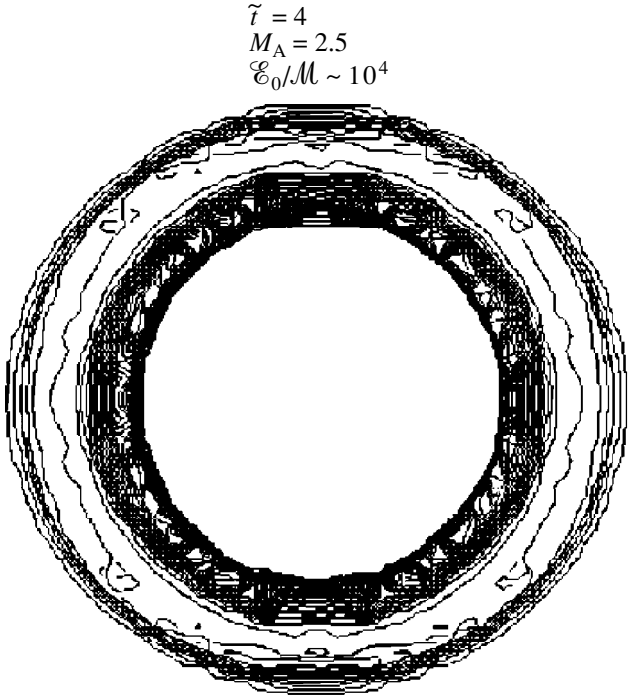

Fig. 6. Density isolines at time $\tilde{t} = 4$ ($M_A = 2.5$, $\mathcal{E}_0/\mathcal{M} \sim 10^4$).

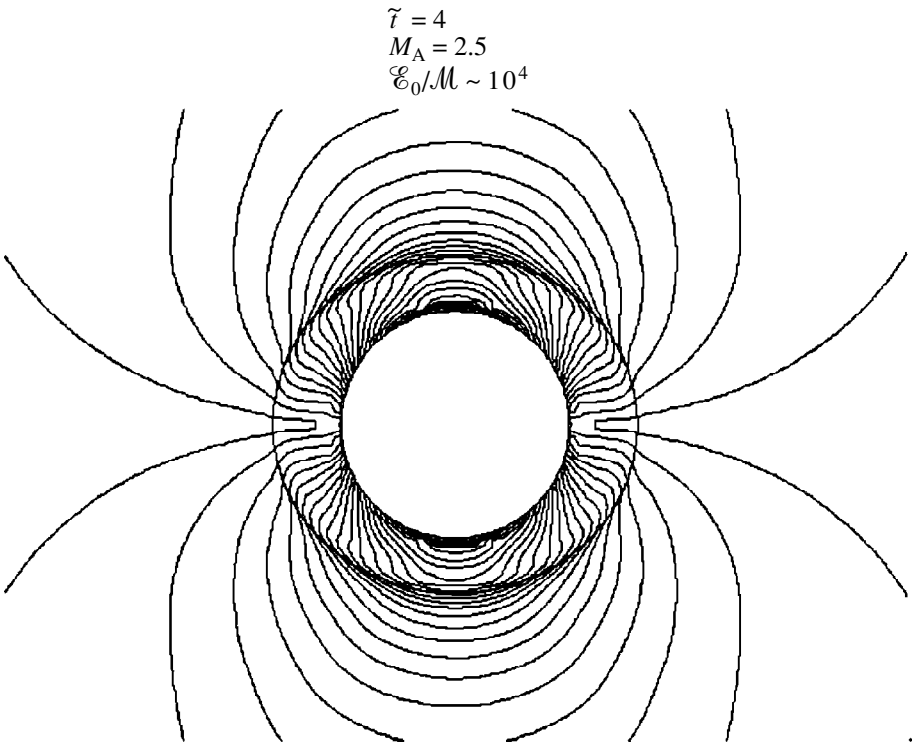

Fig. 7. Magnetic field lines at time $\tilde{t} = 4$ ($M_A = 2.5$, $\mathscr{E}_0/\mathscr{M} \sim 10^4$).

decline of the magnetic field during plasma expansion away from the star causes the Alfvén velocity to decrease. As a result, the waves do not go outside the expanding shell, and it expands as a whole.

Turning to astronomical data [1], we conclude that such morphological features are observed during the development of nova outbursts. Note that changes in other model parameters, in particular, the spatial broadening of the initial shell-particle distribution to size ΔR causes no qualitative change in the pattern of plasma dynamics.

CONCLUSION

Our model shows the emergence of nonuniformities, which are similar in symmetry properties and structure to the observed pattern of nova-shell expansion. Shell expansion depends on two basic parameters: the Mach–Alfvén number and the ratio of shell energy to stellar magnetodipole energy. The Mach–Alfvén number determines the mechanism of plasma interaction with a magnetized stellar wind. For the magnetolaminar mechanism, the energy ratio acts as a dimensionless scale, which also affects the observed properties of expansion at fixed M_A. A further development of the model and its verification require astrophysical data with a determination of the above dimensionless parameters and using methods of laboratory simulations of nonsteady cosmic phenomena.

ACKNOWLEDGMENTS

We wish to thank A.G. Ponomarenko, G.I. Dudnikova, and Yu.P. Zakharov for the stimulating interest in the study and for helpful discussions. This study was supported by the Russian Foundation for Basic Research (project no. 97-02-18471).

REFERENCES

1. A. A. Bojarchuk and E. R. Mustel, Astrophys. Space Sci. **6**, 183 (1970).
2. E. R. Mustel', Astron. Zh. **33**, 182 (1956).
3. M. A. Gol'dshtik and V. N. Shtern, Dokl. Akad. Nauk SSSR **304**, 1069 (1989).
4. D. L. Meler, S. Edgington, P. Godon, *et al.*, Nature **388**, 350 (1997).
5. M. Livio, A. Shankar, and J. M. Truran, Astrophys. J. **330**, 264 (1988).
6. S. Starrfield, J. W. Truran, and W. M. Sparks, Astrophys. J. **226**, 186 (1978).
7. B. C. Low, Astrophys. J. **261**, 351 (1982).
8. S. A. Nikitin, V. A. Vshivkov, and V. N. Snytnikov, Vychisl. Tekhnol. **3** (4), 65 (1998).
9. V. A. Vshivkov, G. I. Dudnikova, and Yu. I. Molorodov, Vychisl. Tekhnol. **4** (10), 103 (1995).
10. S. Chandrasekhar and E. Fermi, Astrophys. J. **118**, 116 (1953).

11. S. A. Nikitin and A. G. Ponomarenko, Zh. Prikl. Mekh. Tekhn. Fiz., No. 6, 3 (1993).

12. E. Parker, *Cosmical Magnetic Fields (Their Origin and Their Activity)* (Oxford, Clarendon Press, 1979; Mir, Moscow, 1982).

13. G. S. Bisnovatyĭ-Kogan, *Physical Problems in Stellar Evolution Theory* (Nauka, Moscow, 1989).

14. D. Mihalas, Stellar Atmospheres (Freeman, San Francisco, 1978; Mir, Moscow, 1982)

15. V. A. Vshivkov, G. I. Dudnikova, Yu. I. Molorodov, and M. P. Fedoruk, Vychisl. Tekhnol. **2** (4), 5 (1997).

16. V. P. Bashurin, A. I. Golubev, and V. A. Terekhin, Zh. Prikl. Mekh. Tekhn. Fiz., No. 5, 10 (1983).

17. Yu. A. Berezin, V. A. Vshivkov, G. I. Dudnikova, and M. P. Fedoruk, Fiz. Plazmy **18**, 812 (1992).

18. Yu. P. Zakharov, A. M. Orishich, A. G. Ponomarenko, and V. G. Posukh, Fiz. Plazmy **12**, 1170 (1986).

Translated by V. Astakhov

Astronomy Letters, Vol. 26, No. 6, 2000, pp. 372–378. Translated from Pis'ma v Astronomicheskiĭ Zhurnal, Vol. 26, No. 6, 2000, pp. 437–443.

A Study of the Shell of Nova V705 Cas

V. P. Arkhipova*, M. A. Burlak, and V. F. Esipov

Sternberg Astronomical Institute, Universitetskiĭ pr. 13, Moscow, 119899 Russia

Received July 5, 1999

Abstract—Spectroscopic observations of the DQ Her-type Nova V705 Cas in the wavelength range Hγ–7400 Å at the nebular stage are presented. The Balmer decrement yields $E_{B-V} = 0.98$. Based on statistical relationships, we estimated E_{B-V} to be 0.7 and the distance to the Nova to be 1.17 kpc. The discrepancy between the estimates of E_{B-V} may result from circumstellar reddening after the formation of a dust shell. The helium, oxygen, nitrogen, argon, iron, and calcium abundances in the Nova shell are determined. The shell of V705 Cas is similar in chemical composition to those of other DQ Her-type novae. © *2000 MAIK "Nauka/Interperiodica".*

Key words: *novae, spectroscopic observations, shells, chemical composition*

INTRODUCTION

Since Nova V705 Cas, which was discovered in 1993, exhibited a deep minimum on the descent of its light curve, it can be classified as being of the DQ Her type. The deep minimum is associated with the formation of a dust shell. The dust formation was confirmed by IR spectroscopic and photometric observations [1], as well as by UV spectra [2].

We constructed an overall V light curve (Fig. 1) by using visual and photoelectric estimates of different authors taken from IAU circulars, as well as photoelectric [3, 4] and photographic observations [5].

Here, based on emission-line intensities, we determine the abundances of several elements in the Nova shell. Data on the chemical composition of nova shells are of great importance in understanding the nature of white dwarfs that are members of novae, in particular, in estimating their masses.

INTERSTELLAR EXTINCTION AND DISTANCE

We used the light curves to determine the following parameters of the Nova: the V magnitude at maximum light $m_{V_{\max}} = 6\overset{m}{.}4$; the B magnitude at maximum light $m_{B_{\max}} = 6\overset{m}{.}6$; the time of brightness decline by 2^m below the maximum $t_{2V} = 62^{\mathrm{d}}$; the rate of early brightness decline $d = 0.03\ m\ \mathrm{d}^{-1}$; and the V magnitude 15 days after the maximum $m_V(15) = 6\overset{m}{.}85$.

Based on statistical relationships between the decline rate of the Nova and its absolute magnitude at maximum light, we estimated its distance. We used Parenago–Sharov's [6] statistical method to estimate the interstellar extinction. Using the M_V–t_{2V} relation [7], assuming that all novae have the same absolute magnitude $M_{V_{\max}} = -5\overset{m}{.}6$ 15 days after the maximum, and using the relation [8] between the B magnitude of a nova at maximum light and its decline rate, we obtained the following distance and interstellar-extinction estimates for V705 Cas:

$$r = 1.24\ \text{kpc},\ A_V = 2\overset{m}{.}34,\ E_{B-V} = 0.73\ (\text{from } t_{2V});$$

$$r = 1.14\ \text{kpc},\ A_V = 2\overset{m}{.}18,\ E_{B-V} = 0.68\ (\text{from } m_V(15));$$

$$r = 1.12\ \text{kpc},\ A_V = 2\overset{m}{.}15,\ E_{B-V} = 0.67\ (\text{from } d).$$

We finally adopted $\langle r \rangle = 1.17$ kpc, $\langle A_V \rangle = 2\overset{m}{.}2$, and $\langle E_{B-V} \rangle = 0.7$.

The distance to V705 Cas was also estimated by other authors. El'kin [9] obtained the following values: $r = 880$ pc from the equivalent width of the interstellar Ca II λ3933 Å line; $r = 940$ pc from polarimetric observations; and $r = 1350$ pc and $E_{B-V} = 0.67$ from photometric data. Hauschildt *et al.* [10] obtained three distance estimates: $r = 3$–6 kpc from interstellar Na I and Mg II lines; $r = 2$ kpc from the $M_{V_{\max}} - t_{2V}$ and $M_{V_{\max}} - t_{3V}$ relations by assuming $E_{B-V} = 0.5$; and $r = 3.2$ kpc by assuming that the magnitude of V705 Cas at maximum was equal to the magnitude of DQ Her at maximum. Using statistical relations, the distance to the Nova was also determined by Hric *et al.* [3], $E_{B-V} = 0.56$ and $r = 1.67$ kpc, and by Lynch *et al.* [11], $r = 1246$ pc.

* E-mail address for contacts: vera@sai.msu.su

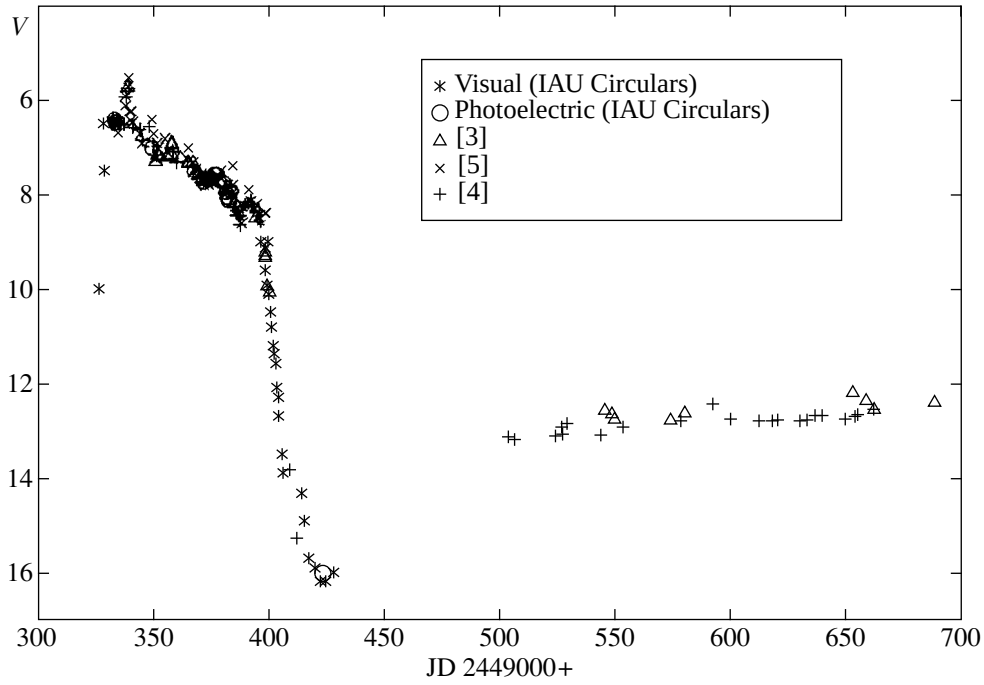

Fig. 1. The *V* light curve of V705 Cas.

Eyres *et al.* [12] performed radio observations in July 1995. They found r = 2.5 kpc for V705 Cas from the angular size of its shell.

Below, we determine the interstellar extinction from the Balmer decrement: $A_V = 3^m.1$, $E_{B-V} = 0.98$. This discrepancy may stem from the fact that the dust in the Nova shell had not yet dispersed by the beginning of our observations.

The Nova is moderately fast, as suggested by t_{2V}.

SPECTROSCOPIC OBSERVATIONS OF V705 Cas AND REDUCTION OF ITS SPECTRA

We obtained spectra of the Nova in Cassiopeia with an optically efficient spectrograph attached to the 1.25-m reflector at the Crimean station of the Sternberg Astronomical Institute The detectors were SBIG ST-6 242 × 375 CCD arrays. The spectral resolution with a 600 lines mm^{-1} diffraction grating was ~6 Å pixel^{-1}. The wavelength range covered was 4200–7500 Å. The total spectrum of the Nova consisted of two partially overlapping frames corresponding to different rotation angles of the grating. The spectral range of each frame was ~2000 Å.

We carried out our observations during five nights in the summer and fall of 1994: on July 15, August 2, September 5, October 2, and November 1. At this time, the Nova brightness was constant, ~13^m, and it was already at the nebular stage. Apart from V705 Cas, we also observed two standard stars, which were used to reduce the spectra: 50 Boo and BD+ 16°3972 (B6V, E_{B-V} = 0.4).

We performed a preliminary reduction of the spectra by using the ST6 program provided with the CCD array. The standard stars were used to correct the spectra for the CCD spectral response and for atmospheric extinction. The spectra were not corrected for the airmass difference (which, however, did not exceed 0.1). We calibrated the spectra by means of the ESIP.EXE and KOEF.EXE programs written by A.M. Tatarnikov. For the subsequent reduction, we used the SPE program written by S.G. Sergeev at the Crimean Astrophysical Observatory. Figures 2 and 3 show the spectrum of V705 Cas taken on November 1, 1994.

The line intensities were determined by using the SPE program.

We inferred the interstellar extinction from the Balmer decrement. The results are given in Table 1. Since Hγ was blended with the λ4363 Å [OIII] line, the color excesses derived from this line are less reliable. We took the mean color excess to be E_{B-V} = 0.98 and used this value to correct the intensities of all lines for interstellar reddening. They are given in Table 2.

We estimated the mean error in the line intensities to be 30%, but for lines with relative intensities of a few hundredths, it can reach 50–100%.

ELECTRON DENSITY AND ELECTRON TEMPERATURE IN THE SHELL OF V705 Cas

The [OIII] line intensity ratio $R(N_e, T_e) = I(\lambda 4959 + \lambda 5007)/I(\lambda 4363)$ at a late nebular stage is used to determine T_e in nova shells. N_e can be estimated by using the critical densities of forbidden lines. The critical density

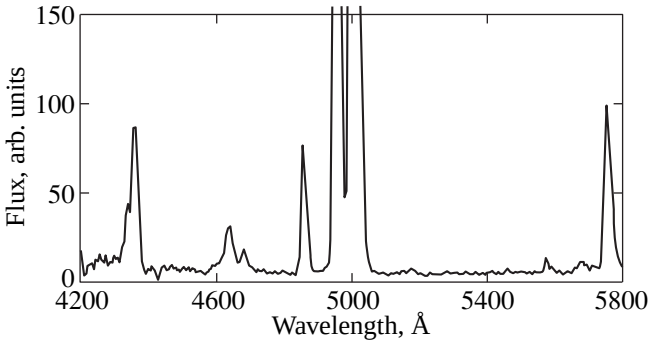

Fig. 2. The spectrum of V705 Cas in the wavelength range 4200–5800 Å taken on November 1, 1994.

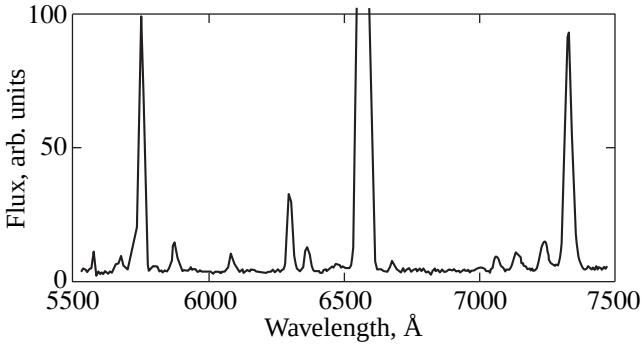

Fig. 3. The spectrum of V705 Cas in the wavelength range 5500–7500 Å taken on November 1, 1994.

for the auroral 4363 Å line is 10^7 cm^{-3}. Preliminary estimates using forbidden lines show that the temperature and electron density decreased only slightly during the observations. We therefore assumed their values to be constant and equal to $T_e = 10^4$ K and $N_e = 10^7$ cm^{-3}, respectively, in the subsequent computations. The $R(N_e, T_e)$ ratios over the observing period are also given in Table 2.

Table 1. The color excess estimated from the Balmer decrement

Color excess	July 15	August 12	September 5	October 2	November 1
E_{B-V}(Hα)	0.91	1.00	0.97	1.02	1.00
E_{B-V}(Hγ)	1.22	1.23	1.21	0.65	0.39:

Table 2. The line intensities relative to Hβ and the $R(N_e, T_e)$ ratio

Line	July 15	August 12	September 5	October 2	November 1
Hγ	0.42	0.42	0.42	0.55	0.63
Hβ	1	1	1	1	1
Hα	2.56	2.82	2.73	2.91	2.83
4363 [O III]	2.53	2.53	2.05	1.73	1.83
4640 N III	0.93	0.58	0.76	0.81	0.78
4686 He II	0.39	0.30	0.33	0.21	0.30
4959 [O III]	3.30	3.65	4.24	4.92	5.49
5309 [Ca V]			0.01		
5411 He II		0.02			
5680 N II	0.05	0.08	0.06	0.06	0.07
5721 [Fe VI]		0.04			
5755 [N II]	0.77	0.84	0.82	0.85	0.81
5801 C IV		0.03	0.02	0.03	0.03
5876 He I	0.09	0.11	0.08	0.08	0.09
6086 [Fe VII]	0.05	0.04	0.04	0.04	0.05
6300 [O I]	0.16	0.18	0.17	0.18	0.17
6364 [O I]	0.07	0.08	0.06	0.06	0.06
6678 He I			0.02	0.03	0.02
7006 [Ar V]			0.01		
7065 He I	0.04	0.04	0.03	0.03	0.03
7135 [Ar III]	0.03	0.04	0.03	0.04	0.05
7235 [Ar IV]	0.07	0.07	0.06	0.06	0.07
7320+7330 [O II]	0.42	0.46	0.42	0.46	0.48
$R(N_e, T_e)$	5.05	5.59	8.03	11.04	11.65

DETERMINING THE CHEMICAL COMPOSITION FOR THE SHELL OF V705 Cas

For the total abundance of any element to be derived, all the ionization stages possible at given N_e and T_e of the gas in the shell must be taken into account. The total abundance is the sum over all ionization states of the element in question, and the unobserved ionization states are taken into account by using the ionization correction factor ICF.

The relative ion abundance can be deduced from the intensities of observed recombination lines:

$$\frac{N(X^{i+})}{N(H^+)} = \frac{\lambda(X^{i+})}{\lambda(H\beta)}\frac{\alpha^{\rm eff}(H\beta)}{\alpha^{\rm eff}(\lambda)}\frac{I(\lambda)}{I(H\beta)} = X(T_e)\frac{I(\lambda)}{I(H\beta)},$$

where $\alpha^{\rm eff}(H\beta)$ and $\alpha^{\rm eff}(\lambda)$ are the effective recombination coefficients, and $I(H\beta)$ and $I(\lambda)$ are the intensities of the corresponding lines.

We used the FIVEL program written by de Robertis *et al.* [13] to determine the elemental abundances from forbidden lines. This program computes volume emission coefficients for the forbidden lines and Hβ at given T_e and N_e.

1. Helium

The total helium abundance is the sum of the He^0, He^+, and He^{++} abundances. The unobserved He^0 state is ignored, because all helium in the Nova shell is assumed to be ionized. In this case, we have

$$\frac{He}{H} = \frac{He^+}{H^+} + \frac{He^{++}}{H^+}.$$

We determined the He^+ abundance from the He I λ5876 and λ6678 Å lines. Given the temperature dependence of $X(T_e)$, we derived the following relation for these lines [14]:

$$\log\frac{N(He^+)}{N(H^+)} = -0.133 + 0.235\log t_e + \log\frac{I(\lambda5876)}{I(H\beta)},$$

$$\log\frac{N(He^+)}{N(H^+)} = 0.851 + 0.216\log t_e + \frac{0.0158}{t_e} + \log\frac{I(\lambda6678)}{I(H\alpha)},$$

where $t_e = T_e/10^4$ K.

We determined the He^{++} abundance from the λ4686 Å line [14]:

$$\log\frac{N(He^{++})}{N(H^+)} = -1.077 + 0.135\log t_e + \log\frac{I(\lambda4686)}{I(H\beta)}.$$

To deduce the true abundance of He^+ required allowance for collisional excitation of the metastable $2s^2{}^3S$ level of He I. The method of allowance is described in [15]. The derived ion and total helium abundances are given in Table 3. As the He^+ abundance, we took a weighted mean of the values inferred from the He I λ5876 and λ6678 Å lines with weights 2 and 1, respectively (for those cases where both lines were observed). The helium abundance averaged over the period of observations was taken to be ⟨He/H⟩ = 0.082.

Table 3. The helium abundance in the shell of V705 Cas

Date	He^+/H^+			He^{++}/H^+	He/H
	λ5876 Å	λ6678 Å	mean	λ4686 Å	
July 15	0.054		0.054	0.033	0.087
August 12	0.067		0.067	0.025	0.092
September 5	0.049	0.054	0.050	0.028	0.078
October 2	0.049	0.066	0.054	0.018	0.072
November 1	0.060	0.058	0.058	0.025	0.083

2. Oxygen

The oxygen abundance can be determined from the relation [14]

$$\frac{O}{H} = \left[\frac{O^+(\lambda7320 + \lambda7330) + O^{++}(\lambda4959)}{H^+(H\beta)}\right]\frac{He}{He^+}\ [14],$$

where the He/He^+ ratio is taken as the ICF. We estimated the oxygen abundance by using all available lines of various ions, namely, λ6300 Å [O I], λ7330 Å [O II], λ4959 Å [O III], and λ4363 Å [O III]. The total oxygen abundance is then equal to the sum over three ionization states:

$$\frac{O}{H} = \frac{O^0}{H^+} + \frac{O^+}{H^+} + \frac{O^{++}}{H^+}.$$

This is a lower limit on the oxygen abundance, because we did not took into account the higher ionization stages. However, it is hoped that, even if O^{+++} or ions of higher ionization stages are present in the Nova shell, they are very few in number, and we allowed for the prevailing states of oxygen. We used the FIVEL program to determine the abundances of all ions from forbidden lines. The O^{++} abundance was deduced from two lines: [O III] λ4363 and λ4959 Å. The results are given in Table 4. We took the mean oxygen abundance to be $\langle O/H\rangle = 5.9 \times 10^{-3}$. Note that, after applying the above ionization correction, we obtained $\langle O/H\rangle = 5.5 \times 10^{-3}$, in good agreement with the previous result.

3. Nitrogen

We determined the nitrogen abundance by using all measurable lines, namely, [N II] λ5755 Å, N II λ5680 Å,

Table 4. The oxygen abundance in the shell of V705 Cas

Date	O^{++}/H^+, 10^{-3}		O^+/H^+, 10^{-4}	O^0/H^+, 10^{-4}	O/H, 10^{-3}
	λ4363 Å	λ4959 Å	λ7330 Å	λ6300 Å	
July 15	6.7	5.5	4.6	2.1	6.6
August 12	6.7	6.0	5.0	2.4	6.9
September 5	5.4	7.0	4.6	2.3	7.2
October 2	4.6	8.1	5.1	2.4	7.7
November 1	4.8	9.1	5.2	2.4	8.5

and N III λ4640 Å. The lower limit on the total nitrogen abundance was then estimated as follows:

$$\frac{N}{H} = \frac{N^+(\lambda5755) + N^{++}(\lambda5680) + N^{+++}(\lambda4640)}{H^+(H\beta)},$$

where for permitted lines:

$$\frac{N^{i+}}{H^+} = X_i(T_e)\frac{I(\lambda)}{I(H\beta)},$$

and the function $X_i(T_e)$ can be represented as

$$X_i(T_e) = \chi_0 t^\eta, \quad t = T_e/10^4 \text{ K}.$$

The coefficients χ_0 and η are tabulated in [16]:

$$\lambda5680: \chi_0 = 0.205, \eta = -0.41;$$

$$\lambda4640: \chi_0 = 0.014, \eta = -0.71.$$

We computed the N^+ abundance by using the FIVEL program. The mean nitrogen abundance was taken to be $\langle N/H\rangle = 2.5 \times 10^{-2}$. The results of our calculations are given in Table 5.

4. Argon

We determined the argon abundance by using the FIVEL program from two lines of different ions: [Ar III] λ7135 Å and [Ar IV] λ7235 Å and, for September 5, also [Ar V] λ7006 Å. A lower limit on the argon abundance was estimated as follows:

$$\frac{Ar}{H} = \frac{Ar^{++}(\lambda7135) + Ar^{+++}(\lambda7235) + Ar^{++++}(\lambda7006)}{H^+(H\beta)}.$$

The mean argon abundance was taken to be $\langle Ar/H\rangle = 2 \times 10^{-5}$. The results of our calculations are given in Table 6.

Table 5. The nitrogen abundance in the shell of V705 Cas

Date	N^+/H^+, 10^{-4}	N^{++}/H^+, 10^{-2}	N^{+++}/H^+, 10^{-2}	N/H, 10^{-2}
July 15	7.2	1.0	1.3	2.4
August 12	7.8	1.5	0.81	2.4
September 5	7.7	1.1	1.1	2.3
October 2	7.9	1.3	1.1	2.5
November 1	7.6	1.5	1.1	2.7

5. Iron

The iron abundance is commonly determined by using the formula

$$\frac{Fe}{H} = \left[\frac{Fe^{5+}(\lambda5176) + Fe^{6+}(\lambda6086)}{H^+(H\beta)}\right]\frac{He}{He^{++}}$$ [17].

Since only the [Fe VII] λ6086 Å line was measurable in our spectra, we could only place a lower limit on the iron abundance. We determined the Fe^{6+} abundance by using the relation from [18]:

$$\frac{N(Fe^{6+})}{N(H^+)} = \frac{\varepsilon(H\beta)N_e}{nA(\lambda)h\nu}\frac{I(\lambda6086)}{I(H\beta)} = X(T_e, N_e)\frac{I(\lambda6086)}{I(H\beta)},$$

where $\varepsilon(H\beta)$ is the volume emission coefficient for Hβ, $A(\lambda)$ is the emission probability, and $n(^1D) = \frac{N(Fe^{6+\,1}D_2)}{N(Fe^{6+})}$ is tabulated in the above paper.

The mean iron abundance was taken to be $\langle Fe/H\rangle = 1.6 \times 10^{-5}$. The results are given in Table 7.

6. Calcium

We had only one calcium line, [Ca V] λ5309, at our disposal, which could be measured only in the Septem-

Table 6. The argon abundance in the shell of V705 Cas

Date	Ar^{++}/H^+, 10^{-6}	Ar^{+++}/H^+, 10^{-6}	Ar^{4+}/H^+, 10^{-6}	Ar/H, 10^{-5}
July 15	0.97	21		2.2
August 12	1.1	21		2.2
September 5	0.97	17	0.24	1.8
October 2	1.2	16		1.7
November 1	1.4	19		2.0

Table 7. The iron abundance in the shell of V705 Cas

Date	Fe^{6+}/H^+, 10^{-6}	Fe/H, 10^{-5}	Date	Fe^{6+}/H^+, 10^{-6}	Fe/H, 10^{-5}
July 15	5.4	1.4	October 2	4.9	2.0
August 12	4.1	1.5	November 1	6.1	2.0
September 5	5.1	1.4			

Table 8. The chemical composition of V705 Cas, some other novae, and the Sun

Element, log$N$	Sun [14]	V705 Cas	DQ Her [19]	DQ Her [20]	QV Vul [14]
He	11.00	10.9	10.85	11.15	11.04
N	7.98	10.4	9.57	10.45	9.04
O	8.91	9.8	9.56	10.38	9.58
Ar	6.57	7.3	–	–	–
Ca	6.34	5.8	7.49	–	–
Fe	7.53	7.2	–	–	7.36

ber 5 spectrum. We determined the Ca^{4+} abundance from the formula:

$$\frac{N(Ca^{4+})}{N(H^+)} = 2.6\times10^{-6}E^0_{4,2}\sqrt{t}\times10^{\frac{1.14}{t}}\frac{I(\lambda5309)}{I(H\beta)},$$

$$E^0_{4,2} = 1.24t^{-0.87}\ [14].$$

The Ca^{4+} abundance was estimated to be $\langle Ca^{4+}/H\rangle = 5.8\times10^{-7}$.

CONCLUSION

The first reliable determinations of elemental abundances in nova shells showed their chemical composition to differ from the solar one primarily by the helium and CNO abundances. Subsequently, O–Ne–Mg novae with enormous neon overabundances were discovered.

The helium abundance that we derived for V705 Cas does not exceed the solar value. This may be because the ejected shell contained mainly matter from the unevolved cool component of the binary. The oxygen and nitrogen abundances that we deduced for V705 Cas do not differ markedly from their estimates for other novae and exceed the solar values. The argon abundance in the shell of V705 Cas exceeds the solar value; we obtained only a lower limit. The iron abundance is nearly solar, but this is again a lower limit. The adopted calcium abundance is highly uncertain, because it was derived from a single measurement of a very weak line.

Table 8 gives the chemical composition in the shell of V705 Cas we inferred, the solar chemical composition, and the chemical composition of the shells around two other novae: DQ Her and QV Vul. Nova QV Vul, like V705 Cas, is distinguished by a deep minimum on its light curve and can therefore be classified as being of the DQ Her type.

REFERENCES

1. M. Kidger, N. Devaney, K. Sahu, and S. López, IAU Circ., No. 5936 (1994).
2. S. N. Shore, S. Starrfield, P. Hauschildt, *et al.*, IAU Circ., No. 5938 (1994).
3. L. Hric, K. Petrik, Z. Urban, and D. Hanzl, Astron. Astrophys., Suppl. Ser. **133**, 211 (1998).
4. K. Kijewski, B. E. Martin, T. Foster, and D. P. Hube, J. R. Astron. Soc. Can. **89**, 43 (1995).
5. U. Munary, T. V. Tomov, A. Antonov, *et al.*, Intern. Bull. Var. Stars, No. 4005 (1994).
6. A. S. Sharov, Astron. Zh. **40**, 900 (1963).
7. J. G. Cohen, Astrophys. J. **292**, 90 (1985).
8. S. van den Bergh and C. J. Pritchet, Publ. Astron. Soc. Pacif. **98**, 110 (1986).
9. V. G. El'kin, Pis'ma Astron. Zh. **21**, 750 (1995) [Astron. Lett. **21**, 670 (1995)].

10. P. H. Hauschildt, S. Starrfield, S. N. Shore, *et al.*, Astron. J. **108**, 1008 (1994).
11. D. K. Lynch, R. W. Russell, R. C. Kellogg, *et al.*, Astron. J. **113**, 1391 (1997).
12. S. P. S. Eyres, R. J. Davis, M. F. Bode, and H. M. Lloyd, IAU Circ., No. 6296 (1996).
13. M. M. de Robertis, R. J. Dufour, and R. W. Hunt, J. R. Astron. Soc. Can. **81**, 195 (1987).
14. L. H. Aller, *Physics of Thermal Gaseous Nebulae* (D. Reidel, Dordrecht, 1984).
15. R. E. S. Clegg, Mon. Not. R. Astron. Soc. **229**, 31 (1987).
16. V. V. Golovatyj, A. Sapar, T. Feklistova, and A. F. Kholtygin, Astron. Astrophys. Trans. **12**, 85 (1997).
17. J. Andrea, H. Drechsel, and S. Starrfield, Astron. Astrophys. **291**, 869 (1994).
18. H. Nussbaumer and P. J. Storey, Astron. Astrophys. **113**, 21 (1982).
19. S. R. Pottasch, Ann. Astrophys. **22**, 412 (1959).
20. R. E. Williams, N. J. Woolf, E. K. Hege, *et al.*, Astrophys. J. **224**, 171 (1978).

Translated by A. Dambis

Astronomy Letters, Vol. 26, No. 6, 2000, pp. 379–389. Translated from Pis'ma v Astronomicheskiĭ Zhurnal, Vol. 26, No. 6, 2000, pp. 444–455.

Porous Dust Grains in the Shells of Herbig Ae/Be Stars

V. B. Il'in[1]* and N. A. Krivova[1, 2]

[1] *Astronomical Institute, St. Petersburg State University, Bibliotechnaya pl. 2, Petrodvorets, 198904 Russia*
[2] *Max Planck Institute of Aeronomy, Katlenburg-Lindau, Germany*

Received September 24, 1999; in final form, December 20, 1999

Abstract—The transfer of polarized radiation in inhomogeneous circumstellar shells with a spheroidal spatial distribution of porous dust particles is computed. The grains are modeled by an MRN mixture of silicate and graphite particles. The optical properties of porous particles (considered separately in the Appendix) are computed by using effective medium theory and Mie theory. The following observational characteristics have been computed for WW Vul, a typical Herbig Ae star with Algol-like minima: the spectral energy distribution from the ultraviolet to the far infrared, the color–magnitude diagrams, the wavelength dependence of linear polarization, and the shell brightness distribution. The effect of grain porosity on the results is considered. It has been found that only moderate particle porosity (the volume fraction of matter is f ~ 0.5) can explain available observational data in terms of the approach used. Since radiation pressure must rapidly sweep submicron-sized grains out of the vicinity of Herbig Ae/Be stars, we briefly discuss how particle porosity can affect this process. © *2000 MAIK "Nauka/Interperiodica".*

Key words: *stars—circumstellar shells, interstellar dust*

1. INTRODUCTION

Herbig Ae/Be (HAeBe) stars are young stars of moderate mass (2–8 $M_\odot$), which appear to be the precursors of Vega- and β Pic-type main-sequence stars surrounded by gas–dust protoplanetary disks. Considerable infrared (IR) excesses commonly observed in HAeBe stars are generally explained by thermal dust radiation. However, it is unlikely that dust particles can form in the shells of these stars, while strong radiation pressure makes it difficult for dust grains to exist near the stars for long. Circumstellar dust is assumed to be the remnant of a protostellar cloud and is continuously supplied to the inner shell layers by comet-like bodies [1]. The presence of dust around Vega- and β Pic-type stars can be explained in a similar way [2, 3].

When modeling the shells around HAeBe stars, only compact dust particles have always been considered (see, e.g., [4–8]). Meanwhile, many of the existing models for interstellar dust suggest a certain grain porosity (see [9] and references therein). Note that the hypothesis of particle porosity in the disk around β Pic allows available observational data to be interpreted in a more consistent way [10, 11]. The presumably low albedo of circumstellar particles [12] can also be evidence that the dust grains in the vicinity of HAeBe stars are not compact.

Here, we consider the influence of particle porosity on the observational manifestations of circumstellar dust: the IR spectrum, the circumstellar extinction curves, the color variations during brightness minima (for UX Ori-type HAeBe stars), the wavelength dependence of polarization, and the shell brightness distribution. Our shell model and the representation of porous dust grains in it are described in Section 2; the results of our calculations are presented and discussed in Section 3. The Appendix contains figures that show how porosity affects the optical properties of silicate and graphite particles of difference sizes.

2. MODEL

2.1. Porous Dust Grains

To describe the optical properties of circumstellar dust grains, we used the MRN model by Mathis *et al.* [13], to which we added one more parameter, particle porosity p (the fraction of the particle volume occupied by vacuum). Thus, two types of dust grain were assumed to be simultaneously present in the shell: graphite and silicate ones. Both are spherical and have the same power-law size distribution

$$n(a) \sim a^{-q}, \quad (1)$$

* E-mail address for contacts: vi2087@vi2087.spb.edu

where q is a constant. The model parameters also include the largest and smallest particle sizes, $a_{\min}$ and $a_{\max}$, as well as the ratio (by number) of silicate particles to graphite ones, n_{Si}/n_C. Here, we do not discuss advantages and disadvantages of the MRN model. Note only that this is one of the existing models for interstellar dust, with each having its own difficulties in explaining the entire set of available direct and indirect data on interstellar grains (see, e.g., [14, 15]). Nevertheless, it is the MRN model that has been used virtually always in calculations similar to ours.

We determined the optical properties of porous grains by using effective medium theory (EMT) and Mie theory. In other words, a porous particle was replaced by a compact homogeneous sphere with some mean refractive index $\langle m \rangle$. The latter was calculated by using Bruggeman's rule [16]

$$(1-p)\frac{m_1^2 - \langle m \rangle^2}{m_1^2 + 2\langle m \rangle^2} + p\frac{m_0^2 - \langle m \rangle^2}{m_0^2 + 2\langle m \rangle^2} = 0, \qquad (2)$$

where m_1 is the refractive index of silicate or graphite (in both cases, the refractive indices were taken from [17]), and $m_0 = 1$ is the refractive index of vacuum. Note that EMT has a wide range of applicability (see, e.g., [16, 18, 19]).

Some optical parameters of silicate and graphite particles that we calculated by using EMT and Mie theory are shown in the figures in the Appendix. The optical properties of the MRN grain aggregates considered here can also be inferred from them.

2.2. Dust Distribution in the Shell

The dust in the shell was assumed to have a spheroidal spatial distribution,

$$n(\mathbf{R}) = n_0[\sqrt{R_x^2 + R_y^2 + R_z^2(A/B)^2}]^{-\alpha}, \qquad (3)$$

where R_x, R_y, R_z are the coordinates of radius vector $\mathbf{R}$, A/B is the flattening (axial ratio) of spheroidal equidensites, and n_0 and α are constants. The angle between the line of sight and the equidensite symmetry axis is i.

There is a dust-free spherical zone of radius R_{in} at the shell center. We determined R_{in} by taking into account the fact that the temperature of the grains at this distance from the star cannot exceed their sublimation temperature (about 1500 K). The outer radius R_{out} of the dust shell was chosen to be constant (4.7×10^3 AU). Its value affects weakly the radiation fluxes in the spectral range under consideration ($\lambda < 100$–300 μm).

We emphasize that, although the shell in our model is spherical, its dust distribution is not spherically symmetric. For this reason, the total radiation emerging from the shell is polarized, and the degree of its polarization depends on A/B and on other model parameters.

2.3. Method of Calculation

We computed the transfer of polarized radiation in the shell by the Monte Carlo method using the program developed by Fischer [20].

The grain temperatures at various distances from the star required for such calculations were determined for a simplified shell model with a spherically symmetric dust distribution,

$$n(R) = n_0' R^{-\alpha} \qquad (4)$$

and with the same sizes and mass as those of the shell with the spherodical distribution given by (3). This approximation is accurate enough (see, e.g., [21]). Below, the shell models with the dust distributions given by (3) and (4) are called, respectively, spheroidal (or two-dimensional) and spherically symmetric (or one-dimensional).

We simulated the transfer of unpolarized radiation in the spherically symmetric shell by using Kruegel's program described in [22]. The changes required to realize the chosen model were made to both programs (see [21] for more detail).

2.4. Brightness Minima

Several HAeBe stars (UX Ori, WW Vul, etc.) exhibit Algol-like minima, which are accompanied by characteristic color and polarization variations [23, 24]. In the currently most popular hypothesis, the minima of UX Ori-type stars are associated with eclipses of the stars by circumstellar clumps of gas and dust ([24, 25]; see, however, [26]). As a result, at minimum light, the fraction of the radiation scattered in the shell increases, and, hence, the star + shell system becomes bluer, while the degree of linear polarization increases, in general agreement with observations (see [24] and references therein).

Clearly, the observed color and polarization variations in this hypothesis must be determined mainly by the properties, amount, and distribution of circumstellar dust in the inner shell layers. Recall that the same layers give a major contribution to the IR spectrum (except the far infrared) and to circumstellar extinction and scattering. We therefore modeled both the spectral energy distribution and the color and polarization variations in terms of the hypothesis described above. Simple relations, for example, those from [27, 28], were used to calculate the latter.

3. RESULTS OF THE CALCULATIONS AND THEIR DISCUSSION

Here, we did not set the objective of comprehensively interpreting the observational data for a specific HAeBe star listed in the Introduction. Instead, we chose a typical shell model and varied the grain porosity in it. Subsequently, a comparison of the results for shells with the same sizes (and optical depths for visi-

ble absorption τ_V^{abs}) revealed the main effects of grain noncompactness.

We chose the model of the shell around WW Vul proposed by Friedemann *et al.* [29] as the basic model. This model is well developed and satisfactorily accounts for the observed IR spectrum. Other models of this dust shell have similar parameters [7, 28].

3.1. Spectral Energy Distribution

Figure 1 shows our computed spectral energy distributions for the spherically symmetric (one-dimensional) model of the shell around WW Vul ($T_* = 9500$ K, $L_* = 80\,L_\odot$)) at various circumstellar particle porosities ($p = 0$, 0.3, and 0.6). The model parameters $R_{in} = 2.7$ AU, $R_{out} = 4.7 \times 10^3$ AU, $\alpha = 1.45$, $n_{Si}/n_C = 1.12$, $q = 3.5$, $a_{min} = 0.005$ μm, and $a_{max} = 0.32$ μm were fixed; only n_0 was varied with p to keep the optical depth τ_V^{abs} constant, which allowed us not to violate satisfactory agreement between the observed and theoretical IR spectra. Note that varying A/B alone affects weakly the shape of the IR spectrum for shells of the same mass [21]. In general, the variations in the above parameters of the spherically symmetric shell are also insignificant if τ_V^{abs} is constant [12, 30].

It is easy to see that, as the grain porosity p increases from 0 to 0.6, the peak in the IR spectrum, while maintaining its magnitude, shifts longward (from 2.5 to 4.5 μm), and a dip is formed in the energy distribution at $\lambda \approx 1.5$–2 μm. In addition, the emission bands at λ 10 and 20 μm become less distinct, and the spectral slope in the far infrared ($\lambda > 60$ μm) slightly decreases. These spectrum transformations are mainly attributable to changes in the grain temperature and in the relative contribution of graphite and silicate particles to the object's IR radiation as the grain porosity increases.

Note that, as p increases further from 0.7 to 0.97, the peak in the IR spectrum is enhanced and shifts shortward (from 4.5 to 2.5 μm). In this case, the dip in the spectrum at $\lambda \approx 1.5$–2 μm is preserved, while the intensity of the emission bands at λ 10 and 20 μm slightly increases. The change in the behavior of the curves at $p \approx 0.6$–0.7 results from an abrupt change in the optical properties of porous graphite particles in the infrared (cf. Figs. 6 and 7 in the Appendix).

Recall that porous grains are more or less compact particles with insignificant vacuum inclusions for $p \longrightarrow 0$ and most likely an assembly of small subparticles for $p \longrightarrow 1$ (see, e.g., [31]). The optical properties of silicate and graphite particles vary with p differently, at least in the EMT approximation (see Figs. 6–9 in the Appendix), and, as a result, the pattern of variations in the grain temperature and, consequently, in the emission spectra with porosity proves to be fairly complex for the MRN mixture of particles.

The far-IR shell spectrum is mainly determined by Q_{abs}/a, where Q_{abs} is the absorption efficiency, and a is the grain size. Variations of Q_{abs}/a with particle porosity p have been repeatedly considered previously (see, e.g., [32]), while the influence of grain porosity on the profile of the λ 10 μm silicate band was discussed by Hage and Greenberg [31] and Henning and Stognienko [33] (see also Fig. 8 in the Appendix).

Note also that, if we fix all shell parameters except p and n_0, then the mass of the circumstellar dust, which gives approximately the same IR flux, first decreases with increasing p and then increases (a minimum at $p \approx 0.6$–0.7). For example, for a shell with the parameters from Subsection 3.1, the IR flux is approximately the same at $M_{sh} = 6.6 \times 10^{-6}\,M_\odot$ (for $p = 0$), $3.9 \times 10^{-6}\,M_\odot$ ($p = 0.65$), $8.3 \times 10^{-6}\,M_\odot$ ($p = 0.97$), etc. Such an effect was noted by Mathis [34] when searching for a minimum of the dust mass required to explain the observed interstellar extinction in the Galaxy.

The behavior of the ultraviolet (UV) spectrum can be better traced in Fig. 2, which shows the so-called circumstellar extinction curve—the wavelength dependence of extinction in the shell. Note that the extinction in this case is defined as the difference between the flux from the object (star + shell) and the flux from the star without a shell and differs from the extinction by dust on the line of sight [6].

Since the circumstellar extinction curve is not known for WW Vul, Fig. 2 shows the results obtained from the observations of the star NX Pup by Tjin A Djie *et al.* [35]. NX Pup ($T_* = 9500$ K, $L_* = 100\,L_\odot$) closely resembles WW Vul, and its circumstellar extinction curve is more or less typical of HAeBe stars (see, e.g., the curve for AB Aur in [4]).

As we see from Fig. 2, the peak at λ2200 Å weakens and shifts longward as p increases from 0 to 0.6. As p increases further (from 0.7 to 0.97), a significant change occurs, as in the case of the IR spectrum: the peak is enhanced and shifts shortward, with the rise in the far ultraviolet ($1/\lambda > 6.2\ \mu m^{-1}$) becoming very steep (see Fig. 8 in the Appendix). Note, however, that these results must be treated with caution. It is unclear whether EMT is applicable to those cases where the size of particle inhomogeneities is comparable to or larger than the wavelength of the radiation, which is quite possible in the far ultraviolet.

3.2. Color–Magnitude Diagrams

Figure 3 shows our computed diagrams for the photometric U, B, V, R, and I bands. For comparison, we present the results of observations for WW Vul at one of the minima [36].

We found the theoretical curves to monotonically displace downward and to the right as p increases; this tendency is also preserved for $p > 0.6$. This is because an increase in grain porosity, with the grain size being preserved, usually causes the albedo to decrease (see,

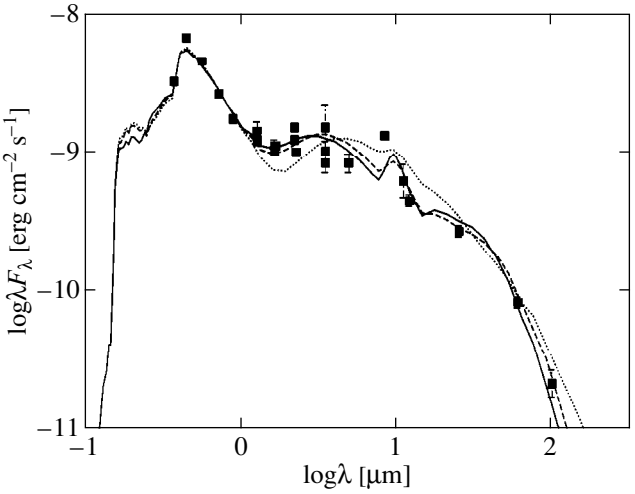

Fig. 1. Spectral energy distributions for a spherically symmetric model of the shell around WW Vul at various grain porosities: $p = 0$ (solid line), $p = 0.3$ (dashed line), and $p = 0.6$ (dotted line). The squares represent observational data from [54–58].

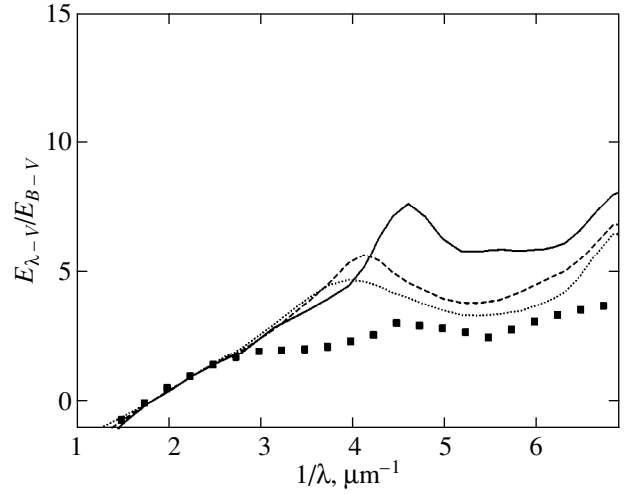

Fig. 2. Circumstellar extinction curves for a spherically symmetric model of the shell around WW Vul at various grain porosities. The notation is the same as in Fig. 1. The squares represent data for NX Pup from [35].

e.g., [31] and Fig. 9 in the Appendix). At the same time, the ensemble-averaged grain albedo $\langle\Lambda\rangle$ determines the fraction of the scattered radiation in the object's total radiation (for optically thin shells). For the same thermal radiation, porous grains therefore scatter starlight worse than do compact particles; accordingly, the star tracks in the color–magnitude diagram are less deformed, i.e., deviate less from the initial straight lines that they must be in the absence of scattered radiation.

For compact grains ($p = 0$), the theoretical curves run well away from the observational points, which we pointed out in [12]. We also showed that the problem could be solved if $\langle\Lambda\rangle \approx 0.3$–$0.4$ in the visible range. Recall that interstellar grains and, consequently, the standard MRN mixtures used for their representation have $\langle\Lambda\rangle \approx 0.5$–$0.7$ (see, e.g., [37]).

Circumstellar-particle porosity can explain the low albedo in a natural way. However, there are also other possibilities to achieve agreement between the theoretical and observed spectra and diagrams simultaneously, for example, by attributing ~50% of the observed near-IR flux that we did not took into account to the radiation of gas and/or very small grains (see, e.g., [38, 39]) or by assuming that the dust in the shell concentrates mainly in optically thick clumps [40, 41]. In addition, for shells without spherical symmetry, the ratio of the total scattered flux to the thermal flux from circumstellar dust can depend strongly not only on the mean particle albedo, as was shown above, but also on the shell orientation relative to the observer (inclination i). Recall that the fraction of the scattered light emerging from an optically thin oblate shell in the direction of the equatorial plane is usually larger than that from the poles, because the scattering is anisotropic and because the dust distribution is nonspherical (see, e.g., [42]). When a spheroidal shell is observed at different inclinations i to the symmetry axis, the scattered flux therefore increases with i, while the thermal flux, which is essentially isotropic, is preserved.

When the grains scatter radiation only forward, i.e., when the asymmetry factor of the phase function is $\langle\cos\Theta\rangle = 1$, the following simple relation clearly holds for the i dependence of the total scattered flux emerging from a shell with the dust distribution (3) toward the observer:

$$F_{\rm sh}(i) = F_{\rm sh}(90)\left[\sin^2 i + \left(\frac{A}{B}\right)^2\cos^2 i\right]^{-\alpha/2}. \qquad (5)$$

It shows that, for very oblate shells ($A/B \gg 1$) observed nearly edge-on ($i \sim 90°$), the dependence of $F_{\rm sh}$ on i must be appreciable, $F_{\rm sh}(i) \sim \left(\frac{\pi}{2} - i\right)^{-\alpha}$, because α is expected to be ~1.5–2. The flux ratio is $F_{\rm sh}(0)/F_{\rm sh}(90) = (A/B)^{-\alpha}$ and differs markedly from 1.

The asymmetry factor of the phase function $\langle\cos\Theta\rangle$ for particles of the MRN mixture in the visible range is close to 1, and formula (5) can be of use. Our calculations confirm that, in general, the dependence of $F_{\rm sh}$ on i follows relation (5), although $\langle\cos\Theta\rangle < 1$ and the optical depth $\tau \sim 1$.

It should be noted that the effect of orientation of a nonspherical shell relative to the observer clearly cannot be invoked to account for the difficulty in simultaneously interpreting the IR spectra and the color–magnitude diagrams (the "excess" scattered flux in models). It can hardly be assumed that only shells seen at an angle to their equatorial plane (for example, $|90° - i| > 20°$) and, hence, with a deficit of scattered radiation are observed. For a random distribution of the shell symmetry planes in space, the number of shells seen nearly

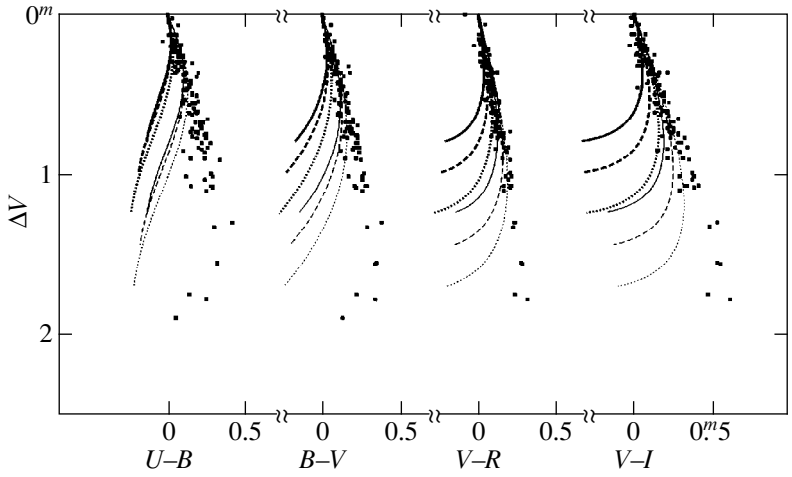

Fig. 3. Color–magnitude diagrams for the *UBVRI* bands for a spheroidal model of the shell around WW Vul. The heavy and normal lines are for inclinations $i = 90°$ and 70°, respectively; the remaining notation is the same as in Fig. 1. The squares represent observational data for WW Vul at minimum light from [36].

edge-on ($|90° - i| < 10°$) and, consequently, without this deficit must always be significant.

Note, on the other hand, that the scattered-to-stellar flux ratio F_{sh}/F_* determines the position of the turning point of the star track in the color–magnitude diagram (see [12]). At large A/B, F_{sh}/F_* depends strongly on i [see, e.g., formula (5)], and the tracks must turn at markedly different levels of brightness decline (ΔV) for different stars. If the tracks for a large group of UX Ori-type objects had been available, then we could have inferred the flattening of their scattering dust shells (spherical or disk-like ones).

3.3. Linear Polarization

Although the linear-polarization variations in the object (star + shell) observed during minima are considerable, they are satisfactorily described by the following approximate relation [36]:

$$\mathbf{P}_{obs}(\Delta m) \approx \mathbf{P}_{is} + \mathbf{P}_{sca} \times 10^{0.4\Delta m}, \qquad (6)$$

where Δm is the change in magnitude; and $\mathbf{P}_{obs}$, $\mathbf{P}_{is}$, and $\mathbf{P}_{sca}$ denote, respectively, the object's observed polarization, the interstellar polarization (including the polarization produced by dust extinction on the line of sight in the shell), and the polarization produced by the scattered radiation of the shell. The latter can be represented as

$$P_{sca} = \frac{\sqrt{Q_{sh}^2 + U_{sh}^2}}{I_{tot}(\Delta m = 0)} = P_{sh}\frac{I_{sh}}{I_{tot}(\Delta m = 0)}, \qquad (7)$$

where I_{sh}, Q_{sh}, and U_{sh} are the Stokes parameters for the scattered radiation emerging from the shell; $P_{sh} = \sqrt{Q_{sh}^2 + U_{sh}^2}/I_{sh}$, $I_{sh}/I_{tot}(\Delta m = 0)$ is the fraction of the scattered radiation in the object's total radiation at maximum light; and $I_{tot}(\Delta m = 0) = I_* \exp(-\tau^{ext}) + I_{sh}$, where I_* is the stellar radiation, and τ^{ext} is the optical depth of the shell for absorption (along the line of sight).

The wavelength dependence of linear polarization $P_{sca}(\lambda)$ can give additional important information about the properties of circumstellar dust. The curves in Fig. 4 indicate this dependence computed for models with $A/B = 5$ at various grain porosities ($p = 0$, 0.3, and 0.6). Note that P_{sca} monotonically decreases as the porosity increases further ($p > 0.6$). The points in Fig. 4 represent the values taken from [36], where they were determined from the observed values by using relation (6).

It should be noted that, although the computed P_{sca} are in satisfactory agreement with the observed ones (see Fig. 4), the polarization of the scattered radiation from the shell P_{sh} at $p \approx 0$–0.3 turns out to be considerably smaller than its estimates that can be obtained from observations. The reason is that the theoretical ratio $I_{sh}/I_{tot}(\Delta m = 0)$ in formula (7) is clearly overestimated for models with such porosities p, as the corresponding tracks in the color–magnitude diagram show (see Fig. 3).

The case of a shell with $A/B = 5$ we chose corresponds to a nearly maximum P_{sh} [21, 42]. Since P_{sh} rapidly decreases with p (for $p > 0.7$), we conclude that models with a large particle porosity can hardly explain the observed polarization in UX Ori-type stars.

Shells with a disk-like dust distribution (for example, a dust disk in the shape of a sphere without polar cones, which one might expect when a magnetic field does not govern the motion of grains, and they are swept out of the inner shell layers almost radially by stellar radiation) can have a slightly higher degree of polarization P_{sh}. Nevertheless, our estimates show that no disk-like dust distribution (for the representation of porous grains we used) can give a considerably larger

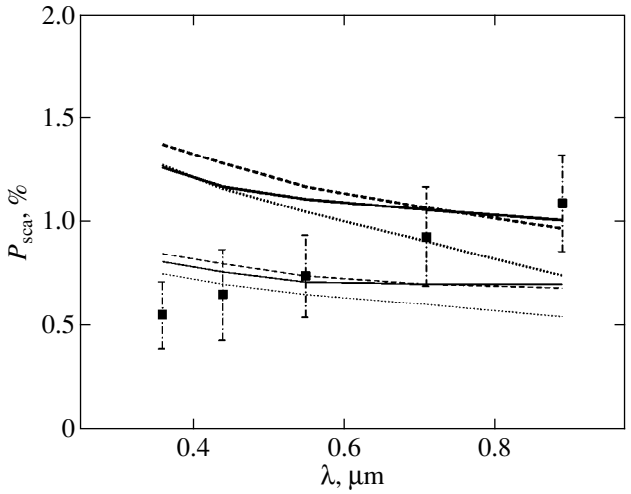

Fig. 4. Wavelength dependence of linear polarization for a spheroidal model of the shell around WW Vul. The notation is the same as in Fig. 3. The squares represent data for WW Vul from [36].

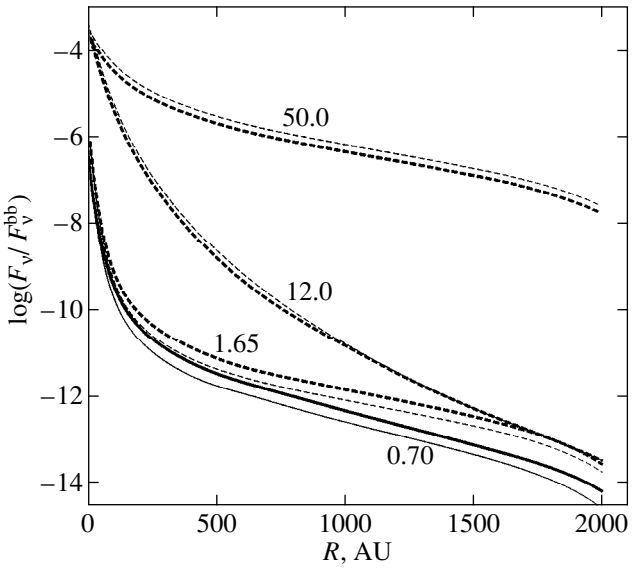

Fig. 5. Brightness distributions at various wavelengths for a spheroidal model of the shell around WW Vul. The heavy and normal lines are for $p = 0$ and 0.6, respectively. F_ν^{bb} is the flux from a blackbody of temperature $T_* = 9500$ K.

P_{sh} than that for the very oblate spheroidal shells we considered and can thus explain the results of our observations.

3.4. Shell Brightness Distribution

To the best of our knowledge, as yet no sufficiently detailed maps of the brightness distribution have been obtained for the shells of HAeBe stars with minima; however, they should be considered as observational tests, which will be possible in the near future. Figure 5 shows the brightness distributions at several wavelengths ($\lambda = 0.7$, 1.65, 12, and 50 μm) computed for two models with particle porosities $p = 0$ and 0.6. The fluxes from the peripheral regions of the shells with porous grains are seen to be a factor of 3–5 lower than those for the shells with compact grains. This is because the phase function for porous particles is generally more elongated forward than that for compact particles (see, e.g., [43] and Fig. 9 in the Appendix).

Polarization maps with a sufficiently high spatial resolution are unlikely to be obtained for UX Ori-type stars in the immediate future. We therefore do not provide and do not discuss here our computed distributions of the polarization parameters over the shell image. Note that they are mainly determined by other parameters than the porosity of circumstellar dust particles (see [44] for more detail).

3.5. Radiation Pressure on Dust

It should be noted that the mere assumption that comet-like bodies supply grains to the inner shell layers does not yet completely solve the problem of submicron-sized grains being present in them—the radiation pressure of HAeBe stars is strong enough to set such a high rate of dust outflow from the shell that it cannot be offset even by the complete breakup of all comet-like bodies near the star [45]. A magnetic field of a certain geometry can slow down the sweeping out of charged grains but cannot change radically the situation [46]. It is therefore of interest to consider how grain porosity can affect the efficiency of their sweeping out of the vicinities of HAeBe stars.

The effect of particle porosity on the radiation-pressure force was discussed in detail by Mukai *et al.* [47] for a rather peculiar model of circumsolar dust grains (fractal aggregates of subparticles). We consider this effect in terms of the representation of porous grains used.

The radiation-pressure force is known to be

$$F_{pr} = \frac{1}{c}\frac{R_*^2}{R^2}\sigma T_*^4 \bar{C}_{pr}, \qquad (8)$$

where $\bar{C}_{pr}$ is the flux-averaged radiation-pressure cross section, R_* and T_* are the stellar radius and temperature, R is the distance from the star to the particle, c is the speed of light, and σ is the Stefan–Boltzmann constant. For silicate and even for graphite at $p > 0.5$, the effective complex refractive index is $(\langle m\rangle - 1) \sim f$, where $f = 1 - p$ is the filling factor of a porous grain. For $x = 2\pi a/\lambda < 0.1$–1, which includes a substantial part of the integration range when averaging the cross section in (8), $C_{pr} \approx 16\pi^2 a^3 \mathrm{Im}(\langle m\rangle - 1)/(3\lambda) \sim a^3 f$, where λ is the wavelength of the incident radiation. Thus, the radiation-pressure force is approximately the same for particles of the same mass but of different porosity and rapidly

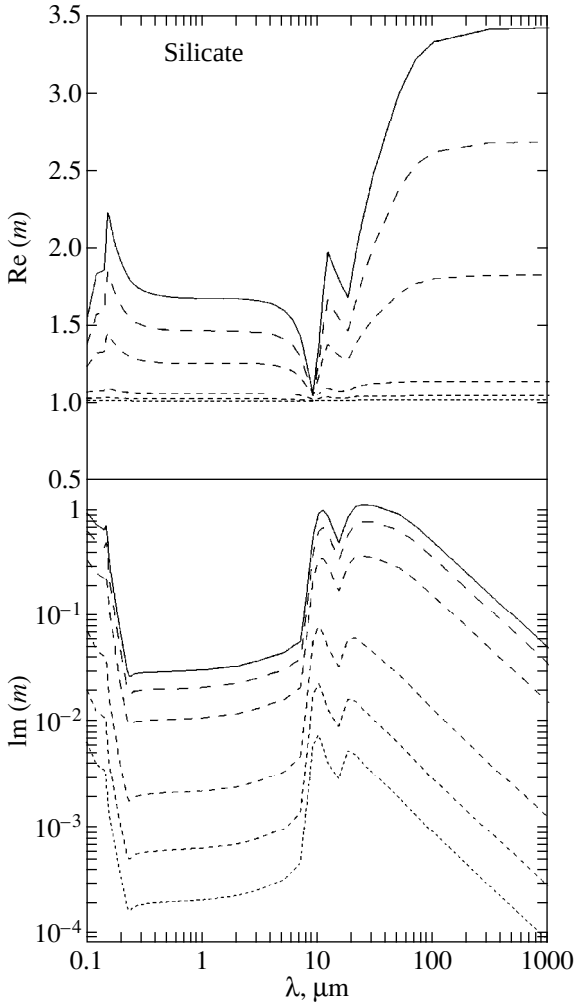

Fig. 6. Complex refractive index m for mixtures of astronomical silicate with vacuum. The porosities are $p = 0$ (solid lines), 0.3, 0.6, 0.9, 0.97 (dashed lines), and 0.99 (dotted lines).

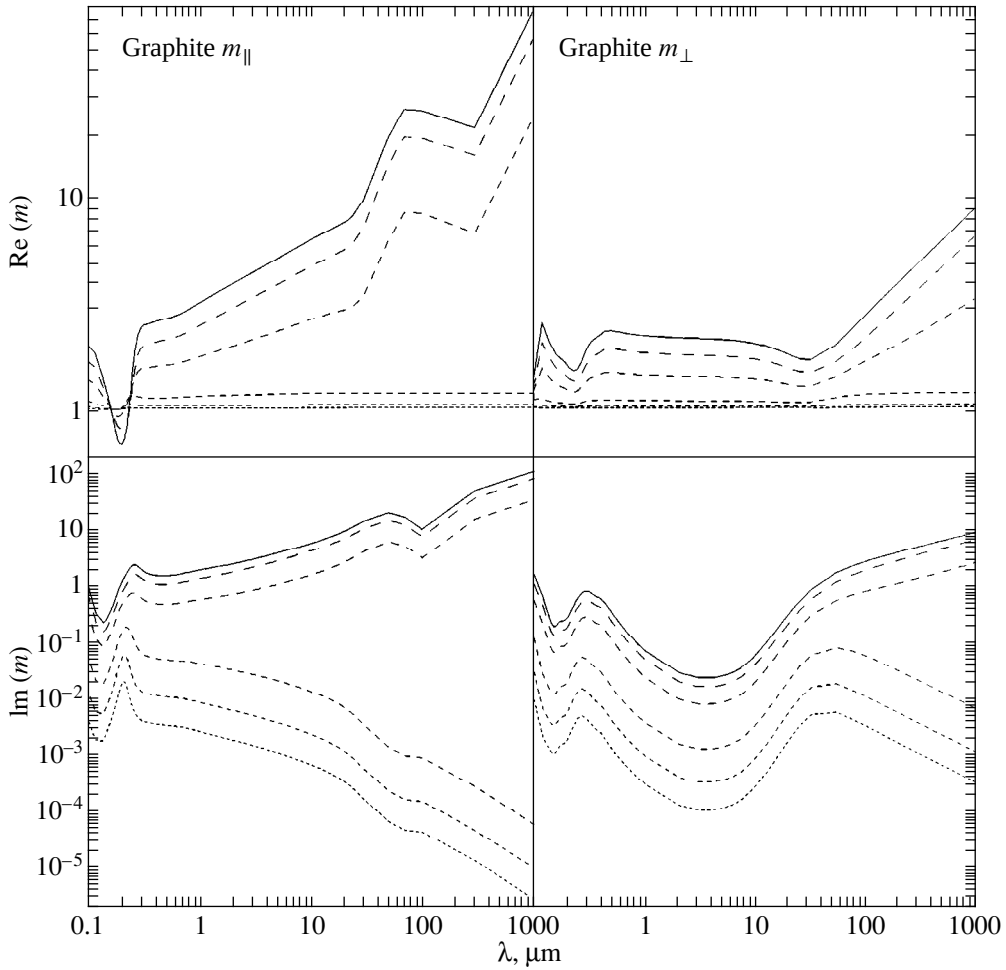

Fig. 7. Same as Fig. 6 for graphite in the case of m = $m_{\parallel}$ and $m = m_{\perp}$.

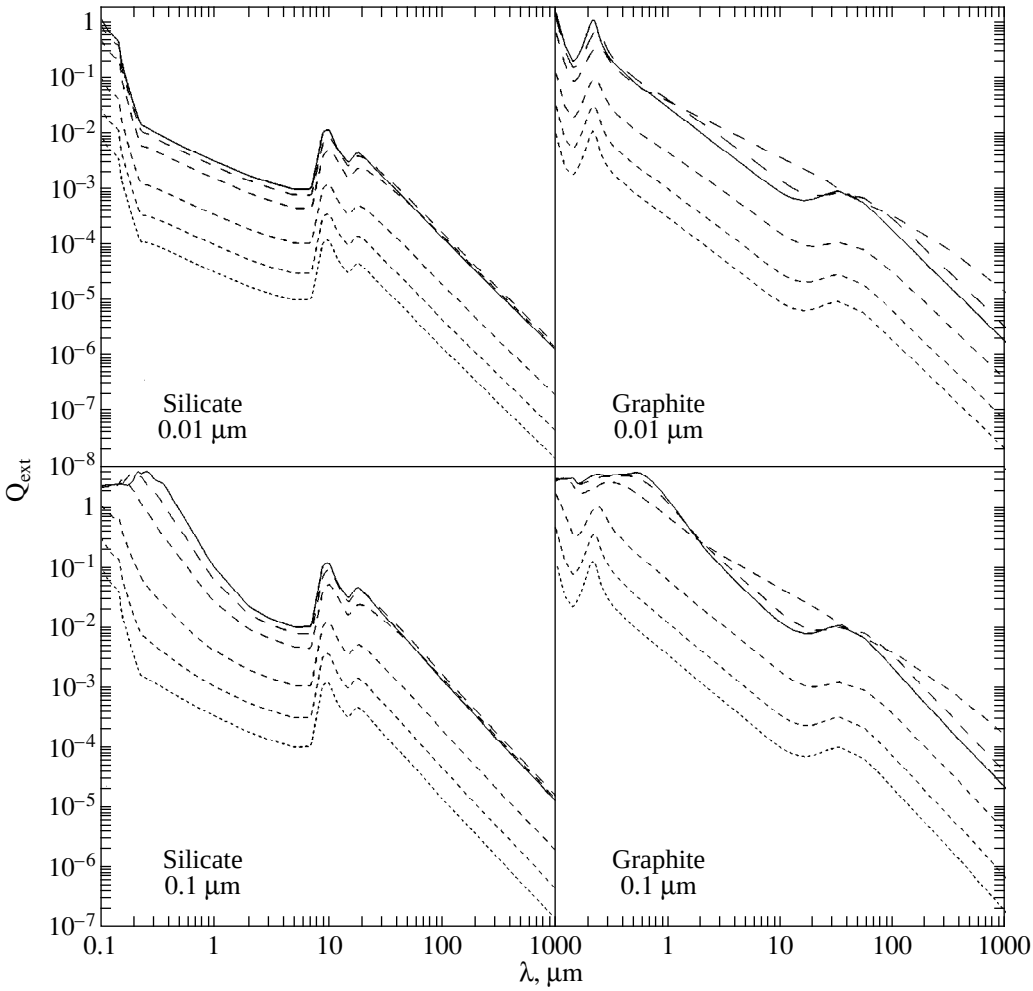

Fig. 8. Extinction efficiencies Q_{ex} for silicate and graphite porous particles of size 0.01 and 0.1 μm.

decreases with increasing p (or decreasing f) for particles of the same size.

An important dynamic indicator is the ratio of radiation-pressure force F_{pr} to gravitational force F_g,

$$\beta = \frac{F_{pr}}{F_g} = \frac{3\sigma}{4\pi c\gamma}\frac{R_*^2 T_*^4}{M_*}\frac{\bar{C}_{pr}}{\rho a^3 f}, \qquad (9)$$

where ρ is the density of the grain material, M_* is the stellar mass, and γ is the gravitational constant. If $\bar{C}_{pr} \sim a^3 f$ (see above), then β does not depend on the grain size and porosity.

We computed Planck mean radiation-pressure cross sections and β for an A0 star ($R_* = 2.5\ R_\odot$; $T_* = 10^4$ K, $M_* = 3.2\ M_\odot$). At large particle porosity and for $a < 0.1$–0.3 μm, β was found to be almost independent of the grain size and roughly correspond to its values for very small, compact grains ($a < 0.001$ μm). For $a > 0.3$–1 μm, β rapidly decreases with increasing a. Recall that, by contrast, there is a noticeable peak of the dependence $\beta(a)$ at $a \sim 0.01$–0.2 μm for compact particles (see, e.g., [48]).

Note also that, for $p \sim 0.9$ and $a < 0.3$ μm, we obtained $\beta \approx 6$–7 and $\beta \sim 70$ for silicate and graphite porous particles, respectively. Although allowance for the star's actual spectral energy distribution must slightly reduce β (see, e.g., [49]), we conclude that even the large porosity of submicron-sized grains composed of astronomical silicate or of more absorptive materials (graphite, amorphous carbon, iron oxide, etc.) cannot prevent their sweeping out of the vicinities of HAeBe stars. Only porous particles of any size composed of less contaminated silicates than astrosil (see, e.g., [50]) can have $\beta < 1$. However, the albedo of such grains is large, and they cannot simultaneously explain the observed IR fluxes and color–magnitude diagrams (at least in terms of the approach used here).

4. CONCLUDING REMARKS

We considered the transfer of polarized radiation in shells with a spheroidal dust distribution at various

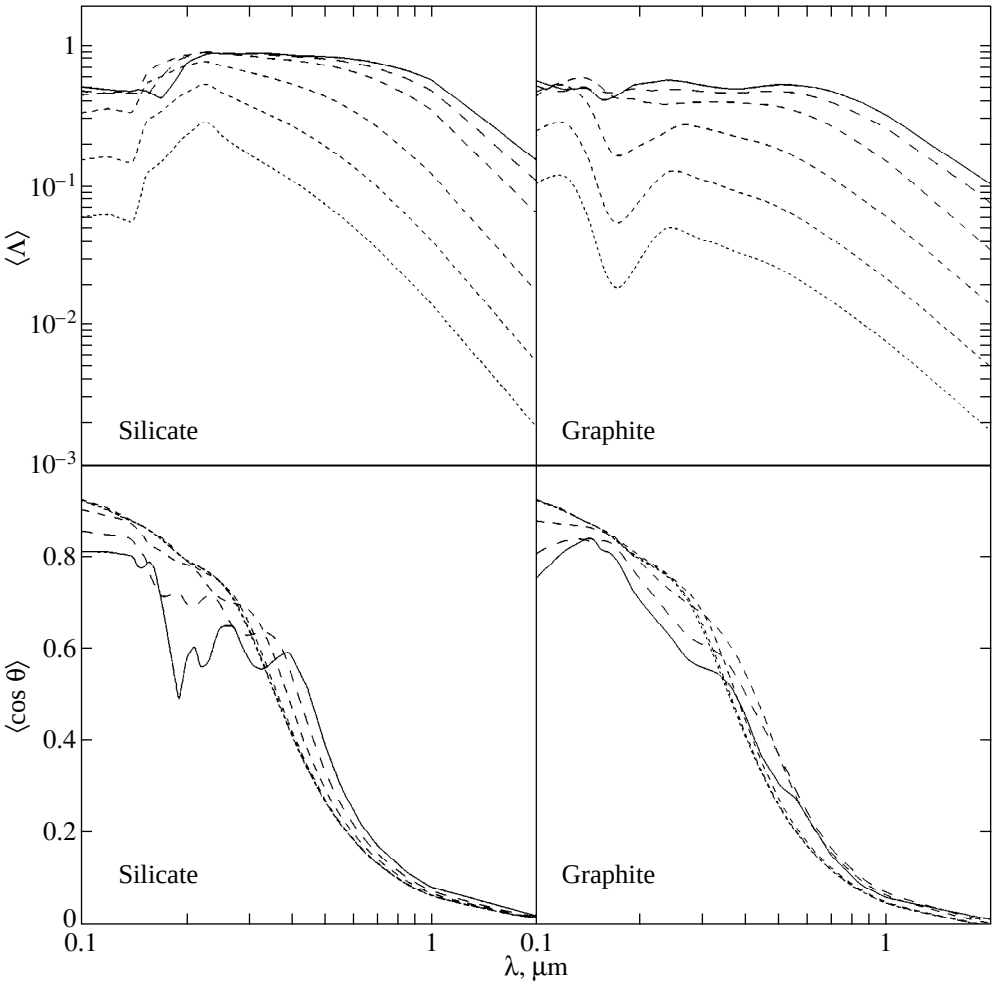

Fig. 9. Albedo and the asymmetry factor of the phase function for silicate and graphite porous particles of size 0.1 μm.

grain porosities. We revealed the effects of noncompactness of circumstellar particles on the observational manifestations of dust shells around HAeBe stars: the spectral energy distribution from the ultraviolet to the infrared, the color–magnitude diagram in the visible range, the wavelength dependence of linear polarization, and the shell brightness distribution in the plane of the sky.

We showed that, in the model we chose, agreement with observational data could be achieved only for grains with a moderate porosity ($p \sim 0.5$). Such a porosity is postulated in some currently available models of interstellar dust (see, e.g., [15]). A considerably larger particle porosity $p \sim 0.9$ is commonly assumed for the grains around β Pic-type stars and of cometary dust [11].

Note that the MRN mixture of particles that we used in our modeling is not quite natural when porous grains are considered. Clearly, the latter must most likely result from subparticle coagulation in the interstellar medium, and, thus, the separate existence of porous silicate and porous graphite particles seems unjustified [15]. We chose the MRN mixture for our analysis, because most similar calculations are performed precisely with this mixture, but the revealed effects must generally show up also for a different representation of an assembly of circumstellar grains. We consider the porosity effects for several models of the particles in the shells of HAeBe stars in the next paper [44].

Here, we determined the optical properties of porous dust grains by using the EMT approximation. The latter suggests that the filling factor f does not vary inside the grain. Meanwhile, a more complex case where f generally decreases outward toward the grain edge is realized in many situations, for example, for fractal particles, including such popular ballistic aggregates as BPCA and BPPA. The optical properties of such aggregates have been repeatedly considered previously (see, e.g., [51, 52]). They differ from homogeneous grains in that the asymmetry factor of the phase function $\langle\cos\Theta\rangle$ for them is larger than that for the particles we considered [43]. As a result, the radiation pressure on such aggregates must be slightly lower, and the dependence of the scattered flux on i must be stronger. In order to assess the importance of these effects,

we plan to also compute radiative transfer in the case where circumstellar grains are ballistic aggregates.

ACKNOWLEDGMENTS

We wish to thank E. Kruegel and O. Fischer, who kindly provided the programs for computing the transfer of unpolarized and polarized radiation. We are also grateful to N.V. Voshchinnikov and H. Kimura for their remarks and helpful discussions. One of us (V.I.) was supported by a scientific grant from the Volkswagen company (Germany), as well as the Federal Program "Astronomy" and the Program "Universities of Russia–Basic Research" (project no. 2154).

APPENDIX

The effect of particle porosity on the observational manifestations of polydisperse assemblies of silicate and graphite circumstellar grains is by no means always clear. For a better understanding of this effect, we provide several figures, which show how porosity changes the optical properties of silicate and graphite particles of different sizes. All calculations were performed by using the EMT approximation and Mie theory.

The input data—the effective refractive indices $\langle m \rangle$ calculated by using the rule (2) for various porosities (p = 0–0.99) of astronomical silicate and graphite—are shown in Figs. 6 and 7, respectively. Note the significant change in the wavelength dependence of the imaginary part of refractive index $\langle m \rangle$ for graphite at $p \sim 0.6$–0.7.

The extinction efficiencies Q_{ext} for silicate and graphite particles of size 0.01 and 0.1 μm are shown in Fig. 8. In the infrared ($\lambda >$ 3–10 μm), Q_{abs} have approximately the same wavelength dependence as Q_{ext}. For graphite particles, we applied the so-called $\left(\frac{1}{3} + \frac{2}{3}\right)$ approximation, which uses the relation $Q_{ext} = \frac{1}{3} Q_{ext}(m_{\|}) + \frac{2}{3} Q_{ext}(m_{\perp})$, where $m_{\perp}$ and $m_{\|}$ are the refractive indices of graphite for two orientations of the electric vector of the incident radiation relative to the axis of the hexagonal structure of crystalline graphite (see [53]). This approximation makes it possible to properly allow for the optical anisotropy of graphite for randomly oriented spherical particles. Notice the different behavior of the curves for silicate and graphite over the entire wavelength range at a moderate particle porosity ($p \le 0.6$).

The albedo and the asymmetry factor of the scattering indicatrix for silicate and graphite porous particles of size 0.1 μm are shown in Fig. 9. The behavior of the curves does not change dramatically with particle size.

REFERENCES

1. N. V. Voshchinnikov and V. P. Grinin, Astrofizika **34**, 181 (1991).
2. P. R. Weissman, in *Protostars and Planets II*, Ed. by D. C. Black and M. S. Mattwesw, (Univ. of Arizona Press, Tucson, 1984), p. 895.
3. C. M. Telesco, E. E. Becklin, R. D. Wolstencroft, and R. Decher, Nature **335**, 51 (1988).
4. W. H. Sorrell, Astrophys. J. **361**, 150 (1990).
5. V. P. Grinin, N. N. Kiselev, N. Kh. Minikulov, *et al.*, Astrophys. Space Sci. **186**, 283 (1991).
6. V. N. Voshchinnikov, F. J. Molster, and P. S. Thé, Astron. Astrophys. **312**, 243 (1996).
7. A. Miroshnichenko, Z. Ivezic, and M. Elitzur, Astrophys. J. Lett. **475**, L41 (1997).
8. S. Pezzuto, F. Strafella, and D. Lorenzetti, Astrophys. J. **485**, 290 (1997).
9. Th. Henning, in *Molecules in Astrophysics: Probes and Processes*, Ed. by E. F. van Dishoeck (Kluwer, 1997), p. 343.
10. E. Pantin, P. O. Lagage, and P. Artymowicz, Astron. Astrophys. **327**, 1123 (1997).
11. A. Li and J. M. Greenberg, Astron. Astrophys. **331**, 291 (1998).
12. N. A. Krivova and V. B. Il'in, Pis'ma Astron. Zh. **23**, 908 (1997) [Astron. Lett. **23**, 791 (1997)].
13. J. S. Mathis, W. Rumpl, and K. H. Nordsieck, Astrophys. J. **217**, 425 (1977).
14. B. T. Draine, ASP Conf. Ser. **58**, 227 (1994).
15. J. S. Mathis, Astrophys. J. **497**, 824 (1998).
16. C. F. Bohren and D. R. Huffman, *Absorption and Scattering of Light by Small Particles* (Wiley, New York, 1983; Mir, Moscow, 1986).
17. A. Laor and B. T. Draine, Astrophys. J. **402**, 441 (1993).
18. R. Stongnienko, Th. Henning, and V. Ossenkopf, Astron. Astrophys. **296**, 797 (1995).
19. M. J. Wolff, G. C. Clayton, and S. J. Gibson, Astrophys. J. **503**, 815 (1998).
20. O. Fischer, Rev. Mod. Astron. **8**, 103 (1995).
21. N. A. Krivova, Candidate's Dissertation (St. Petersburg Univ., St. Petersburg, 1998).
22. R. Chini, E. Krügel, and E. Kreysa, Astron. Astrophys. **167**, 315 (1986).
23. P. S. Thé, D. de Winter, and M. R. Pérez, Astron. Astrophys., Suppl. Ser. **104**, 315 (1994).
24. V. P. Grinin, ASP Conf. Ser. **62**, 63 (1994).
25. V. P. Grinin, Pis'ma Astron. Zh. **14**, 65 (1988).
26. G. V. Zaitseva and V. M. Lyuty, Pis'ma Astron. Zh. **23**, 277 (1997) [Astron. Lett. **23**, 242 (1997)].
27. N. A. Krivova, V. B. Il'in, and O. Fischer, Publ. NASA **3343**, 37 (1996).
28. N. A. Krivova, Pis'ma Astron. Zh. **23**, 371 (1997) [Astron. Lett. **23**, 327 (1997)].
29. C. Friedemann, H.- G. Reimann, J. Gürtler, and V. Tóth, Astron. Astrophys. **277**, 184 (1993).
30. Z. Ivezic and M. Elitzur, Mon. Not. R. Astron. Soc. **287**, 799 (1997).

31. J. I. Hage and J. M. Greenberg, Astrophys. J. **361**, 251 (1990).
32. V. Ossenkopf, Astron. Astrophys. **251**, 210 (1991).
33. Th. Henning and R. Stognienko, Astron. Astrophys. **280**, 609 (1993).
34. J. S. Mathis, Astrophys. J. **472**, 643 (1996).
35. H. R. E. Tjin A Djie, L. Remijn, and P. S. Thé, Astron. Astrophys. **134**, 273 (1984).
36. A. V. Berdyugin, V. P. Grinin, and N. Kh. Minikulov, Izv. Krymsk. Astrofiz. Obs. **86**, 69 (1992).
37. A. Witt, in *Interstellar Dust. IAU Symp. No. 135*, Ed. by L. J. Allamandola and A. G. G. M. Tielens (Reidel, Dordrecht, 1989), p. 87.
38. F. Berrilli, G. Corciulo, G. Ingrosso, *et al.*, Astrophys. J. **398**, 254 (1992).
39. A. Natta, J. Prusti, and E. Krügel, Astron. Astrophys. **275**, 572 (1993).
40. A. S. Mitskevitch, Astron. Astrophys. **298**, 219 (1995).
41. A. S. Mitskevitch, Astron. Astrophys. **298**, 231 (1995).
42. N. V. Voshchinnikov and V. V. Karjukin, Astron. Astrophys. **288**, 883 (1994).
43. H. Kimura and I. Mann, J. Quant. Spectroscop. Radiat. Transf. **60**, 425 (1998).
44. N. A. Krivova and V. B. Il'in, Icarus, 1999 (in press).
45. V. B. Il'in and N. V. Voshchinnikov, Astron. Zh. **70**, 721 (1993).
46. V. B. Il'in and A. V. Krivov, ASP Conf. Ser. **62**, 177 (1994).
47. T. Mukai, H. Ishimoto, T. Kozasa, *et al.*, Astron. Astrophys. **262**, 315 (1992).
48. P. Artymowicz, Astrophys. J. Lett. **335**, L79 (1988).
49. P. L. Lamy and J.-M. Perrin, Astron. Astrophys. **327**, 1147 (1997).
50. C. Jäger, H. Mutschke, B. Begemann, *et al.*, Astron. Astrophys. **292**, 641 (1994).
51. T. Kozasa, J. Blum, and T. Mukai, Astron. Astrophys. **263**, 423 (1992).
52. T. Kozasa, J. Blum, H. Okamoto, and T. Mukai, Astron. Astrophys. **276**, 278 (1993).
53. B. T. Draine, Astrophys. J. **333**, 848 (1988).
54. M. Cohen, Mon. Not. R. Astron. Soc. **161**, 97 (1973).
55. I. S. Glass and M. V. Penston, Mon. Not. R. Astron. Soc. **167**, 237 (1974).
56. E. A. Kolotilov, Astrofizika **13**, 33 (1977).
57. W. B. Weaver and G. Jones, Astrophys. J., Suppl. Ser. **78**, 239 (1992).
58. W. Li, N. J. Evans II, P. M. Harvey, and C. Colomé, Astrophys. J. **433**, 199 (1994).

Translated by V. Astakhov

Astronomy Letters, Vol. 26, No. 6, 2000, pp. 390–397. Translated from Pis'ma v Astronomicheskiĭ Zhurnal, Vol. 26, No. 6, 2000, pp. 456–464.

Spectrum of the Star BM Ori at Minimum Light

E. A. Vitrichenko[1]* and S. I. Plachinda[2]

[1] *Space Research Institute, Russian Academy of Sciences, ul. Profsoyuznaya 84/32, Moscow, 117810 Russia*
[2] *Crimean Astrophysical Observatory, p/o Nauchnyĭ, Crimea, 334413 Ukraine*

Received August 27, 1999

Abstract—Two spectra of the star BM Ori were obtained with the 2.6-m Crimean Astrophysical Observatory telescope near its maximum eclipse phase. The light detector was a CCD array. The wavelength range 5305–5373 Å was chosen in such a way that it contained no strong primary lines. Optimum filtration of the spectra yielded a signal-to-noise ratio of ~300. Eighteen secondary lines are seen in the spectrum. Atmospheric parameters of the secondary star were determined: $T_{\rm eff}$ = 5740 K and log$g$ = 3.0; the secondary was classified by these parameters as being of spectral type G2 III. The best agreement between observed and synthetic spectra is achieved for metallicity [M/H] = –0.5 and microturbulence ξ_t = 0 km s^{-1}. The projected rotational velocity is $V\sin i$ = 60 km s^{-1}, in agreement with the synchronous velocity in the hypothesis that assumes a total eclipse by the secondary star. Atmospheric elemental abundances in the secondary are estimated. Nickel, chromium, and iron exhibit an underabundance of ~1 dex. © *2000 MAIK "Nauka/Interperiodica"*.

Key words: *stars—structure and evolution*

INTRODUCTION

The star BM Ori is a member of the Orion Trapezium. It is a spectroscopic binary and an eclipsing system. The companion Θ^1 Ori B1 with the magnitude $K = 7^m.53(5)$ was discovered at a distance of $0''.9$ [1]. The error, in units of the last digit, is given in parentheses. These measurements were confirmed by Petr *et al.* [2], who obtained $K = 7^m.60(6)$. Both measurements are in good agreement, which argues for the constancy of light from this star. Simon *et al.* [3] found yet another star at a distance of $0''.6$ from the eclipsing system.

Surprising results have recently been obtained by Weigelt *et al.* [4]. These authors discovered that Θ^1 Ori B1 is a binary with the components at distances of $0''.94$ and $1''.02$ from the eclipsing system by using speckle interferometry. They estimated the probability of a chance projection of field stars onto a circle of radius $1''$ to be less than 1%. Given that the primary star is a spectroscopic binary, BM Ori is found to be a pentuple system.

The principal difficulty in understanding the system is that the stellar spectrum during a totality, which lasts for 8.5 h, remains the same as that outside eclipse. In both cases, the spectrum corresponds to a star of spectral type B. Meanwhile, the star reddens appreciably at minimum light, so the eclipsing body is definitely a cooler star. It remains incomprehensible why the secondary spectrum is unseen during a total eclipse. This puzzle was revealed by Doremus [5] and confirmed by Popper and Plavec [6].

Several hypotheses were invoked to account for this phenomenon.

Hall [7] surmised that the eclipse was produced by an opaque disk surrounding the secondary star, which rotates with such a high velocity that it resembles in shape two plates with their bottoms put together. A similar idea was considered by Huang [8] and Zakirov and Shevchenko [9].

Wilson [10] believed the secondary to be a black hole surrounded by a rotating semitransparent disk, which produces an eclipse. Antokhina *et al.* [11] showed that a star could not be eclipsed by a star in the system BM Ori and suggested that the primary was eclipsed by the secondary's extended atmosphere during an eclipse.

Vitrichenko [12] considered a model of the system in which the secondary star is surrounded by a semitransparent dust shell. An eclipse is mainly produced by this shell and partly by the secondary's disk.

Here, we analyze the spectrum of BM Ori near its primary minimum in order to determine the atmospheric parameters and projected rotational velocity of the secondary star, as well as to obtain a preliminary estimate of the chemical composition. We also discuss an eclipse model in which Θ^1 Ori B1 contributes significantly to the light from the system.

* E-mail address for contacts: vitrich@nserv.iki.rssi.ru

1063-7737/00/2606-0390$20.00 © 2000 MAIK "Nauka/Interperiodica"

OBSERVATIONAL DATA AND THEIR REDUCTION

The observations were obtained with the 2.6-m Crimean Astrophysical Observatory telescope. The light detector was a CCD array. We investigated the wavelength range 5305–5373 Å. This range was not chosen accidentally. It contains no strong primary lines, no intense nebular emission lines, and no noticeable telluric lines.

The spectra are listed in Table 1. The first two rows provide data on two spectra of BM Ori. Data on the spectra of the comparison stars are given in the last two rows. The star ζ Leo satisfactorily matches the secondary of the system both in spectral type and in luminosity class. Popper and Plavec [6] used it as a comparison star when searching for secondary lines. However, its projected rotational velocity $V\sin i$ = 85 km s^{-1} [13] is slightly higher than that of the secondary of BM Ori, $V\sin i$ = 60 km s^{-1}. In addition, as our analysis shows (see below), the secondary star is of a considerably later spectral type than has been previously thought. γ Ori is used as a comparison star for the primary, although it is not a close match in spectrum and luminosity. However, it is difficult to find a better comparison star.

The first two columns in Table 1 are self-explanatory. The next columns give dates of observations, Julian dates for mid-exposures (reduced to the Sun), exposure times, corrections to the radial velocity for the Earth's motion, and measured instrumental radial velocities (not reduced to the Sun).

We observed BM Ori near its maximum eclipse phase (at phases 0.973 and 0.975), which corresponds to the second contact. At this time, the primary dims by a factor of ~3, and the secondary lines become a factor of ~2 deeper than those outside eclipse; therefore, they can be measured more accurately.

A preliminary analysis of the spectroscopic data for BM Ori shows that spectral lines are barely seen in each of the spectra because of significant noise. In order to improve the signal-to-noise ratio (S/N), we performed two procedures.

The first procedure is obvious: we added up the two spectra and subtracted twice the background intensity from the sum. Background subtraction in this case is important, because the background accounts for ~10% of the signal. Simultaneously, nebular emission lines were also subtracted. The radial-velocity difference between two exposures due to orbital motion is 2 km s^{-1}, and the projected rotational velocity is $V\sin i$ = 60 km s^{-1}; therefore, adding the spectra causes no line broadening.

The second procedure involves filtration of the spectrum with a rectangular window. The choice of a window width was based on measuring the Gaussian parameter σ for the line profile. Our measurements yielded σ = 1.0(2) Å. We chose a 0.8 Å wide window. The Gaussian parameter for a rectangular window is $\sigma_1 = \sigma/(12)^{1/2}$ = 0.23 Å. This parameter for the filtered spectrum is then $\sigma_2 = (\sigma^2 + \sigma_1^2)^{1/2}$ = 1.03 Å, a value that is larger than σ by a mere 3%. However, the filtration procedure improves considerably the S/N ratio. This ratio measured in a wavelength range without detectable lines (5355–5362) after filtration is S/N = 300.

We performed wavelength calibration of the spectra by using a comparison spectrum; the source of light was an argon-filled lamp with a hollow thorium cathode. The instrumental profile was determined by using lines of this lamp. The Gaussian parameter for it was found to be σ_3 = 0.2 Å, so the true line profile was broadened by the instrumental profile by ~3%, which affects the results only slightly. When radial velocities are determined, the error associated with the difference between the dispersion curves obtained from two comparison spectra located on either side of the observed spectrum is introduced. This error is systematic in nature; its maximum value is ~1 pixel = 0.066 Å = 4 km s^{-1}. However, since we used mean parameters of the dispersion curve, the systematic error could not exceed 2 km s^{-1}.

The spectra of the comparison stars ζ Leo and γ Ori were taken with a better S/N ratio than that of BM Ori, but, for convenience of their comparison, the spectra were also subjected to the same filtration procedure. To obtain a sufficient number of points in the line profile, the filtration was made at steps equal to half the window width.

THE SPECTRUM OF BM Ori AT MINIMUM LIGHT

Figure 1 shows the spectrum of BM Ori (middle) and the spectra of the comparison stars ζ Leo (upper) and γ Ori (lower). The identification of lines belonging to ζ Leo and BM Ori is indicated in the upper part of the figure. Lines belonging to γ Ori are shown in the lower part of the figure. S II 5320.68 Å is a single line, while S II 5345.8 is a blend.

When constructing Fig. 1, we displaced each of the spectra along the wavelength axis by the value corresponding to the radial velocity in Table 1. Thus, the radial velocities of all three stars are zero relative to the wavelength scale. Along the *y* axis, the spectra of the comparison stars were displaced by 0.15 on the continuum intensity scale for convenience of their comparison. We took wavelengths and oscillator strengths from the line list that was kindly sent to us by the Vienna Atomic Line Data (VALD) Center at our request [14].

An examination of Fig. 1 leads us to conclude that only lines of an F–G star are seen in the spectrum of BM Ori near its maximum eclipse phase in the wavelength range under consideration. This conclusion contradicts the opinion of Doremus [5], who believes only the spectrum of the primary B star to be seen at minimum light.

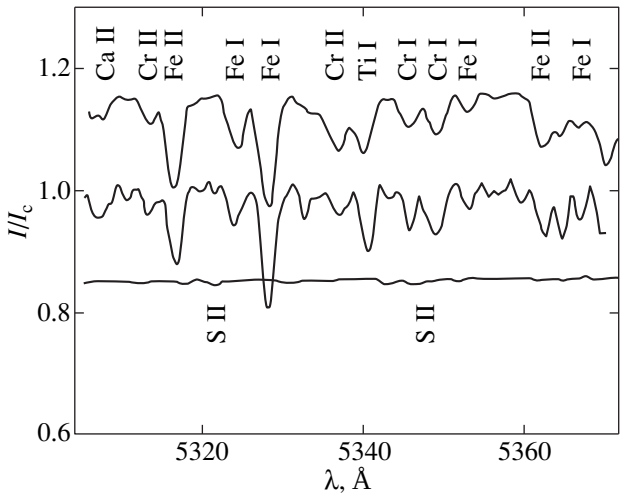

Fig. 1. The spectrum of BM Ori at minimum light (middle curve). The upper and lower curves represent the spectra of ζ Leo and γ Ori, respectively. The species to which the lines of ζ Leo and BM Ori belong are indicated above the upper curve for the strongest lines. The species to which the lines of γ Ori belong is indicated under the lower curve.

There are three main reasons for the contradiction. First, previously, a shorter wavelength part of the spectrum, where the contribution from the secondary star is smaller, was mainly studied [15]. Second, the secondary lines are relatively weak, and their detection in photographic spectra is limited by the noise of the photographic emulsion. The choice of a spectral range without strong primary lines (see the lower spectrum) also played an important role. Third, an overwhelming majority of lines in the spectrum of a G star belong to iron ions; according to our preliminary estimates, iron exhibits an underabundance of ~1 dex (see below), causing the secondary lines to weaken. The detection of secondary lines was discussed in [16].

The primary lines in the BM Ori spectrum are much weaker than those in the γ Ori spectrum for two reasons. They are weakened by the contribution of the secondary star and by the higher projected rotational velocity of the primary star than that of γ Ori. Whereas $V\sin i$ = 170 km s^{-1} for the primary [16], this parameter for γ Ori is 61 km s^{-1} [13].

PROJECTED ROTATIONAL VELOCITY

The subsequent analysis requires that the projected rotational velocity of the secondary star be determined. Previously, it was determined unreliably. Based on eye estimates, Popper and Plavec [6] took $V\sin i$ to lie in the range 50 to 100 km s^{-1}. Vitrichenko *et al.* [16] obtained $V\sin i$ = 55(5) km s^{-1} from the widths of the Na doublet lines. This determination is also unreliable, because these are the resonance lines and can be broadened by pressure.

The projected rotational velocity was estimated from the two strongest Fe II 5316.52 and Fe I 5328.04 lines. Using the average spectrum, but before applying the filtration procedure, we estimated the Gaussian parameters to be 0.92 and 1.12 Å, respectively. For these two lines, we constructed profiles with different rotational velocities by using the STARSP code [17]. We determined the Gaussian parameter for each profile and used these data to construct calibration curves; $V\sin i$ was deduced from the latter. The velocity averaged over the two lines is $V\sin i$ = 60(3) km s^{-1}, in good agreement with previous determinations [16], but the error in our estimate is considerably smaller.

The projected rotational velocity matches the synchronous velocity of the secondary star, $V\sin i$ = 66(2) km s^{-1} [16], within the error limits.

ATMOSPHERIC PARAMETERS OF THE SECONDARY STAR

We determined the effective temperature $T_{\rm eff}$ and the logarithm of surface gravity log$g$ for the secondary star from spectroscopic orbital elements of both components and from light-curve solution [16, 18]. The gravity g can be calculated using the formula

$$g = g_\odot M_2/R_2^2 = 960 \text{ cm s}^{-2},$$

where $g_\odot = 2.7 \times 10^4$ cm s^{-2} is the solar surface gravity, $M_2 = 2.5(1)\,M_\odot$ is the secondary's mass, and $R_2 = 8.4(2)\,R_\odot$ is its radius. We obtained log$g$ = 2.98(2); its error was estimated from the errors of the input data.

We derived the secondary's temperature from the luminosity–radius–temperature relation

$$M_{\rm b} = 42.31 - 5\log R - 10\log T.$$

Here, $M_{\rm b} = +0\overset{m}{.}1$ is the absolute bolometric luminosity of the secondary star. We obtained $T_{\rm eff}$ = 5740(70) K; the error in the temperature was deduced from the error in the radius.

According to the tables from [19], a star with such parameters belongs to the spectral type G2 III. Our

Table 1. Data on the spectra

Star	Spectral type	Date, 1999	JD 2451000+	Exposure time, min	$\Delta V_{\rm r}$, km s^{-1}	$V_{\rm r}$, km s^{-1}
BM Ori	B3+G2	March 1	239.212	30	–25	38(3)
BM Ori	B3+G2	March 1	239.234	30	–25	
ζ Leo	F0 III	March 22	260.441	15	–16	6(3)
γ Ori	B2 III	March 1	239.249	3	–28	54(5)

result is in good agreement with an attempt to classify the secondary star by temperature and luminosity [20]. According to the above study, the star lies in the region of yellow giants in the Hertzsprung–Russell diagram.

BRIGHTNESS OF THE SECONDARY STAR

The next step toward estimating the chemical composition of the secondary star is to determine its brightness during eclipse L_2', which is used to convert observed line equivalent widths W_λ^{obs} to true equivalent widths W_λ using the formula

$$W_\lambda = W_\lambda^{obs}/L_2'. \quad (1)$$

The secondary's brightness is given by

$$L_2 = F_2/(F_1 + F_2 + F_3), \quad (2)$$

where F_1 is the monochromatic flux from the primary, F_2 is the flux from the secondary, and F_3 is the flux from other radiation sources, for example, from the star Θ^1 Ori B1. The term "brightness" was taken from the jargon of variable-star researchers (see [21], p. 97). This quantity is dimensionless. Occasionally, it is called the relative luminosity or luminosity (see [22], p. 176).

The quantity L_2' proves to be difficult to determine, because the eclipse mechanism is not known for certain. Nor do we know the nature of Θ^1 Ori B1. This forces us to consider two hypotheses regarding the pattern of eclipse. In the first hypothesis (A), we consider an eclipse model in which the primary is mainly screened by a semitransparent dust cloud and partly by the secondary disk. In the second hypothesis (B), we make an attempt to allow for the light from Θ^1 Ori B1 by assuming that this star is of spectral type B.

Hypothesis A. We assume Θ^1 Ori B1 to emit no radiation in the spectral range under consideration. This is possible if it is sufficiently cool, for example, of spectral type M. We also assume that the primary star during a totality is partially eclipsed by the secondary and partially by the dust cloud, by the fraction $\alpha_0 = 0.63$ of the entire stellar disk area [12]. According to [23], it follows from an analysis of the depths of minimum that $L_2 = 0.32(2)$ outside eclipse. Vitrichenko and Larionov [15] confirmed this result by an independent method by studying the continuum spectrum. During a totality, we then have

$$L_2' = L_2/[L_1(1-\alpha_0) + L_2] = 0.56(3), \quad (3)$$

where $L_2 = 0.32$ is the secondary's brightness outside eclipse, $L_1 = 0.68$ is the primary's brightness, and $\alpha_0 = 0.63$ is the maximum eclipse phase.

Hypothesis B. Let us consider a different scheme of eclipse by assuming the following: (1) the secondary during eclipse completely screens the primary, and (2) Θ^1 Ori B1 is similar in spectral type to the primary. In that case, we see radiation from the secondary and Θ^1 Ori B1 during eclipse.

An argument for the first assumption is the fact that, according to the atmospheric parameters derived above, the secondary star is a giant. This is confirmed by the location of the secondary in the region of giants in the Hertzsprung–Russell diagram [20].

There are two arguments for the second assumption. First, the stellar spectrum during a totality is the same as that outside eclipse, i.e., typical of a B star [5, 6]. Second, the *UBVRI* light curves can be solved by assuming that the maximum eclipse phase for all these bands is the same, $\alpha_0 = 0.63$. This is possible only if the energy distributions for the primary and the third star are similar. The above assumption was confirmed by Vasileiskiĭ and Vitrichenko [18].

The parameter L_2' for hypothesis B is the same as that for hypothesis A. In this case, the radiation from the primary star, which was considered in hypothesis A, is divided into two parts in the proportion 0.63 : 0.37; the first and second parts are attributed to the primary and the third body, respectively.

As a result, it turns out that it does not matter which of the two hypotheses we take for the reduction of line equivalent widths to allow for the binary nature of the star. In any case, $L_2' = 0.56(3)$ during a totality.

ESTIMATING THE CHEMICAL COMPOSITION

We can give many reasons why chemical anomalies may be suspected in the secondary star. The first one is its youth. The atmosphere could retain the "fossil" chemical composition if the secondary was formed from the matter preserved in the parent globule. The second reason is the binary nature. The primary could "transfer" part of its matter processed in the first nuclear reactions to the secondary. The third reason is that the secondary could "collect" matter from a gaseous nebula with a light-element underabundance [24]. The explosion of a nearby supernova and magnetic fields can also change the atmospheric chemical composition.

The secondary lines identified in BM Ori are listed in Table 2. About half of the lines are blends; most lines belong to Fe I. The Ca II line is most likely interstellar in origin. The first and second columns give the species and the wavelength λ_1 of the strongest line in the blend, respectively. The wavelength λ_2 (without the first three digits), which is a weighted mean of the wavelengths of the lines in the blend, is given next. The VALD line depths served as weights. This wavelength was used to measure the radial velocity (next column). The next two columns contain the measured equivalent width W_1 of the entire blend and the equivalent width W_2 of the strongest line freed from the effects of weaker lines. Weak lines were taken into account by using the VALD line depths. The next-to-last column gives the radial

Table 2. A list of secondary lines in BM Ori

Species	λ_1, Å	λ_2, Å	W_1, Å	W_2, Å	V_r, km s^{-1}	Blends
Ca II	5307.22	7.32	0.049	0.036	32:	Fe I 7.36
Cr II	5310.69		0.010		44	
Cr II	5313.36		0.031		29	
Fe II	5316.62	6.70	0.068	0.036	38	Fe II 6.78
Fe I	5322.04		0.008		25	
Fe I	5324.18	4.84	0.039		44	Fe II 5.55
Fe I	5328.04	8.30	0.118	0.046	43	Cr I 8.38, Fe I 8.53
Fe I	5332.90	2.83	0.024	0.017	44	Fe I 2.66, Si I 3.24
Cr II	5334.87		0.009		4:	
Ti II	5336.77		0.026		63:	
Fe II	5337.73	7.75	0.030	0.016	3:	Cr II 7.77, Si I 7.99
Fe I	5341.02	1.03	0.070	0.031	16	Mn I 1.06
Cr I	5345.80		0.031		52	
Cr I	5348.31	8.96	0.081	0.040	41	Ca I 9.46, Fe I 9.73
Fe I	5353.37		0.022		43	
Fe II	5362.87		0.056		39	
Fe I	5364.86	5.08	0.036	0.021	52	Fe I 5.40
Fe I	5367.48		0.032		37	

velocity determined from the blend using λ_2, and the blends (the wavelength is given without the first three digits) are listed in the last column.

The procedure of allowance for weak lines is not faultless. It makes sense only under the following conditions: solar chemical composition, microturbulence $\xi_t = 2$ km s^{-1}, and metallicity [M/H] = 0. All these quantities were specified for the VALD line list. As we show below, none of these conditions is satisfied. For this reason, allowance for weak lines is merely an approximation rather than an exact solution to the problem of line blending.

When in doubt about line identification or when lines were closely spaced, we put a colon near the radial velocity.

When the chemical composition is calculated, it is necessary to determine the microturbulence ξ_t. Model calculations show that the line equivalent widths decrease by a factor of 2.5, on the average, as ξ_t changes from 0 to 12 km s^{-1}. The speed of sound is an upper limit.

We used the following standard technique to estimate ξ_t: the microturbulence was chosen in such a way that the coefficient b in the equation

$$\varepsilon(\mathrm{Fe/H}) = a + bW_\lambda \qquad (4)$$

was zero. Here, ε is the abundance of an element (in our case, neutral iron) relative to hydrogen, and W_λ is the line equivalent width.

Unexpectedly, b turned out to be close to zero at $\xi_t = 0$. As ξ_t grows, b also sharply grows, and the rms error of one equation (4) increases. For main-sequence G stars, $\xi_t = 2$ km s^{-1}, on the average [25]. For a G giant, the microturbulence can only be larger, in conflict with the above estimate.

The number of measured Fe I lines in the spectrum is relatively small, which casts doubt on the accuracy of constructing a dependence of the type (4). However, we have two spectra of BM Ori obtained with the CCD spectrograph of the 6-m telescope outside eclipse [26]. In these spectra, we managed to detect and measure ~100 Fe I lines. An analysis of these measurements shows that $b \sim 0$ at $\xi_t = 10$ km s^{-1}. The behavior of the dependences of b on ξ_t for these spectra proved to be opposite: b decreases with increasing ξ_t, as does its error. The value of b is positive in the former case and negative in the latter case for all ξ_t.

This contradiction remains incomprehensible. The difference in the microturbulences can be assumed to be real, and this is attributable to variability of the physical conditions in the stellar atmosphere. The star exhibits flares for about 10% of the time [27], which may cause the turbulent velocity to increase, and no flares are observed for about 90% of the time. Some stabilization mechanism, for example, a magnetic field, may be operating.

The results of our abundance calculations are presented in Table 3. We used the line equivalent widths corrected for blending and reduced by using formula (1). The first column gives species; solar elemental abundances, deviations [X/H] of the abundance from the solar value, errors σ of the mean abundance, and number N of lines used follow next. The last three columns (marked with asterisks) contain the same quantities obtained from a preliminary analysis of the spectra out-

side eclipse [26]. Both abundance measurements are in satisfactory agreement, within the error limits, although we used markedly different microturbulences. This is an additional argument that the microturbulence is variable. The solar elemental abundances were taken from the VALD database. Using more accurate data [28] affects the result only slightly.

Since the abundances of most of the elements were not known, we chose [M/H] during our analysis in such a way that the observed and synthetic spectra coincided most closely. It turned out that agreement could be achieved at [M/H] = –0.5 dex. A similar result for other stars in the Orion Nebula was obtained by Cunha *et al.* [29]. These authors showed iron in the F and G stars of the Orion association to be underabundant, [Fe/H] = –0.16. On the other hand, Vitrichenko and Klochkova [30] investigated the chemical composition of the star V1016 Ori and found iron to be probably overabundant, [Fe/H] = 0.07(4).

In Fig. 2, the observed spectrum of BM Ori is compared with its synthetic spectrum computed with $T_{\rm eff}$ = 5740 K, log$g$ = 3.0, [M/H] = –0.5, and ξ_t = 0 km s^{-1}. To allow for the light from the secondary star, we reduced its observed spectrum by using the formula

$$I_r = 1 - (1 - I_{obs})/L_2', \quad (5)$$

where I_r is the reduced spectrum, and I_{obs} is the observed spectrum. The wavelengths of the observed spectrum were shifted in accordance with the instrumental radial velocity (see Table 1).

An examination of Fig. 2 shows that the observed spectrum is in satisfactory agreement with the synthetic one. The largest discrepancy is seen for the Fe I 5332.90+Fe I 5332.66+Si I 5333.34 blend and the Cr II 5334.87 line. This discrepancy is difficult to explain, but the superposition of emission lines originating in the secondary's atmosphere can be a possible reason. In addition, the first line is a complex blend, and the effect of its components on the observed equivalent width is difficult to estimate. The Cr II line exhibits an abnormal radial velocity (see Table 2), so there may be an error in the identification. In both cases, the blend most likely contain the line of an element that is more underabundant than iron or chromium.

DISCUSSION

Let us discuss the following questions: (1) How well do our measured radial velocities of the three stars studied agree with published determinations? and (2) How can Θ^1 Ori B1 affect the observed spectrum and the light curve.

It follows from Table 1 that the secondary's radial velocity is V_r = 38–25 = 13(1) km s^{-1}. According to refined spectroscopic orbital elements for the secondary star [16], the radial velocity for phase 0.974 must be V_r^1 = –14(2) km s^{-1}. Hence, O–C = +27 km s^{-1}. The difference cannot be explained by observational errors. This brings up a number of questions: How accurate are the period and the epoch? How accurate are the elements of the secondary's radial-velocity curve? Is there any systematic error in the radial velocity?

Table 3. Preliminary estimates of the chemical composition for the secondary star of BM Ori

Species	Sun	[X/H]	σ	N	[X/H]*	σ*	N*
Ti II	–7.05	–1.2		1	–0.9	0.1	33
Cr I	–6.37	–0.8	0.2	2	0.0	0.1	41
Cr II	–6.37	–0.5	0.3	3	–0.4	0.1	17
Fe I	–4.37	–1.6	0.1	8	–1.3	0.1	82
Fe II	–4.37	–0.7	0.4	3	–1.8	0.1	11

We took the photometric elements (period and epoch) from [23]. The error in the epoch is $0^d.001$. The radial-velocity difference requires that the error in the phase be +0.027, which corresponds to an error of $0^d.14$ in the date. The accumulated error in the period can give an error of $0^d.007$. So, errors in the photometric elements cannot account for the difference. It was pointed out in the literature that BM Ori could have a secular change of the orbit [23, 31]. However, as yet there are no quantitative estimates of this effect.

Errors in the spectroscopic orbit cannot give an error in the calculated radial velocity larger than 2 km s^{-1}.

Let us check whether there is a systematic error in the radial velocities by using the comparison stars. For ζ Leo and γ Ori, our measured heliocentric radial velocities are –10(3) and +26(5) km s^{-1}, respectively (see Table 1). In the catalog of stellar radial velocities [32], V_r = –15 and +18 km s^{-1} for the first and second stars, respectively. The difference can be explained by obser-

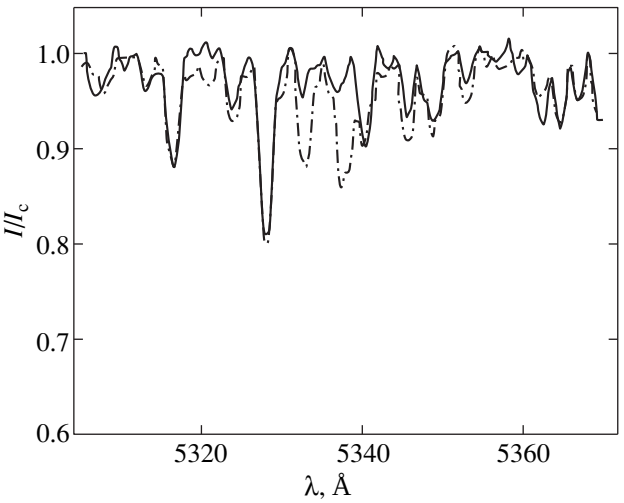

Fig. 2. Comparison of the synthetic (dashed line) and observed (solid line) spectra for the secondary of BM Ori.

vational errors and by the fact that both stars exhibit radial-velocity variations over a narrow range. We thus conclude that our radial-velocity determinations cannot have the systematic error that accounts for the radial-velocity difference.

Popper and Plavec [6] found that the secondary's radial velocity inferred from several spectra was systematically higher by 20 km s^{-1}, while the radial velocities of interstellar lines are in agreement with an accuracy of 1 km s^{-1}. The secondary's radial velocity can therefore be assumed to occasionally increase by ~20 km s^{-1}. In that case, the deviation of the secondary's radial velocity by +27 km s^{-1} we detected can also be explained.

Let us check whether Θ^1 Ori B1 can actually be the source of third light. As was already mentioned above, we only know the K magnitude of this star, $K = 7\overset{m}{.}6$. Let us calculate its magnitude K_1 by using data from [15]. Good agreement between the magnitudes K and K_1 is achieved if we assume that half of the flux from dust belongs to the binary system and the second half belongs to Θ^1 Ori B1:

$$K_1 = K_+ - 2.5\{\log[L_1(1-\alpha_0) + L_d/2]\} = 7\overset{m}{.}6, \quad (6)$$

where $K_+ = 6\overset{m}{.}3$ is the total magnitude of the stars calculated by using data from [2], $L_1 = 0.19$ is the brightness of the primary star, $\alpha_0 = 0.63$ is the maximum eclipse phase or (in hypothesis B) the ratio of the flux from the primary to the total flux from the "primary + third star," and $L_d = 0.46$ is the ratio of the flux from dust to the total flux from the triple system.

The hypothesis is confirmed under the above assumptions, but it should be noted that the dust shell gives 3/4 of the entire flux. On the one hand, this comes as no surprise, because the dust radiation in this band is more intense than the radiation from each of the stars [15]. On the other hand, the magnitude K_1 depends largely on what fraction of the dust radiation we attribute to the third star. In this case, it is therefore pertinent to speak about the lack of disagreement between K and K_1 rather than about their equality.

The question of dust localization still remains to be solved. According to hypothesis B, half of the dust radiation comes from the binary system and the other half from the third star. Where is the dust located in the binary system? Around the secondary star or around the entire system? Infrared observations of the minimum shows that the dust in the binary system lies around the secondary [33], but this result needs to be confirmed.

The problem of detecting and measuring secondary lines has a long history [16]. Our analysis explains why these lines are difficult to detect. The secondary lines are weakened for the following reasons: (1) the previously studied photographic flux from the primary exceeds the flux from the secondary; (2) there is a metal underabundance; (3) the projected rotational velocity is relatively high; and (4) the photographic spectra have a S/N ratio of ~ 30, and the secondary lines fall within the noise track. For the above reasons, the secondary lines are virtually unseen in the spectrum, although the primary and secondary stars are comparable in brightness.

We have been able to solve the problem stated above because: the depth of secondary lines in the spectra during eclipse increased by a factor of 1.8; the signal-to-noise ratio reached 300 through the use of a CCD array; and we chose a portion of the spectrum in the V band where the flux from the secondary is higher than its photographic flux.

CONCLUSION

We detected eighteen secondary lines in the spectra of BM Ori obtained near a totality. Having analyzed the radial-velocity curve and the light curve, we determined atmospheric parameters for the secondary star: $T_{\rm eff} = 5740$ K and $\log g = 3.0$. These parameters correspond to the spectral type G2 III, in good agreement with the secondary's position in the Hertzsprung–Russell diagram [20].

The microturbulence was found from Fe I lines to be $\xi_t = 0$ km s^{-1}. This microturbulence is not typical of a yellow giant, which can be attributed to the peculiar atmospheric structure.

We determined the projected rotational velocity, $V\sin i = 60(3)$ km s^{-1}, in agreement with the estimates of other authors. In hypothesis B, this velocity agrees with the synchronous velocity $V_e = 66(2)$ km s^{-1} from [16].

Our radial velocity of the secondary star disagrees with the radial-velocity curve, which can be explained by the fact that the radial velocity is variable—it occasionally increases by ~20 km s^{-1}. This phenomenon may be associated with mass outflow from the atmosphere.

We considered two hypotheses for the pattern of eclipse. In the first hypothesis, an eclipse is assumed to be produced by a dust shell around the secondary star. In the second hypothesis, the secondary completely screens the primary, while Θ^1 Ori B1 is a third light. The fraction of the flux from the secondary during a totality proves to be the same for both hypotheses, $L_2' = 0.56(3)$.

A preliminary abundance analysis shows that one might expect a metal underabundance [M/H] ~ –0.5 dex in the secondary star. The observed spectrum is in satisfactory agreement with the synthetic one computed with the above atmospheric parameters.

ACKNOWLEDGMENTS

We wish to thank the Vienna Atomic Line Data (VALD) Center for sending us a line list at our request and V.V. Tsymbal for providing the STARSP code, which we widely used here. This study was supported

by the International Science Foundation (grant nos. R2Q000 and U1C000) and the ESO C&EE Program (grant no. A-05-067).

REFERENCES

1. M. J. McCaughrean and J. R. Stauffer, Astron. J. **108**, 1382 (1994).
2. M. G. Petr, V. C. Foresto, S. V. W. Beckwith, *et al.*, Astrophys. J. **500**, 825 (1998).
3. M. Simon, L. M. Cloes, and T. L. Beck, Astron. J. **117**, 1375 (1999).
4. G. Weigelt, Y. Balega, T. Preibisch, *et al.*, Preprint Max Planck Inst., No. 799 (1999).
5. C. Doremus, Publ. Astron. Soc. Pacif. **82**, 745 (1970).
6. D. M. Popper and M. Plavec, Astrophys. J. **205**, 462 (1976).
7. D. S. Hall, Bamberg Veroff. **9**, 217 (1971).
8. S.- S. Huang, Astrophys. J. **195**, 127 (1975).
9. M. M. Zakirov and V. S. Shevchenko, Perem. Zvezdy **21**, 638 (1982).
10. R. E. Wilson, Astrophys. Space Sci. **19**, 165 (1972).
11. E. A. Antokhina, N. Z. Ismailov, and A. M. Cherepashchuk, Pis'ma Astron. Zh. **15**, 837 (1989) [Sov. Astron. Lett. **15**, 362 (1989)].
12. E. A. Vitrichenko, Pis'ma Astron. Zh. **24**, 708 (1998) [Astron. Lett. **24**, 611 (1998)].
13. A. A. Boyarchuk and I. M. Kopylov, Izv. Krymsk. Astrofiz. Obs. **31**, 44 (1964).
14. F. Kupka, N. E. Piskunov, T. A. Ryabchikova, *et al.*, Astron. Astrophys. **138**, 1 (1999).
15. E. A. Vitrichenko and V. M. Larionov, Pis'ma Astron. Zh. **22**, 178 (1996) [Astron. Lett. **22**, 157 (1996)].
16. E. A. Vitrichenko, V. S. Shevchenko, and V. A. Shcherbakov, Pis'ma Astron. Zh. **22**, 185 (1996) [Astron. Lett. **22**, 163 (1996)].
17. V. V. Tsymbal, ASP Conf. Ser. **108**, 198 (1995).
18. A. S. Vasileiskiĭ and E. A. Vitrichenko, Pis'ma Astron. Zh. (2000) (in press).
19. V. Straizis and G. Kuriliene, Astrophys. Space Sci. **89**, 353 (1981).
20. E. A. Vitrichenko, Pis'ma Astron. Zh. **22**, 587 (1996) [Astron. Lett. **22**, 523 (1996)].
21. A. A. Mikhailov, *A Course in Astrophysics and Stellar Astronomy* (Fizmatgiz, Moscow, 1962), Vol. 2.
22. D. Ya. Martynov, *A Course in General Astrophysics* (Nauka, Moscow, 1988).
23. N. I. Bondar' and E. A. Vitrichenko, Pis'ma Astron. Zh. **21**, 700 (1995) [Astron. Lett. **21**, 627 (1995)].
24. K. Cunha, Rev. Mex. Astron. Astrofis. **27**, 111 (1993).
25. D. Gray, *The Observation and Analysis of Stellar Photospheres* (Wiley, New York, 1976).
26. E. A. Vitrichenko and V. G. Klochkova, Pis'ma Astron. Zh. (2001) (in press).
27. N. I. Bondar' and E. A. Vitrichenko, Astron. Zh. **74**, 701 (1997).
28. N. Grevesse, A. Noels, and A. J. Sauval, ASP Conf. Ser. **99**, 117 (1996).
29. K. Cunha, V. V. Smith, and D. L. Lambert, Astrophys. J. **493**, 195 (1998).
30. E. A. Vitrichenko and V. G. Klochkova, Pis'ma Astron. Zh. **26**, 13 (2000) (in press).
31. D. S. Hall and L. M. Garrison, Publ. Astron. Soc. Pacif. **81**, 771 (1969).
32. R. E. Wilson, *General Catalogue of Stellar Radial Velocities* (Washington Publ., Carnegie Inst., 1953).
33. E. A. Vitrichenko, Preprint Inst. Kosmich. Issled. Ross. Akad. Nauk, No. 1982 (1998).

Translated by V. Astakhov

Astronomy Letters, Vol. 26, No. 6, 2000, pp. 398–403. Translated from Pis'ma v Astronomicheskiĭ Zhurnal, Vol. 26, No. 6, 2000, pp. 465–471.

Optical Spectrum of the Infrared Source IRAS 20004+2955 (V1027 Cyg)

V. G. Klochkova[1], T. V. Mishenina[2]*, and V. E. Panchuk[1]

[1] *Special Astrophysical Observatory, Russian Academy of Sciences, Nizhniĭ Arkhyz, Stavropol'skiĭ kraĭ, 357147 Russia*
[2] *Astronomical Observatory, Odessa State University, Odessa, Ukraine*

Received May 15, 1999; in final form, September 27, 1999

Abstract—Based on high-dispersion echelle spectra taken with the 6-m Special Astrophysical Observatory telescope, we study the IR source IRAS 20004+2955 identified with the variable star V1027 Cyg. We have determined the star's fundamental parameters ($T_{\rm eff}$ = 5000 K, log$g$ = 1.0), metallicity ([Fe/H] = –0.2 dex), and atmospheric abundances of 16 elements. Its metallicity, carbon underabundance, and slight overabundance of the heavy elements Zr, Y, Ce, and Eu suggest that V1027 Cyg belongs to the Galactic disk population. © *2000 MAIK "Nauka/Interperiodica".*

Key words: *stars—structure and evolution*

INTRODUCTION

The theory of final evolutionary stages for red giants and supergiants receives observational confirmation slowly and with difficulty. Visible photometry proved to be ineffective, because the lines of normal colors could not be constructed (strong absorption in circumstellar shells is a hindrance). The situation improved significantly as a result of the IRAS mission, when it became possible to associate IR characteristics of the shells with the presumed evolutionary status of the corresponding objects and to construct evolutionary models for gas–dust shells [1]. A subsequent, more oriented search for evolutionary changes of the chemical composition in the stellar atmospheres of objects at the protoplanetary-nebula stage shows that the chemical composition of a sample of protoplanetary-nebula candidates is highly nonuniform, and its peculiarities are associated with a set of characteristics of both IR and optical spectra [2, 3].

There are many examples when different classification criteria yield contflicting results. The object IRAS 20004+2955, identified with the variable star V1027 Cyg (HD 333385, BD+29 3865), serves as an example. Its very red color index (B–V) = 2.34 is apparently attributable to substantial interstellar reddening of this object, located close to the Galactic plane. The IR color indices are similar to those of IRAS 18095+2704, which is believed to be a typical protoplanetary nebula, but its chemical abundance [4] is not in close agreement with that expected for this evolutionary stage.

On the other hand, modeling a low-resolution spectrum of IRAS 20004+2955 led Volk and Kwok [1] to conclude that the object was just beginning to evolve toward high temperatures. In the diagram that relates the intensity of the 10-μm emission feature to the infrared color index [25/12], IRAS 20004+2955 is located in the region occupied by intermediate-mass giants with effective temperatures above 5000 K, which corresponds to the core-helium burning stage between the first and the second ascent along the red giant branch [5]. The mean width of 14 photospheric lines was found from photographic spectra with 0.4 Å resolution to be 34 km s^{-1} [6], which corresponds to luminosity class 0.

Arkhipova *et al.* [7] classified V1027 Cyg as SRd with the photometric amplitude increasing from V to U. They concluded that most of the reddening was attributable to interstellar extinction; the pattern of light and color variations suggests that the variability was caused by pulsations. In the spectrum taken in October 1991 with a two-pixel resolution of about ~4 Å, Arkhipova *et al.* [7] suspected the presence of weak molecular C_2 Swan bands, 4714 (2;1) and 4734 Å (1;0), and the September 25, 1996 spectrum [8] exhibited molecular TiO bands (γ, γ', and β); Ba II lines were suspected to be enhanced (relative to Hα), and radial-velocity variations were detected, which confirm the pulsation model of light variations.

The above features of IRAS 20004+2955 make its in-depth abundance analysis of current interest; it can help understand the object's evolutionary status.

OBSERVATIONS AND ANALYSIS OF SPECTRA

Our spectrograms of V1027 Cyg were obtained with the PFES [9] and NES [10] echelle spectrographs of the

* E-mail address for contacts: tamar@deneb.odessa.ua

Table 1. Characteristics of the spectra and radial velocities

Spectrogram	JD 2400000+	λλ, Å	Resolution	Signal/noise	Radial velocities	
					V_r, km s^{-1}	σ
s15103	50309.4	4020–8000	13000	>100	8.88	3.30
s15104	50309.4	4020–8000	13000	>100	8.83	2.75
s20525	51001.4	5000–5900	35000	100	10.29	0.89
s20633	51002.4	5000–5900	35000	100	10.02	0.91

6-m Special Astrophysical Observatory telescope. Information about the spectrograms is presented in Table 1. The spectrograms were reduced by using the MIDAS [11] and DECH20 [12] packages.

DETERMINING THE MODEL PARAMETERS AND CHEMICAL COMPOSITION

The spectral type of the object under study was considered by several authors and was estimated to range from G7 Ia to K2–4 I. The spread in estimates can be explained primarily by the star's variability. Roman [13], Keenan and McNeil [14], and Winfrey *et al.* [15] found the spectral type to be K0 Ia, G7 Ia, and K2–4 I, respectively. The spectra obtained at different epochs with the same spectrograph were classified as late G [7] and K2 Ib [8].

Using spectra with 1.5 Å resolution, Hrivnak *et al.* [16] estimated the spectral type to be G7 Iab. When modeling the IR spectrum, these authors ran into the difficulty of describing optical and near-IR fluxes using a single value of the extinction. According to Hrivnak *et al.* [16], this may imply that the star's effective temperature is below 5000 K assumed in the model.

Using a calibration relationship between the equivalent width of the oxygen infrared triplet and the absolute luminosity [17], we estimated $M_V \approx -7$. Based on equivalent widths of the barium 5853, 6141 Å lines, we estimated M_V by extrapolating the calibration from [18] to be in the range –7 to –8. Taking into account uncertainty in the object's mass and large errors of the above calibrations in the luminosity range under consideration, we gave up determining the surface gravity from the luminosity.

Because of the ambiguous relationship between light and color variations [8] and because of the large reddening, we also gave up determining the effective temperature from photometric data. We estimated the effective temperature ($T_{\rm eff}$ = 5000 K) by comparing observed and theoretical Hα profiles. In this case, the profile is described best at the surface gravity log$g$ = 1, but it should be borne in mind that the Hα profile is only slightly sensitive to log$g$ in this temperature range. The assumed $T_{\rm eff}$ is confirmed by the lack of correlation between the Fe I abundance and the lower-level potential of the Fe I lines used for its determination. The conditions of ionization equilibrium for iron and vanadium (two Fe II lines and one V II line were measured in the spectrum) give a lower value, log$g$ = 0.7. The set of $T_{\rm eff}$ and log$g$ corresponds to the spectral type G5 Ib. We determined the microturbulent velocity (6.7 km s^{-1}) from the condition that there was no correlation between the equivalent widths W of Fe I lines and the number density of iron atoms calculated from the corresponding lines.

We estimated the uncertainty in the effective temperature, gravity, and microturbulent velocity to be 100 K, 0.3 dex, and 0.3 km s^{-1}, respectively.

We determined the chemical composition by using the spectra taken with the 6-m telescope on August 14, 1996 (JD 2450309). Photometric measurements are available for this date: V = 8.88, B–V = 2.28, and U–B = 2.26 [8]. The star was on the descending branch of its light curve, where the absorption spectra of semiregular variables are generally not distorted by emission. Since our spectra exhibit no clear peculiarities, we could use the intensity ratio of the Ba II 6497 Å and Hα lines for the classification ($I_{6497}/I_{6563} < 1$, typical of normal supergiants). We estimated the spectral type to be G5 Ia–G7 Iab. The figure shows the corresponding portion of the spectrum. The only peculiarity of the spectrum is the line broadening, which exceeds significantly the instrumental-profile widths of the spectrographs used. By comparing the observed and theoretical spectra, we estimated the broadening (35 km s^{-1}), in agreement with the value from [6]. Although microturbulence is most likely responsible for the broadening, we formally estimated the projected rotational velocity from the Fe I 4476 Å line to be $V\sin i$ = 40 km s^{-1}. For

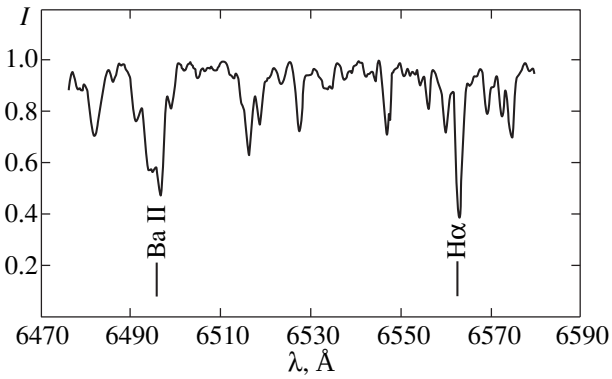

A portion of the V1027 Cyg spectrum near the Ba II and Hα lines (JD 2450309)

Table 2. Atomic data for the lines used, their equivalent widths, and the elemental abundances derived from specific lines using two model atmospheres: (1) $T_{\rm eff}$ = 5000 K, log$g$ = 1.0, (2) $T_{\rm eff}$ = 4900 K, log$g$ = 0.5; log$A$(H) = 12

Species	λ, Å	χ, eV	loggf	W, mÅ	log$A$(X)	
					(1)	(2)
1	2	3	4	5	6	7
Li I	6707.800	0.00	0.02	15.00	1.12	1.01
Na I	6154.220	2.10	–1.50	230.30	6.94	6.89
Al I	6696.020	3.14	–1.56	61.80	6.23	6.19
	6698.670	3.14	–1.86	54.40	6.46	6.42
Si I	5645.600	4.92	–2.13	97.20	7.50	7.46
	5665.550	4.92	–2.07	119.90	7.57	7.52
	5772.150	5.08	–1.72	161.20	7.62	7.56
	5793.070	4.92	–1.98	145.60	7.63	7.57
	7034.901	5.87	–0.88	131.10	7.42	7.39
	5690.430	4.93	–1.86	169.50	7.64	7.58
	6125.030	5.61	–1.46	97.30	7.55	7.51
	6131.860	5.61	–1.70	86.10	7.72	7.68
	6583.710	5.95	–1.57	55.10	7.68	7.65
	6800.600	5.96	–1.75	40.40	7.70	7.67
Ti I	5673.400	3.11	–0.40	8.20	4.93	4.88
	5766.330	3.29	0.35	29.80	4.97	4.91
	6312.240	1.46	–1.56	49.20	5.02	4.92
	6325.150	0.02	–3.38	42.40	5.07	4.91
	5644.137	2.26	0.13	155.50	4.98	4.89
	5866.450	1.07	–0.87	256.60	5.03	4.91
	5937.810	1.07	–1.95	87.50	5.29	5.17
	6126.220	1.07	–1.42	148.90	5.07	4.95
	5604.910	1.04	–1.17	46.30	4.15	4.04
	5670.830	1.08	–0.36	156.10	4.08	3.96
	5703.570	1.05	–0.23	137.80	3.83	3.71
V I	6058.110	1.04	–1.36	11.90	3.68	3.57
	6081.430	1.05	–0.60	100.60	3.97	3.85
	6224.505	0.28	–1.79	112.20	4.31	4.15
	6274.700	0.26	–1.64	67.50	3.85	3.70
	5830.675	3.11	0.72	10.00	3.88	3.83
V II	5819.935	2.52	–1.82	93.30	4.15	4.01
Cr I	5787.970	3.32	–0.06	144.80	5.50	5.44
	6330.090	0.94	–2.80	118.80	5.33	5.20
	6882.475	3.43	–0.28	54.90	5.20	5.15
	6883.060	3.43	–0.35	68.50	5.39	5.33
	6926.037	3.44	–0.55	106.90	5.86	5.80
	6669.270	4.18	–0.42	14.50	5.54	5.50
Mn I	5537.760	2.18	–1.90	161.90	5.43	5.33
	5516.774	2.17	–1.79	200.00	5.49	5.39
Fe I	5386.330	4.15	–1.82	141.60	7.74	7.68
	5441.330	4.31	–1.60	78.30	7.31	7.25
	5560.190	4.43	–1.15	99.00	7.13	7.08
	5633.960	4.99	–0.37	193.50	7.48	7.43
	5650.710	5.08	–0.79	67.60	7.25	7.21
	5651.450	4.47	–1.87	32.30	7.29	7.24

Table 2. (Contd.)

1	2	3	4	5	6	7
Fe I	5652.310	4.26	–1.83	38.70	7.10	7.05
	5653.800	4.38	–1.49	67.00	7.18	7.13
	5661.348	4.28	–1.89	108.70	7.75	7.69
	5809.200	3.88	–1.73	149.10	7.36	7.28
	5859.560	4.54	–0.63	228.20	7.41	7.34
	5905.670	4.65	–0.81	169.20	7.40	7.34
	6055.970	4.73	–0.47	170.10	7.14	7.09
	6082.710	2.22	–3.62	215.00	7.62	7.50
	6093.666	4.60	–1.44	82.30	7.47	7.42
	6094.340	4.65	–1.64	23.20	7.08	7.03
	6096.662	3.98	–1.85	84.00	7.20	7.13
	6226.730	3.88	–2.16	128.40	7.65	7.58
	6351.270	4.31	–2.63	12.80	7.41	7.35
	6380.750	4.18	–1.39	147.00	7.31	7.24
	6726.640	4.61	–1.10	154.30	7.51	7.45
	6732.060	4.58	–2.21	35.20	7.73	7.68
	6737.980	4.56	–1.76	63.90	7.57	7.51
	6752.720	4.63	–1.31	91.40	7.40	7.34
	6769.660	4.58	–2.36	28.90	7.79	7.74
	6786.856	4.19	–1.99	80.40	7.50	7.44
	6801.870	1.61	–5.84	16.40	7.62	7.49
	6806.850	2.73	–3.22	130.90	7.36	7.26
	6820.430	4.64	–1.22	118.80	7.47	7.42
	6837.016	4.59	–1.80	63.50	7.63	7.58
	6851.640	1.61	–5.39	22.00	7.30	7.17
	6911.520	2.42	–3.98	58.80	7.30	7.20
	6916.700	4.15	–1.41	148.10	7.26	7.19
	7366.387	4.63	–1.95	51.00	7.69	7.63
	7430.541	2.58	–3.90	55.00	7.35	7.25
	7473.552	4.60	–1.86	45.00	7.49	7.44
	7476.376	4.79	–1.61	39.00	7.38	7.33
	7491.649	4.30	–1.06	172.00	7.17	7.10
	7498.530	4.14	–2.24	29.00	7.14	7.08
	7501.272	4.18	–2.98	6.00	7.21	7.16
	7551.100	5.09	–1.47	17.10	7.17	7.13
	7563.020	4.83	–1.53	65.10	7.60	7.55
	7568.894	4.28	–0.88	213.00	7.15	7.08
	7582.150	4.95	–1.55	34.80	7.43	7.39
	7588.300	5.03	–0.98	64.30	7.26	7.21
	7723.200	2.28	–3.50	162.90	7.20	7.09
Fe II	5824.410	3.42	–4.77	20.60	7.26	7.09
	7479.693	3.89	–3.59	135.00	7.62	7.45
Co I	5342.700	4.02	0.62	114.50	4.85	4.78
	6189.000	1.71	–2.19	80.60	4.75	4.62
	6093.143	1.74	–2.27	95.70	4.97	4.84
	6771.040	1.88	–1.80	140.20	4.85	4.72
	6814.950	1.95	–1.79	87.30	4.63	4.50
	7054.040	2.72	–1.52	50.80	4.95	4.85

Table 2. (Contd.)

1	2	3	4	5	6	7
Ni I	5847.000	1.67	–3.35	103.00	5.88	5.75
	6186.710	4.10	–0.84	122.50	6.23	6.16
	6327.600	1.67	–2.98	178.10	5.84	5.71
	6772.313	3.65	–0.93	168.60	6.01	5.93
	6086.276	4.26	–0.84	96.80	6.26	6.20
	5094.420	3.83	–1.07	59.90	5.79	5.73
	5468.100	3.85	–1.57	62.60	6.31	6.25
	5643.100	4.16	–1.19	25.20	5.82	5.76
	5996.740	4.24	–0.97	24.40	5.65	5.60
	6204.640	4.09	–1.09	61.60	6.05	5.99
	6635.150	4.42	–0.68	57.50	5.95	5.89
	6772.360	3.66	–0.86	183.20	6.01	5.93
	6850.480	3.68	–1.92	44.00	6.21	6.14
	7030.060	3.54	–1.70	80.00	6.14	6.06
Y I	6435.050	0.07	–0.93	20.40	2.30	2.16
	6687.500	0.00	–0.65	42.80	2.27	2.12
Y II	5728.890	1.84	–1.16	122.00	2.49	2.29
Zr I	6762.380	0.00	–1.18	39.40	2.66	2.49
Ce II	5117.170	1.39	–0.04	51.50	1.45	1.24
	6043.390	1.21	–0.20	79.50	1.59	1.37
Eu II	6049.510	1.28	–0.42	70.20	0.79	0.58
	6645.130	1.38	0.29	208.80	0.94	0.72

Table 3. Atmospheric elemental abundances for V1027 Cyg determined from two model atmospheres: (1) $T_{\rm eff}$ = 5000 K, log$g$ = 1.0, (2) $T_{\rm eff}$ = 4900 K, log$g$ = 0.5; n is the number of lines used for the analysis

Species	n	(1)		(2)		Sun
		log$A$	σ	log$A$	σ	log$A$
Li I	1	1.12		1.02		1.06
Na I	1	6.94		6.89		6.32
Al I	2	6.35	0.12	6.31	0.12	6.43
Si I	10	7.60	0.09	7.56	0.09	7.64
Ca I	3	6.27	0.14	6.21	0.14	6.38
Ti I	8	5.05	0.10	4.95	0.09	5.06
V I	8	3.97	0.19	3.85	0.18	4.00
V II	1	4.15		4.01		4.00
Cr I	6	5.47	0.20	5.41	0.21	5.64
Mn I	2	5.46	0.03	5.36	0.03	5.56
Fe I	46	7.39	0.19	7.33	0.19	7.64
Fe II	2	7.44	0.18	7.28	0.18	7.56
Co I	6	4.83	0.12	4.72	0.11	4.83
Ni I	14	6.01	0.19	5.94	0.20	6.22
Zr I	1	2.66		2.49		2.36
Y I	2	2.28	0.02	2.14	0.02	2.24
Y II	1	2.49		2.29		2.24
Ce II	2	1.52	0.07	1.31	0.07	1.47
Eu II	2	0.87	0.07	0.66	0.07	0.60

this purpose, we used the $V\sin i$ calibration for F supergiants from [19]. Our measured radial velocities are given in Table 1 (σ is the rms error of measurement from a single line).

As was shown above, the luminosity estimates do not argue for the value of log$g$ obtained from the condition of ionization equilibrium. However, the spectrum of V1027 Cyg is mainly represented by lines of neutral atoms, and the errors in the chemical composition attributable to uncertainty in log$g$ affect the abundances of those rare earths which are represented only by lines of ions. In our procedure of determining the chemical composition, we restrict ourselves to lines whose effective formation depths correspond to atmospheric levels described well in the plane-parallel approximation.

The abundances of all elements were determined from lines with $W < 200$ mÅ. We used Kurucz's grid of model atmospheres [20] by applying a standard procedure of interpolation between grid points. To determine the elemental abundances, we used Kurucz's WIDTH-9 code and the STARSP software package developed by Tsymbal [21]. In some cases, we computed synthetic spectra to identify lines in blends by means of the STARSP code. This software package was also used to analyze the molecular spectrum. Oscillator strengths loggf were taken from [22]. Table 2 gives atomic data for the lines used, their equivalent widths, and the abundances derived from two model atmospheres.

DISCUSSION

The derived elemental abundances are given in Table 3 for two model atmospheres with the following parameters: $T_{\rm eff}$ = 5000 K, log$g$ = 1 [model (1)] and $T_{\rm eff}$ = 4900 K, log$g$ = 0.5 [model (2)]. For both models, the correlation coefficient between log$A$(Fe) and the lower-level excitation potential of Fe I lines does not exceed 0.1; i.e., within the error limits of the method, the two models are identical in $T_{\rm eff}$. As we see from Table 3, using the models with the above parameters has no fundamental effect on the results of our abundance determinations. The lithium abundance is nearly solar and apparently suggests lithium depletion in the atmosphere due to deep mixing of the envelope. For the CNO-group elements, we estimated only an upper limit for the carbon abundance, log$A$(C) < 8.3. This estimate was obtained from the intensity of the molecular C_2 (0, 1) Swan band head. The method of determining the light-element abundances from molecular-band heads is outlined in [23]. The carbon lines near 7100 Å are strongly blended with the telluric spectrum, the oxygen 6300 Å line is also blended, and the IR oxygen triplet lines are very strong and unsuitable for determining the oxygen abundance. The nitrogen lines are weak and blended; the nitrogen abundance is difficult to derive from CN spectral features, because neither the oxygen nor the carbon abundance is known. We deduced the sodium abundance from the 6154 Å line with W = 230 mÅ. Since this line is weakly susceptible to departures from LTE (the errors in the abundances in the LTE approximation do not exceed 0.2 dex), we can also speak about a sodium overabundance. As we see from Table 3, a modest underabundance of the iron-group elements, ~ –0.2 dex, was obtained for the object under study. Relative to Fe, we found modest overabundances of Zr, Y, Ce, and Eu, whose values decrease with increasing luminosity.

We conclude that the derived chemical abundance pattern generally corresponds to the atmosphere of a normal supergiant. However, if we take into account our estimate of the carbon abundance relative to Fe, then this will be a relationship that is more characteristic of asymptotic-giant-branch (AGB) stars. The semiregular light variations and the high degree of intrinsic polarization do not rule out the possibility that V1027 Cyg is at the post-AGB stage.

CONCLUSION

Based on spectra obtained over a wide wavelength range, we determined the fundamental parameters and detailed chemical composition of the peculiar supergiant V1027 Cyg with the IR excess produced by its circumstellar gas–dust shell. The abundances of the iron-group elements were shown to differ only slightly from their solar values: the star's metallicity is [Fe/H] = –0.2 dex. The nearly solar metallicity in combination with the radial velocity that we measured for two different epochs of observations and with the star's location near the Galactic plane, lead us to conclude that the object belongs to the Galactic disk. The carbon underabundance and the sodium overabundance are consistent with the hypothesis that the star is at the post-AGB stage.

ACKNOWLEDGMENTS

This study was supported by the Russian Foundation for Basic Research (project no. 99-02-18339).

REFERENCES

1. K. M. Volk and S. Kwok, Astrophys. J. **342**, 345 (1989).
2. V. G. Klochkova, Bull. Spec. Astrophys. Obs. **44**, 5 (1998).
3. V. G. Klochkova, R. Szczerba, V. E. Panchuk, and K. M. Volk, Astron. Astrophys. **345**, 905 (1999).
4. V. G. Klochkova, Mon. Not. R. Astron. Soc. **272**, 710 (1995).
5. P. David and R. Papoular, Astron. Astrophys. **237**, 425 (1990).
6. C. L. Imhoff, Astrophys. J. **214**, 773 (1977).
7. V. P. Arkhipova, N. P. Ikonnikova, V. P. Noskova, and S. Yu. Shugarov, Pis'ma Astron. Zh. **18**, 436 (1992) [Sov. Astron. Lett. **18**, 175 (1992)].
8. V. P. Arkhipova, V. F. Esipov, N. P. Ikonnikova, *et al.*, Pis'ma Astron. Zh. **23**, 794 (1997) [Astron. Lett. **23**, 690 (1997)].
9. V. E. Panchuk, I. D. Najdenov, V. G. Klochkova, *et al.*, Bull. Spec. Astrophys. Obs. **44**, 127 (1998).
10. V. E. Panchuk, V. G. Klochkova, and I. D. Naidenov, Preprint Spec. Astrophys. Obs., No. 135 (1999).
11. Image Processing Group, Eur. South. Obs., MIDAS Users Guide, Release 95 Nov. (1995).
12. G. A. Galazutdinov, Preprint Spec. Astrophys. Obs., No. 92 (1992).
13. N. G. Roman, in *Spectral Classification and Multicolor Photometry*, Ed. by Ch. Ferenbach and B. Westerlund (Reidel, Dordrecht, 1973), p. 36.
14. P. C. Keenan and R. McNeil, *An Atlas of Spectra of the Cooler Stars* (Ohio State Univ., Columbus, 1976).
15. S. Winfrey, C. Barnbaum, M. Morris, and A. Omont, Bull. Amer. Astron. Soc. **26**, 1382 (1994).
16. B. J. Hrivnak, S. Kwok, and K. M. Volk, Astrophys. J. **346**, 265 (1989).
17. A. A. Ferro and E. E. Mendoza, V, Astron. J. **106**, 2516 (1993).
18. S. Andrievsky, Astron. Nachr. **319**, 239 (1998).
19. A. Slettebak, G. W. Collins, II, P. B. Boyce, *et al.*, Astrophys. J., Suppl. Ser., **29**, 137 (1975).
20. R. L. Kurucz, Rev. Mexic. Astron. Astrofis. **23**, 181 (1992).
21. V. V. Tsymbal, Odessa Astron. Publ. **7**, Part 2, 146 (1994).
22. E. A. Gurtovenko and R. I. Kostyk, *Fraunhofer Spectrum and the Set of Solar Oscillator Strengths* (Naukova Dumka, Kiev, 1989).
23. T. V. Mishenina and V. V. Tsymbal, Pis'ma Astron. Zh. **23**, 693 (1997) [Astron. Lett. **23**, 609 (1997)].

Translated by N. Samus'

Astronomy Letters, Vol. 26, No. 6, 2000, pp. 404–412. Translated from Pis'ma v Astronomicheskiĭ Zhurnal, Vol. 26, No. 6, 2000, pp. 472–480.

Infrared Photometry for Variable Stars of Selected Types in 1978–1999

O. G. Taranova*

Sternberg Astronomical Institute, Universitetskiĭ pr. 13, Moscow, 119899 Russia

Received April 14, 1999; in final form, August 12, 1999

Abstract—We present and discuss IR observations for 35 stars of different variability types averaged over many years. These include about twenty symbiotic stars, four W Ser stars and one Algol, six Miras, etc. *© 2000 MAIK "Nauka/Interperiodica".*

Key words: *stars—variable and peculiar; IR photometry; circumstellar dust shells*

INTRODUCTION

In the mid-1970s, systematic studies of variable stars of different types were started with IR photometry of Miras, Be stars, and other bright near-IR sources at the Crimean Station of the Sternberg Astronomical Institute (SAI). At present, the list of program objects contains about one hundred sources. Here, we present the results of our statistical analysis of *JHKLM* photometric data for several tens of these objects.** The list contains 16 symbiotic stars, four W Ser stars, six Miras, etc.

OBSERVATIONS

IR photometry for stars of different variability types was performed with the 1.25-m telescope at the Crimean Station of the SAI from 1978 until 1998. Prior to 1985, *JHK* and *LM* photometry had been carried out using a photometer with plumbum sulfide (PbS) detectors cooled by solid carbon oxide (*JHK* photometry) and by liquid nitrogen (*LM* photometry). Since 1985, *JHKLM* photometry for astrophysical sources has been performed using a photometer with a photovoltaic indium antimonide (InSb) detector cooled by liquid nitrogen [1]. The InSb detector is considerably more sensitive than the PbS detector and is currently an optimum choice for near-IR (1–5 μm) observations. The photometer was mounted at the Cassegrain focus of the telescope, the exit aperture was ~12″, and the spatial separation of the modulated beams was ~30″ in the east–west direction. The list of program stars is given in Table 1. The second, third, and fourth columns contain variability types, ranges of *V* magnitudes, and variability periods, respectively; the next column lists the star's coordinates and the photometric standards used. The data in columns 2–6 were taken from the GCVS [2]. The last column contains references to published IR observations of individual stars at the Crimean Station of the SAI. Standard stars were chosen from the catalog [3]; their *HLM* magnitudes were estimated from their spectral types by using relations from [4]. In our stellar photometry, the error of a single photometric measurement generally did not exceed a few hundredths of a magnitude.

DISCUSSION

The mean *J* magnitudes and *J–K*, *H–K*, *K–L*, and *K–M* color indices calculated from the entire set of our observations for each of the 35 sources (Table 1) are collected in Table 2. Besides, Table 2 contains mean epochs of observations, standard deviations (SD), and the number of observing nights for each star (*N*). All stars were arbitrarily subdivided into several groups: (a) sixteen symbiotic stars; (b) four W Ser stars and one Algol; (c) six Miras; (d) four "unique" objects; and (e) four "others."

While analyzing the data from Table 2, we noticed the following characteristic features. Among the symbiotic stars, the largest amplitude of *J* light variations was observed for the slow novae V1016 Cyg and HM Sge ($\Delta J \sim 0\overset{m}{.}8$) and for the carbon symbiotic star UV Aur ($\Delta J \sim 0\overset{m}{.}4$). CH Cyg, V1329 Cyg, WY Gem, TX CVn, V1413 Aql, BF Cyg, and AG Dra with ΔJ in the range $0\overset{m}{.}28$–$0\overset{m}{.}13$ follow next. Minimum ΔJ were observed for the carbon symbiotic star NQ Gem and for V443 Her. The largest *J–K* and *H–K* color variations, which in most cases reflect atmospheric-temperature variations in the cool components of symbiotic stars,

* E-mail address for contacts: taranova@sai.msu.ru

** Electronic tables with *JHKLM* photometry for these stars will be made available via INTERNET at http://infra.sai.msu.ru in 2000.

Table 1. A sample from our list of objects observed at the Crimean Station of the SAI in 1978–1999

Object	Type	ΔV	P, day	α_{2000}	δ_{2000}	BS	Reference
S Per	M	8–12	822	$2^h\ 19^m$	58° 22′	834	–
RX Cas	SER	7–9	32	3 03	63 23	1035	[10–13]
ε Aur	GS	3–4	9892	4 58	43 45	1454	–
ζ Aur	GS	3–4	972	4 59	41 00	1454	–
UV Aur	SS	7–11	394	5 19	32 28	1791	[14–16]
U Ori	M	5–13	368.3	5 53	20 10	2134	–
WY Gem	SS	9–10	–	6 09	23 13	2134	[17]
ZZ CMi	SS	10–12	5000	7 19	09 05	2854	[17]
NQ Gem	SS	7–8	70	7 29	24 37	2905	–
R LMi	M	6–13	372.19	9 43	34 45	3705	–
RW LMi	SRA	13–16	640	10 13	31 57	4100	[15, 16]
R UMa	M	6–14	301.62	10 41	69 02	4301	–
TX UMa	GS	7–9	3.06	10 42	45 50	4335	[13, 18]
TX CVn	SS	9–12	–	12 42	37 02	4915	[14, 19, 20]
AG Dra	SS	9–12	554	16 01	66 56	6132	[21, 14]
V CrB	M	7–13	357.63	15 48	39 43	5932	–
RU Her	M	7–14	484.83	16 08	25 12	5947	–
FG Ser	SS		–	18 15	–0 18	6752	[14, 22]
V443 Her	SS	11–12	–	18 20	23 25	6895	[21, 14, 23]
V1413 Aql	SS		–	19 03	16 28	7176	[14, 24]
BF Cyg	SS	9–13	–	19 22	29 35	7417	[21, 14]
CH Cyg	SS	6–9	–	19 23	50 08	7328	[20, 25–31, 7]
HM Sge	SS	11–18	550	19 40	16 38	7488	[32–38]
CI Cyg	SS	10–13	855	19 46	35 33	7615	[39]
V1016 Cyg	SS	10–17	580	19 55	39 42	7796	[32, 34, 40, 41]
FG Sge	–	9–14	–	20 09	20 11	7635	[6, 42, 8, 5]
P Cyg	SDOR	3–6	–	20 16	37 53	7796	–
V627 Cas	–		–	22 57	58 49	8832	[43, 44]
V367 Cyg	SER	7–8	18	20 46	39 06	7949	[45]
V1329 Cyg	SS	12–18	950	20 49	35 24	7949	[46]
V360 Lac	SER	5.9–6	10	22 48	41 41	8632	–
V407 Cyg	M + NB	13–?	745	21 00	45 34	8079	[24]
VV Cep	GS	4.8–5.4	7430	21 55	63 23	8334	–
KX And	SER	6.9–7.05	–	23 05	49 55	8860	[45]
Z And	SS	8–12.4	–	23 31	48 32	8860	[47]

were found for V1016 Cyg and HM Sge [$\Delta(J–K) \sim 0\overset{m}{.}4$]; less pronounced variations were detected in UV Aur, CH Cyg, TX CVn, AG Dra, FG Ser, CI Cyg, and BF Cyg. For the remaining symbiotic stars, the $J–K$ and $H–K$ color variations are within the limits of photometric errors. Note that $J–K$ color variations within $0\overset{m}{.}4$ correspond to color-temperature variations up to 500–700 K at color temperatures below 3500 K.

Among the W Ser stars, the eclipsing binaries RX Cas and V367 Cyg and the Algol TX UMa exhibit the largest amplitude of J light variations, and these variations are obviously due to orbital motion. The largest $J–K$ and $H–K$ color variations were observed in the W Ser star V367 Cyg; in the remaining W Ser stars, these variations were within the limits of photometric errors.

Among the Miras under study, the largest amplitude of J light variations was observed for S Per ($\Delta J \sim 0\overset{m}{.}7$), a slightly smaller amplitude was observed for V CrB and RU Her ($\Delta J \sim 0\overset{m}{.}4$), and $\Delta J \sim 0\overset{m}{.}2$ for the three remaining Miras. S Per also shows the largest (among the Miras in Table 1) $J–K$ and $H–K$ color variations; in the other Miras, these variations do not exceed $0\overset{m}{.}15$.

Among the "unique" objects, the largest J light variations ($\Delta J \sim 1\overset{m}{.}1$) were observed in FG Sge. These variations occurred in 1992–1998 after the star's outburst [5]. Prior to 1992, the J light variations in FG Sge did not exceed several tenths of a magnitude [6–8]. This star also showed the largest color variations over the last seven years. The carbon star RW LMi and V407 Cyg can be considered to be next in instability among the "unique" stars. The (possibly symbiotic) star AS 501A can be classed with objects of medium IR variability.

Among the "other" objects, the existence of IR variability is not obvious, because their IR light variations do not exceed $0\overset{m}{.}04$–$0\overset{m}{.}06$.

The existence of dust shells around the program stars can be judged from their K–L and K–M color indices. For normal cool stars, they do not exceed $0\overset{m}{.}40$ and 0^m, respectively; larger values suggest the presence of relatively hot dust shells. Thus, the data in Table 2 show that most program stars have color excesses; fourteen stars exhibit no excesses. Maximum excesses were observed in the "unique" object RW LMi, and slightly smaller excesses were observed in the symbiotic star HM Sge and the "unique" object FG Sge after its outburst; the symbiotic star V1016 Cyg, the unique object V627 Cas, and the symbiotic star CH Cyg and V407 Cyg with nearly the same excesses follow next in order of decreasing excesses. Considerable color excesses were observed in the symbiotic stars UV Aur, TX CVn, and BF Cyg.

Characteristic features of the color indices for the program stars discussed above are clearly seen in the two-color diagrams of Fig. 1. Figure 1a shows that, by their mean J–K and H–K color indices, a considerable fraction of the objects (including the W Ser stars, several symbiotic stars, and all the "other" stars) are located along the lines of their variations for normal stars. Another group of stars is located along the blackbody line. The pattern in Fig.1b is slightly different. Only late-type stars and "hot" stars (the W Ser star V360 Lac and the Algol TX UMa) remain near the line of normal stars. Most stars in the two-color [(J–K), (K–L)] diagram (Fig. 1b) lie above the lines for normal stars and a blackbody. The positions of the stars in the two-color diagrams confirm our conclusions about color excesses in the program stars.

Since the existence of dust shells around most program stars was established simultaneously with the beginning of their IR observations, we will assume the observed brightness and color excesses to be mainly attributable to radiation from the circumstellar dust shells. In this case, the observed flux from the star, $F_{\rm obs}(\lambda)$, can be represented as the sum

$$F_{\rm obs}(\lambda) = F_{\rm star}(\lambda) + F_{\rm dust}(\lambda), \quad (1)$$

where the first term is the flux from the star (or from the stars if the system is multiple and the other components contribute appreciably at a given wavelength) at the outer boundary of the dust shell, and the second term is the flux from the dust shell. The contribution of real dust shells (the dust-grain temperatures in which cannot exceed 1500–1700 K) to the spectral range $\lambda < 1.5$ μm is generally no larger than a few percent of the flux from the system's stellar components. Consequently, only the radiation from the central star attenuated by the dust shell is seen in this range. This effect is clearly seen in Fig. 1a, where the mean J–K and H–K color indices for the program stars lie along the blackbody line, whose slope, in turn, is close to that of the normal interstellar reddening line. In other words, attenuation of the radiation from the central sources by dust shells with different optical depths mainly shows up in the behavior of the J–K and H–K color indices. However, as follows from Fig. 1b, the radiation from the dust shell itself is significant even for K–L: most values lie above the lines for normal stars and a blackbody. To illustrate this conclusion, we calculated several models for the radiation from a star + dust shell system. The calculations were performed for a spherically symmetric, physically thin (a constant source function $B(\lambda) = \varepsilon/\alpha$) dust shell, whose radiation was in equilibrium with the radiation from the central star. In this case, relation (1) can be approximately represented as

$$\begin{aligned} F_{\rm obs}(\lambda) &\approx \Theta_{\rm star}^2 B(\lambda, T_{\rm star}) e^{-\tau(\lambda)} \\ &+ \Theta_{\rm dust}^2 B(\lambda, T_{\rm dust})(1 - e^{-\tau(\lambda)}) \\ &= \Theta_{\rm star}^2 B(\lambda, T_{\rm star}) e^{-\tau(\lambda)} \\ &\times [1 + (R_{\rm dust}^2/R_{\rm star}^2)(B(\lambda, T_{\rm dust})/B(\lambda, T_{\rm star}))(e^{\tau(\lambda)} - 1)], \end{aligned} \quad (2)$$

where $\Theta_{\rm star}$ and $\Theta_{\rm dust}$ are the angular radii of the star and the dust shell; $R_{\rm star}$ and $R_{\rm dust}$ are the radii of the star and the shell; $T_{\rm star}$ and $T_{\rm dust}$ are the temperatures of the star and the shell; $\tau(\lambda)$ is the optical depth of the dust shell at a given wavelength; and $B(\lambda, T)$ is the monochromatic fluxes from a blackbody at temperature T. According to McCabe [9],

$$\begin{aligned} &(R_{\rm dust}/R_{\rm star})^2 \\ &\approx 0.25[\langle Q(T_{\rm star})\rangle/\langle Q(T_{\rm dust})\rangle](T_{\rm star}/T_{\rm dust})^4, \end{aligned} \quad (3)$$

where $\langle Q(T_{\rm star})\rangle$ and $\langle Q(T_{\rm dust})\rangle$ are the grain absorption efficiency factors averaged over the spectrum of the star and the dust shell.

Since $\langle Q(T_{\rm star})\rangle/\langle Q(T_{\rm dust})\rangle \propto \langle \tau_{\rm star}(\lambda)\rangle/\langle \tau_{\rm dust}(\lambda)\rangle$ and assuming a power-law wavelength dependence of the optical depth, i.e., $\tau(\lambda) \propto \lambda^{-\beta}$ and $\langle \tau_{\rm star}(\lambda)\rangle/\langle \tau_{\rm dust}(\lambda)\rangle \approx [(\lambda_{\rm star}^{\rm max}/\lambda_{\rm dust}^{\rm max}]^{-\beta} = (T_{\rm dust}/T_{\rm star})^{-\beta}$, relation (3) can be rewritten as

$$(R_{\rm dust}/R_{\rm star})^2 \approx 0.25(T_{\rm star}/T_{\rm dust})^{4+\beta}. \quad (4)$$

Table 2. Statistics of our *JHKLM* photometry for variable stars in 1978–1999

(a) Symbiotic stars

Z And				CH Cyg			WY Gem		
Parameter	Mean	SD	*N*	Mean	SD	*N*	Mean	SD	*N*
JD 2400000+	44880	2320	10	48576	2252	209	51032	217	18
J	6.34	0.14	7	1.09	0.29	195	3.07	0.02	18
H–K	0.23	0.06	7	0.55	0.08	186	0.35	0.03	18
J–K	1.28	0.06	7	1.66	0.15	185	1.26	0.02	18
K–L	0.44	0.20	4	0.90	0.16	170	0.24	0.04	18
L–M	–0.23	0.00	1	0.10	0.11	157	–0.36	0.04	18
UV Aur				CI Cyg			V443 Her		
JD 2400000+	49162	2078	66	47154	2895	56	48313	2544	32
J	4.32	0.41	66	5.85	0.08	50	6.67	0.05	30
H–K	0.88	0.13	65	0.33	0.07	32	0.34	0.07	14
J–K	1.99	0.23	65	1.29	0.09	46	1.27	0.05	28
K–L	0.88	0.29	65	0.28	0.13	21	0.26	0.08	13
L–M	0.21	0.17	61	–0.30	0.13	14	–0.25		1
AG Dra				V 1016 Cyg			HM Sge		
JD 2400000+	45801	1748	29	47335	2561	134	46906	2545	110
J	7.15	0.13	24	7.17	0.74	109	7.41	0.81	95
H–K	0.17	0.13	15	1.16	0.24	98	1.50	0.25	77
J–K	0.93	0.09	19	2.44	0.39	105	3.13	0.40	86
K–L	1.13	2.15	7	1.76	0.36	83	2.08	0.46	58
L–M	–0.17	0.00	1	0.63	0.46	78	0.65	0.42	58
ZZ CMi				V 1329 Cyg			FG Ser		
JD 2400000+	49574	2169	15	44869	374	9	45054	884	11
J	4.14	0.10	15	8.22444	0.28	9	5.89	0.06	8
H–K	0.37	0.10	13	0.555	0.04	2	0.45	0.10	7
J–K	1.25	0.04	15	1.43333	0.17	6	1.49	0.08	8
K–L	0.24	0.05	15				0.26	0.04	4
L–M	–0.16	0.11	15				–0.30	0.00	2
TX CVn				NQ Gem			V1413 Aql		
JD 2400000+	46833	5013	94	51053	203	16	48333	1833	19
J	7.35	0.18	80	4.44	0.05	16	8.89	0.15	18
H–K	0.37	0.09	40	0.36	0.02	16	0.47	0.05	9
J–K	1.23	0.14	72	1.24	0.04	16	1.25	0.08	18
K–L	0.75	0.11	37	0.33	0.03	16	0.43	0.08	8
L–M	0.09	0.24	21	–0.41	0.05	16			

BF Cyg			
JD 2400000+	48002	2198	86
J	7.57	0.13	80
H–K	0.34	0.07	26
J–K	1.30	0.09	69
K–L	0.39	0.15	29
L–M	0.01	0.26	8

(b) W Ser stars

KX And				V 367 Cyg			TX UMa		
Parameter	Mean	SD	*N*	Mean	SD	*N*	Mean	SD	*N*
JD 2400000+	50527	1272	26	50266	1274	56	45784	1821	25
J	5.81	0.09	26	5.42	0.23	56	6.82	0.23	25
H–K	0.17	0.04	26	0.04	0.18	55	0.07	0.04	21
J–K	0.64	0.04	26	0.33	0.18	56	0.24	0.09	24
K–L	0.19	0.07	26	0.26	0.09	55	0.08	0.16	16
L–M	0.03	0.15	24	0.32	0.18	51	0.13	0.16	8

Table 2. (Contd.)

RX Cas				V 360 Lac		
JD 2400000+	46362	1787	58	51157	187	20
J	6.48	0.20	56	5.59	0.06	20
H–K	0.24	0.08	48	0.10	0.02	20
J–K	0.84	0.05	55	0.27	0.04	20
K–L	0.25	0.05	25	0.08	0.02	18
L–M	−0.04	0.16	21	−0.04	0.14	17

(c) Miras

V CrB				R LMi			U Ori		
Parameter	Mean	SD	*N*	Mean	SD	*N*	Mean	SD	*N*
JD 2400000+	47870	9493	23	48197	860	16	48738	1409	14
J	3.56	0.48	23	1.84	0.21	16	0.87	0.32	14
H–K	0.87	0.11	23	0.79	0.08	15	0.63	0.08	14
J–K	2.06	0.17	23	1.75	0.08	16	1.39	0.12	14
K–L	1.15	0.06	23	0.84	0.28	15	0.66	0.14	14
L–M	0.12	0.08	23	−0.01	0.06	14	−0.01	0.06	14
RU Her				S Per			R UMa		
JD 2400000+	49457	1710	21	47704	273	11	48016	687	12
J	1.73	0.41	21	3.37	0.72	11	2.71	0.19	12
H–K	0.74	0.09	21	0.76	0.19	11	0.58	0.08	11
J–K	1.50	0.12	21	1.72	0.18	11	1.26	0.07	12
K–L	0.76	0.09	21	1.16	0.26	11	0.78	0.06	12
L–M	0.18	0.07	21	0.49	0.19	11	0.02	0.06	12

(d) “Unique” objects

V 407 Cyg				FG Sge (before IR outburst)			627 Cas		
Parameter	Mean	SD	*N*	Mean	SD	*N*	Mean	SD	*N*
JD 2400000+	49446	1994	43	47087	512	16	48636	1345	24
J	5.07	0.53	41	7.10	0.13	16	5.85	0.27	22
H–K	0.75	0.12	41	0.12	0.05	16	1.06	0.08	22
J–K	1.96	0.17	41	0.53	0.07	16	2.42	0.10	22
K–L	0.92	0.18	41	0.26	0.08	13	1.48	0.41	23
L–M	0.22	0.13	32	0.15	0.25	6	0.47	0.13	16

RW LMi				FG Sge (after outburst)		
JD 2400000+	49259	1806	47	50400	584	71
J	6.28	0.63	46	8.55	1.09	61
H–K	2.25	0.13	47	1.42	0.45	53
J–K	4.50	0.14	46	2.67	0.86	58
K–L	2.93	0.16	47	2.03	0.60	61
L–M	0.98	0.17	47	0.66	0.76	42

(e) “Others”

ζ Aur				P Cyg			VV Cep		
Parameter	Mean	SD	*N*	Mean	SD	*N*	Mean	SD	*N*
JD 2400000+	51014	228	23	50940	317	8	51075	260	17
J	1.12	0.04	23	3.80	0.05	8	1.07	0.04	17
H–K	0.20	0.05	23	0.25	0.03	8	0.29	0.04	17
J–K	0.99	0.05	23	0.51	0.05	8	1.17	0.04	17
K–L	0.18	0.04	23	0.44	0.05	8	0.29	0.03	17
L–M	−0.29	0.03	23	0.16	0.05	8	−0.48	0.07	17

ε Aur (eclipse, 1982–1984)				ε Aur (maximum)		
JD 2400000+	45429	55	4	51027	223	22
J	2.60	0.03	4	1.82	0.03	22
H–K	0.14	0.04	4	0.12	0.05	22
J–K	0.37	0.05	4	0.39	0.03	22
K–L				0.23	0.03	22
L–M				0.02	0.03	22

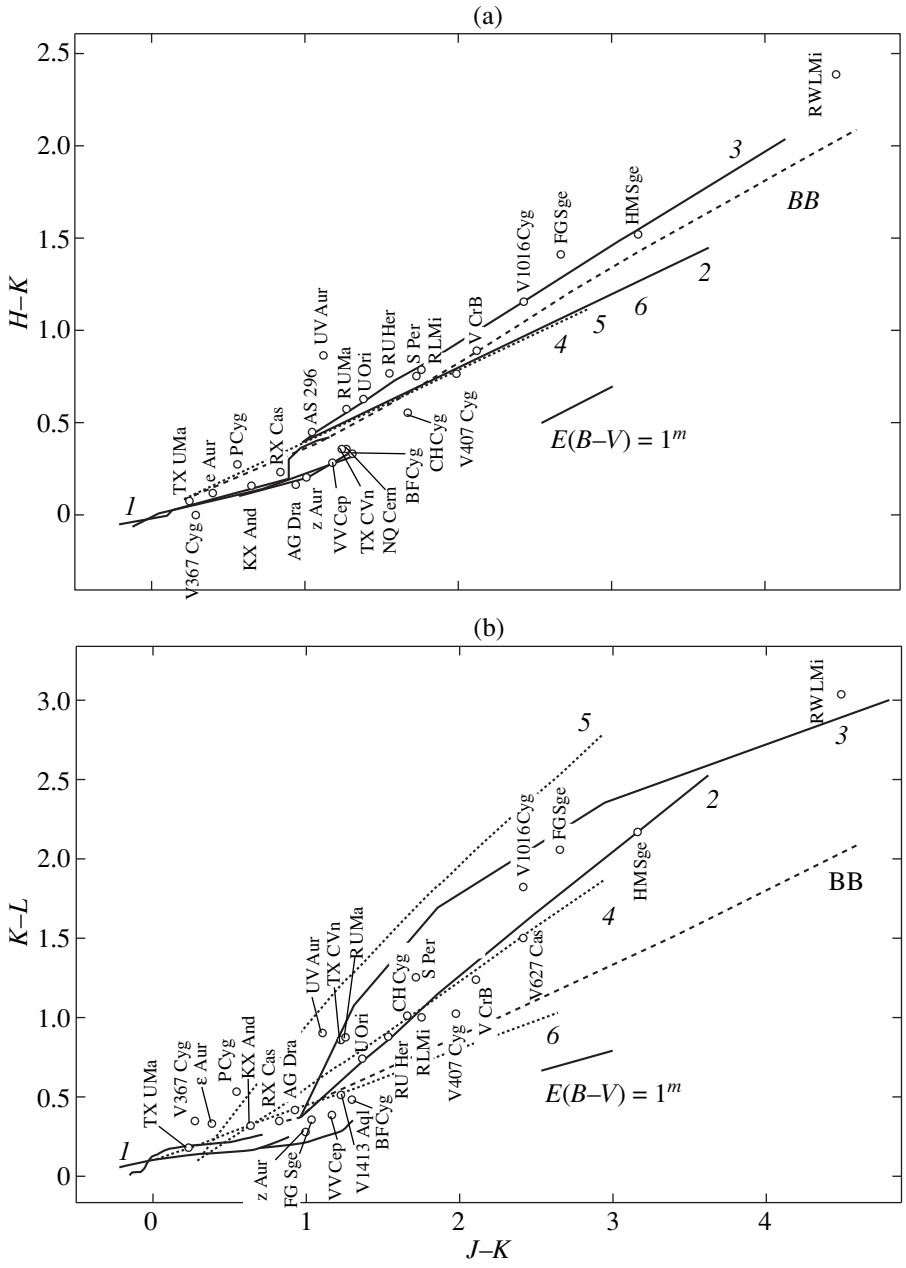

Fig. 1. Two-color [(*J*–*K*), (*H*–*K*)] (a) and [(*J*–*K*), (*K*–*L*)] (b) diagrams. The open circles represent mean color indices for the program stars. Lines *1* refer to normal stars [4]. Dashed lines *BB* indicate variations in the corresponding color indices of a blackbody with its temperature. The solid and dotted lines (*2*–*6*) represent our model calculations, and the color variations along these curves reflect variations in the optical depths of the corresponding dust shells. The short solid lines indicate color variations with interstellar extinction with $E(B–V) = 1^m$.

Then,

$$F_{\rm obs}(\lambda) \approx \Theta^2_{\rm star} B(\lambda, T_{\rm star}) e^{-\tau(\lambda)} \times [1 + 0.25(T_{\rm star}/T_{\rm dust})^{4+\beta} (B(\lambda, T_{\rm dust})/B(\lambda, T_{\rm star}) \times (e^{\tau(\lambda)} - 1)] \equiv \Theta^2_{\rm star} B(\lambda, T_{\rm star}) e^{-\tau(\lambda)} \times D(\lambda, \tau(\lambda), T_{\rm star}, T_{\rm dust}, \beta). \quad (5)$$

Changing to magnitudes, we have

$$m_{\rm obs}(\lambda) \approx [m_{\rm star}(\lambda) + 1.08\tau(\lambda)] + [-2.5\log D(\lambda, \tau(\lambda), T_{\rm star}, T_{\rm dust}, \beta)], \quad (6)$$

where $m_{\rm star}(\lambda)$ is the central star's magnitude outside the shell. The first term (in square brackets) describes attenuation of the observed star's brightness by the dust shell, and the second term describes its increase due to

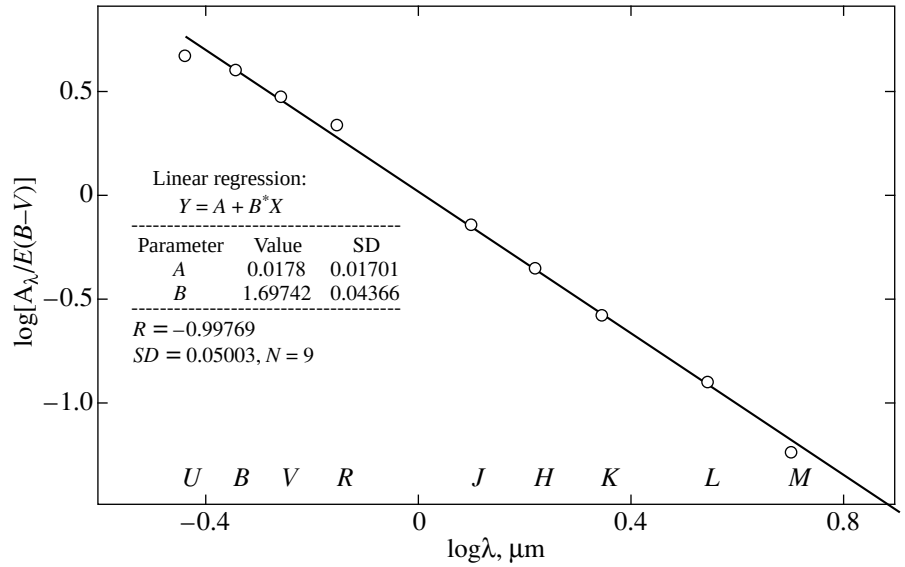

Fig. 2. $\log[A_\lambda/E(B–V)]$ versus $\log\lambda$. The straight line is a linear fit.

intrinsic radiation from the shell itself. If the parameters (radius and temperature) of the central source are assumed to be constant, then the observed magnitude variations depend only on the dust-grain temperature and on the optical depth of the dust shell.

The parameter β depends on the kind of dust grains. For interstellar dust grains, it is close to 1.7 in the spectral range 0.36–5 μm. This value is obtained for a linear fit to the wavelength dependence of interstellar extinction, as shown in Fig. 2, where $\log\lambda$ and $\log[A_\lambda/E(B–V)]$ are plotted along the *x* and *y* axes, respectively. Note that $A_\lambda \approx 0.92\tau(\lambda)$. For interstellar grains, we took the following ratios:

$$A_U/A_B/A_V/A_R/A_J/A_H/A_K/A_L/A_M = 4.78/4.05/3.05/2.23/0.75/0.46/0.27/0.13/0.08. \quad (7)$$

The straight line in Fig. 2 is a linear fit for (7).

Based on the assumptions and relations described above, we computed several model spectral energy distributions for a source surrounded by a dust shell with a variable optical depth for several sets of parameters (T_{star} and T_{dust}) at $\beta \sim 1.7$. These model calculations are represented by curves *2–6* in the two-color diagrams of Figs. 1a and 1b; their parameters are listed in Table 3, where $\tau_b(J)$ and $\tau_e(J)$ give the range of optical depths at $\lambda = 1.25$ μm (*J* band). The color variations along curves *2–6* in Figs. 1a and 1b reflect variations in the optical depths of the corresponding dust shells.

Table 3. Model parameters for a "star + dust shell" system

Model number	$\tau_b(J)$	$\tau_e(J)$	T_{star}, K	T_{dust}, K	R_{dust}/R_{star}
2	0	5	3500	350	354
3	0	4	3500	600	76
4	0	5	8000	220	13153
5	0	5	8000	250	9742
6	0	5	10000	150	78905

Figure 1b shows that the thickest dust shell is observed around the "unique" carbon star RW LMi. The mean temperature of its dust shell in our model is close to 600 K; its mean optical depth at a wavelength of 1.25 μm is $\langle\tau(J)\rangle \sim 4(\langle A_V\rangle \sim 18)$. For the group of stars consisting of the symbiotic stars (HM Sge, CH Cyg, AS 338), Miras (V CrB, R LMi, RU Her, U Ori), and the "unique" object V627 Cas, the dust-shell temperatures are $T_{dust} \sim 350$ K. Among these stars, the symbiotic star HM Sge has the densest shell [$\langle\tau(J)\rangle \sim 4$], and the Mira U Ori has the least dense shell [$\langle\tau(J)\rangle < 1$]. $\langle\tau(J)\rangle \sim 2$ for the Mira V CrB and $\langle\tau(J)\rangle \sim 2.5$ for the "unique" object V627 Cas. The mean temperature of the dust shell around the "unique" object V407 Cyg is below 350 K and $\langle\tau(J)\rangle \sim 2$. The systems FG Sge, V1016 Cyg, and TX CVn, and the Miras S Per and R UMa have dust shells with mean temperatures of ~500 K. Among these stars, the shell around FG Sge is densest ($\langle\tau(J)\rangle \sim 3$), and the shells around TX CVn and R UMa are least dense ($\langle\tau(J)\rangle < 0.3$).

The remaining stars have small brightness and color excesses, and if we attribute these excesses to dust shells, then their $\langle\tau(J)\rangle$ cannot exceed 0.1.

Parameters of the dust shells around the program stars, together with estimated parameters of the stars themselves, either have been considered in more detail in our cited papers or will be analyzed in the future.

CONCLUSION

Our analysis of the mean color characteristics for 35 stars of different variability types obtained from twenty-year-long *JHKLM* photometry at the Crimean Station of the SAI enables us to subdivide them into several groups:

(1) Stars with no evidence of radiation from dust shells with temperatures above 250 K. These include, in particular, all the classical symbiotic stars under study, W Ser stars and the Algol, and the stars ε and ζ Aur.

(2) Stars surrounded by dust shells with temperatures of 300 K or higher, but their optical depths at $\lambda = 1.25$ μm do not exceed 0.5. This group contains such dissimilar (in the nature of variability) objects as the symbiotic stars TX CVn, CH Cyg, and UV Aur, the "unique" object V407 Cyg, and six Miras.

(3) Stars surrounded by optically thick dust shells with temperatures of 350 K or higher. The densest dust shell is observed around the carbon star RW LMi. This group contains the symbiotic novae HM Sge and V1016 Cyg and the "unique" stars V627 Cas and FG Sge.

It should be noted that all our estimates of the mean dust-shell parameters were made for a simple model of a star surrounded by a spherically symmetric, physically thin dust shell, whose grains are similar to interstellar ones. Actually, the condition of spherical symmetry is often not satisfied. For instance, a break in the dust shell whose size is comparable to the diameter of the central star is enough for us to see the stellar radiation which is not attenuated by the dust shell, while the radiation from the shell itself will change only slightly. Conversely, a compact dust cloud can significantly attenuate the starlight, while its own radiation will be unnoticeable.

ACKNOWLEDGMENTS

I am grateful to V.I. Shenavrin, B.F. Yudin, and other researchers of the IR astronomy group at the SAI for simultaneous observations. This study was supported in part by the Russian Foundation for Basic Research (project no. 96-02-16353).

REFERENCES

1. A. E. Nadzhip, V. I. Shenavrin, V. G. Tikhonov, Trudy Gos. Astron. Inst. Shternberg **58**, 119 (1986).
2. P. N. Kholopov, N. N. Samus', V. P. Goranskiĭ *et al.*, *General Catalogue of Variable Stars* (Nauka, Moscow, 1985–1990).
3. H. L. Johnson, R. I. Mitchell, B. Iriarte, and W. Z. Wisniewski, Comm. Lunar Planet. Lab. **4**, 99 (1966).
4. J. Koornneef, Astron. Astrophys. **128**, 84 (1983).
5. A. M. Tatarnikov and B. F. Yudin, Pis'ma Astron. Zh. **24**, 359 (1998) [Astron. Lett. **24**, 303 (1998)].
6. O. G. Taranova, Astrofizika **25**, 453 (1986).
7. O. G. Taranova, Pis'ma Astron. Zh. **13**, 423 (1987).
8. V. P. Arkhipova and O. G. Taranova, Pis'ma Astron. Zh. **16**, 808 (1990) [Sov. Astron. Lett. **16**, 347 (1990)].
9. E. M. McCabe, Mon. Not. R. Astron. Soc. **200**, 71 (1982).
10. O. G. Taranova and V. I. Shenavrin, Pis'ma Astron. Zh. **9**, 5 (1982).
11. O. G. Taranova, V. I. Shenavrin, and A. E. Nadzhip, Astron. Tsirk., No. 1370 (1985).
12. O. G. Taranova, Pis'ma Astron. Zh. **13**, 502 (1987) [Sov. Astron. Lett. **13**, 374 (1987)].
13. O. G. Taranova and V. I. Shenavrin, Pis'ma Astron. Zh. **23**, 810 (1997) [Astron. Lett. **23**, 698 (1997)].
14. U. Munari, B. F. Yudin, O. G. Taranova, *et al.*, Astron. Astrophys., Suppl. Ser. **93**, 383 (1992).
15. O. G. Taranova, Astrofizika **27**, 29 (1987).
16. O. G. Taranova and V. I. Shenavrin, Pis'ma Astron. Zh. **25**, 860 (1999) [Astron. Lett. **25**, 750 (1999)].
17. O. G. Taranova, Astron. Tsirk., No. 1467, 7 (1986).
18. O. G. Taranova, Astron. Tsirk., No. 1462, 4 (1986).
19. O. G. Taranova and B. F. Yudin, Pis'ma Astron. Zh. **9**, 36 (1983) [Sov. Astron. Lett. **9**, 19 (1983)].
20. O. G. Taranova and B. F. Yudin, Astron. Zh. **61**, 510 (1984).
21. O. G. Taranova and B. F. Yudin, Astron. Zh. **59**, 101 (1982).
22. O. G. Taranova and B. F. Yudin, Pis'ma Astron. Zh. **11**, 55 (1985) [Sov. Astron. Lett. **11**, 23 (1985)].
23. E. A. Kolotilov and B. F. Yudin, Pis'ma Astron. Zh. **20**, 411 (1994) [Astron. Lett. **20**, 347 (1994)].
24. V. F. Esipov, O. G. Taranova, and B. F. Yudin, Astrofizika **29**, 286 (1988).
25. O. G. Taranova and B. F. Yudin, Pis'ma Astron. Zh. **8**, 722 (1982) [Sov. Astron. Lett. **8**, 389 (1982)].
26. A. P. Ipatov and O. G. Taranova, Astron. Astrophys. **135**, 325 (1984).
27. O. G. Taranova and B. F. Yudin, Astrophys. Space Sci. **146**, 33 (1988).
28. O. G. Taranova and B. F. Yudin, Astron. Zh. **69**, 262 (1992).
29. O. G. Taranova, B. F. Yudin, and E. A. Kolotilov, Pis'ma Astron. Zh. **21**, 529 (1995) [Astron. Lett. **21**, 470 (1995)].
30. U. Munari, B. F. Yudin, E. A. Kolotilov, and T. V. Tomov, Astron. Astrophys. **311**, 484 (1996).
31. O. G. Taranova and B. F. Yudin, Astron. Astrophys. **257**, 615 (1992).
32. O. G. Taranova and B. F. Yudin, Pis'ma Astron. Zh. **6**, 495 (1980) [Sov. Astron. Lett. **6**, 273 (1980)].
33. O. G. Taranova and B. F. Yudin, Astron. Astrophys. **117**, 209 (1983).
34. A. P. Ipatov, O. G. Taranova, and B. F. Yudin, Astron. Astrophys. **142**, 85 (1985).
35. O. G. Taranova and B. F. Yudin, Pis'ma Astron. Zh. **8**, 90 (1982) [Sov. Astron. Lett. **8**, 46 (1982)].
36. O. G. Taranova and B. F. Yudin, in *Physics of Classical Novae*, Proc. IAU Coll. No. 122, Ed. by A. Cassatella and R. Vioti (Springer, Berlin, 1990), p. 435.

37. B. F. Yudin, U. Munari, O. G. Taranova, and I. Dalmeri, Astron. Astrophys., Suppl. Ser. **105**, 169 (1994).
38. B. F. Yudin, Astron. Zh. **71**, 900 (1994).
39. O. G. Taranova and B. F. Yudin, Astron. Zh. **58**, 1051 (1981).
40. B. F. Yudin, Astron. Zh. **59**, 307 (1982).
41. O. G. Taranova and B. F. Yudin, Astron. Zh. **63**, 17 (1986).
42. O. G. Taranova, Pis'ma Astron. Zh. **13**, 891 (1987).
43. O. G. Taranova and B. F. Yudin, Astron. Tsirk., No. 1501, 7 (1987).
44. E. A. Kolotilov, U. Munari, B. F. Yudin, and A. M. Tatarnikov, Astron. Zh. **73**, 894 (1996).
45. O. G. Taranova, Pis'ma Astron. Zh. **23**, 803 (1997).
46. O. G. Taranova and B. F. Yudin, Astron. Zh. **63**, 151 (1986).
47. O. G. Taranova and B. F. Yudin, Astron. Zh. **58**, 1249 (1981).

Translated by N. Samus'